

© Copyright 2007

Jason Brown Benedict



Dyeing Crystals:  
19<sup>th</sup> Century Phenomenology to 21<sup>st</sup> Century Technology

Jason Brown Benedict

A dissertation submitted in partial fulfillment of the  
requirements for the degree of:

Doctor of Philosophy

University of Washington

2007

Program Authorized to Offer Degree:  
Department of Chemistry

UMI Number: 3293455

Copyright 2007 by  
Benedict, Jason Brown

All rights reserved.

#### INFORMATION TO USERS

The quality of this reproduction is dependent upon the quality of the copy submitted. Broken or indistinct print, colored or poor quality illustrations and photographs, print bleed-through, substandard margins, and improper alignment can adversely affect reproduction.

In the unlikely event that the author did not send a complete manuscript and there are missing pages, these will be noted. Also, if unauthorized copyright material had to be removed, a note will indicate the deletion.

**UMI<sup>®</sup>**

---

UMI Microform 3293455

Copyright 2008 by ProQuest Information and Learning Company.

All rights reserved. This microform edition is protected against  
unauthorized copying under Title 17, United States Code.

ProQuest Information and Learning Company  
300 North Zeeb Road  
P.O. Box 1346  
Ann Arbor, MI 48106-1346



University of Washington  
Graduate School

This is to certify that I have examined this copy of a doctoral dissertation  
by

Jason Brown Benedict

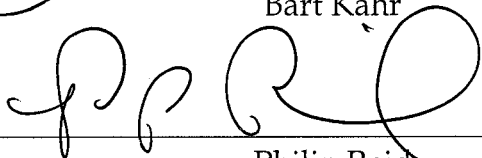
and have found that it is complete and satisfactory in all respects,  
and that any and all revisions required by the final  
examining committee have been made.

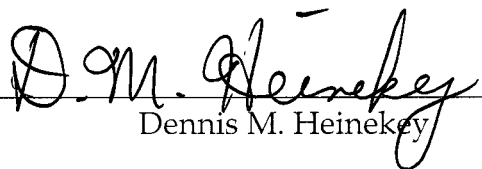
Chair of the Supervisory Committee:

  
Bart Kahr

Reading Committee:

  
Bart Kahr

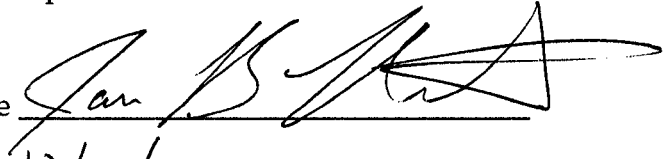
  
Philip Reid

  
Dennis M. Heinekey

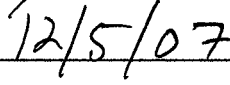
Date: 12/5/07

In presenting this dissertation in partial fulfillment of the requirements for the doctoral degree at the University of Washington, I agree that the Library shall make its copies freely available for inspection. I further agree that extensive copying of the dissertation is allowable only for scholarly purposes, consistent with "fair use" as prescribed in the U.S. Copyright Law. Requests for copying or reproduction of this dissertation may be referred to ProQuest Information and Learning, 300 North Zeeb Road, Ann Arbor, MI 48106-1346, 1-800-521-0600, to whom the author has granted "the right to reproduce and sell (a) copies of the manuscript in microform and/or (b) printed copies of the manuscript made from microform."

Signature

A handwritten signature in black ink, appearing to read "Jan B. Smith", written over a horizontal line.

Date

A handwritten date "12/5/07" in black ink, written over a horizontal line.

University of Washington

**Abstract**

Dyeing Crystals:  
19<sup>th</sup> Century Phenomenology to 21<sup>st</sup> Century Technology

Jason Brown Benedict

Chair of the Supervisory Committee:  
Professor Bart Kahr  
Department of Chemistry

The linear dichroism of organic light-absorbing molecules (dyes) contained within varied solid matrices are analyzed. Hosts of increasing disorder from single crystals, to organized polycrystalline formations, to polymers are examined. Organic chromophores contained within single crystal hosts serve as optical reporters of the local chemical environment within the crystal and on the growing crystal surfaces. The selectivity for various crystallographic facets combined with knowledge of the structure of the surfaces allows inferences to be drawn regarding the non-covalent interactions that govern crystal growth from solution. Peculiar concepts from the descriptive crystallographic literature of the 19<sup>th</sup> century are framed in contemporary terms. Attempts to utilize non-centrosymmetric dyed crystals as gain media for up-conversion lasing are described. Acentric media are likewise considered for electrooptic modulation of light. In principle, the growth front of radial non-centrosymmetric polycrystals, known as spherulites, would orient dyes dissolved in the melt in a polar manner. The linear optical properties of dyed spherulites are described.

While the strong linear dichroism of the spherulite was indicative of dye alignment, the absence of an enhanced second harmonic generation signal reveal that the dye domains remain effectively centrosymmetric. These materials are nevertheless instructive in illustrating the principles of the orientational dependence of linear dichroism, a subject of long standing confusion. Strong electric fields applied to thin polymer films containing a large proportion of organic chromophores continues to be a popular approach to generating polar ensembles of molecules. Measurements of the linear optical properties of poled polymer films were modeled to assess the magnitude of chromophore alignment and degradation during poling.

## TABLE OF CONTENTS

	Page
List of Figures .....	iv
List of Tables .....	viii
Preface.....	ix
Chapter 1 - Linear Dichroism .....	1
1.1 Background .....	1
1.2 Linearly Polarized Light .....	8
1.3 Absorption of Light .....	11
1.4 Linear Dichroism in Birefringent Media .....	14
1.4.1 Correction for Solvent Effects .....	18
1.4.2 Fresnel Reflection Corrections .....	20
Chapter 2 - Linear Dichroism of Single Crystals .....	23
2.1 History .....	23
2.2 Dyeing Potassium Acid Phthalate .....	25
2.2.1 Potassium Acid Phthalate .....	25
2.2.2 Diamino Acridine in Potassium Acid Phthalate .....	28
2.2.3 Rhodamine 110 in Potassium Acid Phthalate .....	59
2.3 Methyl Red in Phthalic Acid .....	75
2.3.1 Syncrystallization .....	78
2.3.2 Phthalic Acid .....	80

2.3.3 Methyl Red.....	85
2.3.4 Co-Crystals of Methyl Red and Phthalic Acid.....	89
2.3.5 Mixed Crystals of Methyl Red and Phthalic Acid.....	94
2.3.6 Discussion .....	113
2.3.7 Conclusions: What is Syncrystallization?.....	121
2.3.8 Experimental.....	124
Chapter 3 - Linear Dichroism of Poled Polymers.....	129
3.1 Background - Theory .....	133
3.1.1 Angular Dependence of Linear Dichroism .....	136
3.1.2 Corrections .....	143
3.1.3 The Equivalence Point.....	149
3.1.4 Chromophore Transformation.....	153
3.2 Polymer Film Preparation .....	159
3.3 NLO Film Optical Characterization.....	161
3.3.1 Qualitative Observations .....	161
3.3.2 Quantitative Analysis.....	164
Chapter 4 - Sorbitol Spherulites .....	178
4.1 Sorbitol .....	180
4.2 Sorbitol Spherulites - Undyed .....	181
4.2.1 Linear Optical Properties .....	182
4.2.2 Non-linear Optical Properties .....	186

4.3 Dyed Sorbitol Spherulites.....	188
4.3.1 Angular Dependence of Linear Dichroism .....	188
4.3.2 Electro-optic Sorbitol Spherulites .....	207
4.4 Experimental .....	219
References.....	227

## LIST OF FIGURES

Figure Number	Page
I. Luminescence of a KAP/DMASI single crystal .....	x
1.1. Commercially available calcite dichroscope .....	3
1.2. Internal assembly of a calcite rhomb dichroscope .....	4
1.3. Buckley's absorption spectra of chromotrope 2B .....	7
1.4. Schematic illustration of EDTM vector projections.....	15
2.1. Structure and habit of KAP viewed down [100].....	26
2.2. Images of black light (366 nm) irradiated KAP crystals.....	28
2.3. Fluorescence image of a KAP/DAA crystal.....	29
2.4. Contrast enhanced image of a KAP/DAA crystal .....	31
2.5. Idealized KAP habit with fast slope recognition.....	32
2.6. Absorption and luminescence spectra of KAP/DAA .....	35
2.7. Linear dichroism spectra of KAP/DAA .....	36
2.8. Protonation scheme for DAA .....	38
2.9. TR-EPR spectra of KAP/DAA .....	43



2.10.	TR-EPR spectra of the triplet states of DAA in KAP .....	45
2.11.	Angular dependencies of DAA triplets in KAP .....	46
2.12.	Surface representations of the DAA ZFS tensor in KAP. ....	48
2.13.	EPS for the stable terminations of KAP .....	51
2.14.	Energy-level diagram for DAA.....	55
2.15.	Single crystal potassium sulfate dye laser .....	61
2.16.	Photoluminescence of laser dyes doped in KAP .....	63
2.17.	Normalized one photon luminescence spectra of Rh110 .....	65
2.18.	Normalized up-conversion luminescence of Rh110 .....	68
2.19.	Schematic representations of laser cavities .....	70
2.20.	Laser damaged crystals .....	72
2.21.	Methyl red structures identified in solution equilibria .....	77
2.22.	Idealized habit of PA .....	81
2.23.	Computed energies MR molecule based on N - H distance .....	88
2.24.	MR skeleton with various co-crystal bond lengths .....	90
2.25.	Hydrogen bonds of methyl red in co-crystals.....	92
2.26.	Powder absorption spectra of crystals containing MR.....	94
2.27.	Phthalic acid crystals grown in the presence of MR .....	96
2.28.	Contrast enhanced (101) slices of a MR dyed PA crystal .....	98
2.29.	Polarized absorbance spectra of PA/MR growth sectors .....	100
2.30.	EDTMs of the strongest transitions overlaid on MR.....	102

2.31.	Spectral deconvolution for LD measurements .....	104
2.32.	Simulations of MR docking to PA surfaces .....	107
2.33.	Models of MRin (red) and MRex (yellow) within PA .....	109
2.34.	Linear dichroism images of a PA/MR crystal .....	111
2.35.	PA/MR mixed crystal showing dark bâtonnets.....	112
2.36.	MR orientations superimposed upon the PA lattice.....	115
2.37.	Normalized absorption spectra before and after heating .....	120
3.1.	Photograph of Jen 3-3; a poled polycarbonate film.....	131
3.2.	Schematic representation of the E relative to the sample.....	140
3.3.	Plot of the calculated equivalence point .....	153
3.4.	Calculated absorptances as a function of internal angle .....	158
3.5.	Structures of YLII, AJL-7, and AJL-8 .....	162
3.6.	Optical micrographs of various poled polymer samples .....	163
3.7.	Photograph of polymer sample on spindle stage.....	164
3.8.	Absorption spectra of the poled and un-poled domains .....	168
3.9.	Traces of the experimentally determined absorptance.....	169
3.10.	Traces of the experimentally determined absorbance .....	170
3.11.	Traces of the absorptance of the photodamaged sample .....	172
4.1.	Chemical structure of D-sorbitol on an optical micrograph.....	181
4.2.	Metripol images of sorbitol spherulites. ....	182
4.3.	AFM images of a sorbitol spherulite .....	184

4.4.	Additional AFM images of a sorbitol spherulite .....	185
4.5.	X-ray diffraction powder pattern of sorbitol.....	186
4.6.	SHG image of a pure sorbitol spherulite .....	187
4.7.	Absorption spectra of sorbitol containing amaranth .....	192
4.8.	Metripol images of spherulites containing amaranth.....	193
4.9.	Idealized index/absorption ellipsoids .....	194
4.10.	Polarized transmittance image of a spherulite .....	196
4.11.	Transmittance and absorbance plots, $\theta$ rotations .....	197
4.12.	Transmittance for $\varphi_{\perp}$ and $\varphi_{\parallel}$ rotations .....	199
4.13.	Schematic representation of a view parallel to a $\varphi$ rotation.....	204
4.14.	Structure of DAST superimposed upon a micrograph.....	208
4.15.	SHG image of a sorbitol spherulite containing DAST .....	210
4.16.	Additional SHG image of a spherulite containing DAST .....	211
4.17.	Additional SHG image of a spherulite containing DAST .....	212
4.18.	Metripol images of a damaged DAST spherulite .....	214
4.19.	Optical micrograph of a collimated sorbitol spherulite .....	216
4.20.	DAST skeleton with bond lengths.....	217

## LIST OF TABLES

Table Number	Page
2.1. Eigenvalues of ZFS tensors of DAA in matrices.....	44
2.2. Crystallographic data .....	83
2.3. Computed PA surface and attachment energies .....	84
2.4. Calculated replacement energies for mixed crystal models .....	110
2.5. Similarities between co-crystals and pure crystal structures .....	118
3.1. Summary of poled polymer films details .....	160

## PREFACE

One of the first experiments I carried out at the University of Washington was the crystallization of potassium acid phthalate (KAP) in the presence of dimethylaminostilbazolium iodide (DMAI), a dye with numerous photonic applications. Because KAP has perfect cleavage, the crystal could be sliced revealing an extraordinary texture in the luminescence associated with dye incorporation into specific growth sectors, polyhedral sub-volumes of the crystal that has grown through individual (*hkl*) facets. These images clearly illustrate the multitude of photophysical consequences that can arise from the interactions of a single chromophore with a growing single crystal.

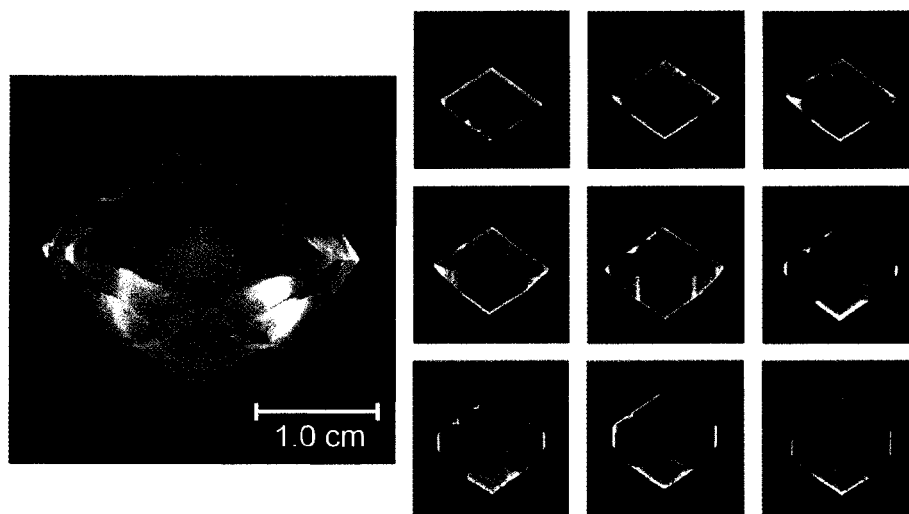


**Figure I.** Luminescence of a KAP single crystal (left) grown in the presence of DMASI and cleaved into nine successive 250  $\mu\text{m}$  slices from top (upper left) to bottom (lower right).

Shortly thereafter, the number of scientists interested in the photophysics of dyes with large hyperpolarizabilities increased by many dozen at the University of Washington when the Department of Chemistry became host to the National Science Foundation's Materials and Devices for Information Technologies Research Science and Technology Center. Consequently I interrupted for a period of time my study of complex photophysical consequences of dyed crystals to investigate by like methods – linear dichroism spectroscopy and polarimetry- comparable chromophores in the vastly more complex electric field poled polymers.

This work established the conviction that structural chemical inferences would only be forthcoming by returning to a well-ordered host. As illustrated in Figure I, the anticipated complexities are sufficient to fill this thesis. Nevertheless, the final chapter describes attempts to marry the virtues of dyed crystals and polymers in dyed polycrystalline media.

## **Acknowledgements**

Thank you to my committee: Dr. Daniel Gamelin, Dr. Phil Reid, Dr. Mike Heinekey and Dr. Alex Jen.

Thank you to my fellow graduate students: Dr. Andri Arnaldsson, Dr. Steven Bowles, Dr. Colleen Craig, Dr. Joesph Dragavon, Brad Habenicht, Dr. Scott Hammond, Dr. Eric Heatwole, Dr. Paul Miller, Dan 'The Man' Patel, Dr. Stephen Reichow, Dr. Harrison Rommel.

Thank you to my lab members: Dr. Yonghong Bing, Eric Bott, Charles Branham, Theresa Bullard, Dr. Kacey Claborn, Dawn Cohen, John Freudenthal, Erica Gunn, Eva Hollis, Christine Isborne, Dr. Sei-Hum Jang, Matt Nichols, Stephen Powell, Sarah Price, Scott Randall, Laura Snyder, Dr. Ryan 'McTowelieeee' Sours, Jillian Thayer and last but certainly not least, Kristin Wustholz.

Thank you Walter and Julia Duncan. We have shared many great experiences and will undoubtedly share many more.

Thank you Dr. Werner Kaminsky for all of your scholarly advice. I will never tire of your verbose anecdotes, topical or not.

Thank you Jarrod and Lance. Distance has not, nor will it ever, weaken our friendship.

Thank you to my family: Benjamin, June and Courtney Benedict. Your generous support of my undergraduate education made all this possible. Grammy Benedict for always checking up on me and making sure I always studied hard; Roger and Margaret for many, many conversations about many, many futures. Mr. Herbie Snuggles McButtersworth III and Stain for always agreeing with me and taking my side. Always.

To my siblings, Melinda, Cherie, John and little Hannah: I am honored when I see myself in you, and fulfilled when I see you in me.

To my parents: Pops taught me frugality and reason. Da Mama taught me to embrace and appreciate the waxing and waning of my emotional self.

Thank you Bart. You are my advisor, my mentor, my friend. You will never be rid of me. Thank you.

And finally to my wife, my queen, Tasha, who would love me just as much if this were a book on pastries. Thank you.



## Dedication

For my grandmother, Catharine Cooke Brown:

I hope this wins a fur-lined bathtub.

## CHAPTER 1 - LINEAR DICHROISM

### 1.1 Background

Michl and Thulstrup<sup>1</sup>, in their treatise on polarized light spectroscopy, indicate that the investigation of aligned solutes with linearly polarized light extends to at least 1888 when Ambronn<sup>2</sup> described the absorption anisotropy of dye-stained cell membranes. The scientific study of oriented solutes actually began at least 30 years earlier in 1854<sup>3</sup> when Henri de Sénarmont produced crystals of strontium nitrate tetrahydrate grown in the presence of logwood extract, *Sénarmont's Salt*.

Sénarmont, motivated to understand pleochroism of minerals, wondered if the anisotropic absorption of light could be induced in other optically transparent crystals grown in the presence of coloring agents. In “The Production of Artificial Pleochroism in Crystals” he describes crystals that when viewed with linearly polarized light, appeared either red or violet

depending on the crystal orientation. Numerous attempts have been made to reproduce these pleochroic crystals since the work was originally published<sup>4</sup>, most ending in failure. The study of dyed crystals proceeded in fits and starts for nearly a century, undoubtedly inhibited by the difficulty in reproducing these early experiments.

Crystalline minerals and gems were undoubtedly the source of the earliest observations of linear dichroism. The first substantial characterization of linear dichroism in crystals was reported by a pioneer in crystal optics, Sir David Brewster.<sup>5</sup> This work was a continuation of his paper published a year earlier in which he characterized the refractive properties of 165 minerals.<sup>6</sup> By viewing minerals with polarized light through an aperture attached to a rhomb of the mineral to be examined, he recorded the observed colors based on the input polarization for over 30 minerals. Previously, dichroism had only been observed in iolite and erroneously believing this property to be unique to this mineral, Abbé Haüy renamed it *dichroite*. Brewster's extensive survey, however, unambiguously established dichroism as "a very common property of crystallized bodies."<sup>5</sup>

Today we take for granted the incredible convenience and utility of commercial spectrophotometers for the analysis of light absorbing media. In the 19<sup>th</sup> century, however, optical photometry was a practiced art. One of the first tools available to researchers studying dichroic materials was the aptly named dichroscope which enabled a user to view the two polarized rays emitted from a doubly refracting crystal side-by-side (Figure 1.1).



**Figure 1.1.** Commercially available calcite dichroscope (left) illustrating dichroism of tourmaline as seen through the scope (right).<sup>7</sup>

Because the two images can be viewed simultaneously and side-by-side, subtle differences in color or intensity can be detected. This instrument is still in used today primarily by gemologists to quickly characterize rough gemstones. A skilled faceter uses the device to determine the optimal viewing direction for a rough stone, cutting and polishing accordingly.

The most common dichroscope consists of a cleaved piece of optical quality calcite rhomb (Iceland spar) to which glass prisms have been attached on both ends (Figure 1.2). This assembly is encased within a tube having an aperture at one end and an eye piece on the opposite side. The complimentary angles of the glass prisms with respect to the rhomb allow light to enter and exit the optical train in a straight line.

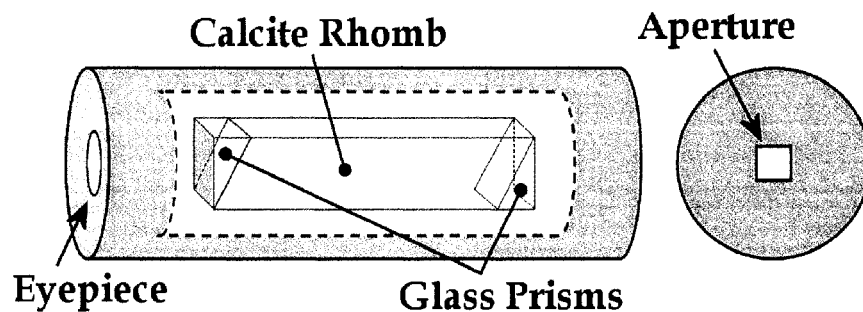


**Figure 1.2.** Diagram illustrating the internal assembly of a calcite rhomb dichroscope.

The material to be examined is placed in front of the aperture, bathed in unpolarized white light, and viewed through the eyepiece. If the material is uniaxial or biaxial and not viewed parallel to an optic axis, the strong birefringence of the calcite will split the two polarizations into two unique images. It is possible for the vibration directions of the sample to be oriented at  $45^\circ$  with respect to the calcite directions resulting in no apparent

dichroism. For that reason it is important to view the sample in varied orientations to ensure adequate characterization.

Dichroism can be observed by viewing the sample through a single polarizer and rotating either the sample or polarizer, but weak dichroism is difficult to observe. A simpler version of the dichroscope can be constructed by placing two sections of a standard sheet polarizer side-by-side in a suitable holder so that the two domains are aligned with the orthogonal vibration directions. This alternative arrangement enables the simultaneous viewing of a sample through the two domains but without the benefit of imaging the same domain.

While the dichroscope has played and continues to play an important role in the qualitative characterization of dichroism in solids, a quantitative understanding was realized with the advent of optical spectroscopy.

The science of spectroscopy began in 1817 when Joseph von Fraunhofer characterized the emission lines from flames and the sun.<sup>8</sup> In 1834, Sir David Brewster surmised that “a general principle of chemical analysis in which simple and compound bodies might be characterized by their action on definite parts of the spectrum” after observing the dark line spectrum of  $\text{NO}_2$  in his laboratory.<sup>9</sup> Robert Bunsen and Gustav Kirchhoff published

details of the first spectrometer in 1861 commencing a rapid expansion in this analytical technique.<sup>10</sup> Henry Clifton Sorby introduced microspectrophotometry – the marriage of a polarizing microscope and a spectrophotometer.<sup>11</sup> Bunsen was the first to quantitatively measure linear dichroism by publishing the first polarized absorption spectra using single crystals of didymium sulfate.<sup>12</sup> The linear dichroism of dyed crystals was first quantitatively characterized by Buckley in 1951 when he published the polarized absorption spectra of potassium sulfate dyed with chromotrope 2B (Figure 1.3).<sup>13</sup>

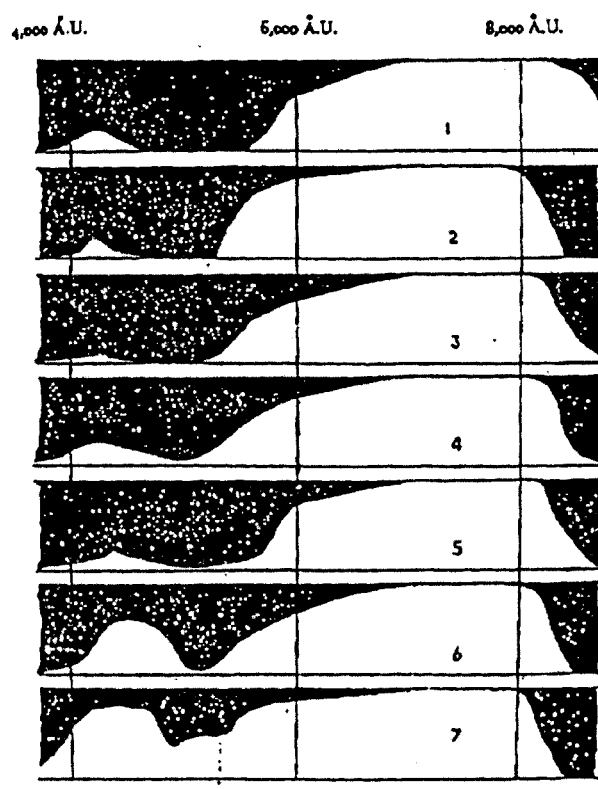


**Figure 1.3.** Buckley's absorption spectra of chromotrope 2B in an aqueous solution (1), in  $\text{NH}_4\text{ClO}_4$  (2,3,4) and in  $\text{K}_2\text{SO}_4$  (5,6,7).

Michls and Thulstrup draw a distinction between the linear dichroism of crystals and the linear dichroism of partially aligned systems such as oriented polymers, liquid crystals and lipid bilayers. These systems typically exhibit a much lower degree of organization; the light absorbing species possessing a biased, but continuous distribution of orientations. This distinction is reasonable in the case of single crystals or stoichiometric



co-crystals, the structure and composition of which can be determined by x-ray diffraction and directly compared to optical measurements. Single crystal hosts containing light absorbing impurities at concentrations less than 1% blur this distinction as we shall see illustrate in the forthcoming chapters.

## 1.2 Linearly Polarized Light

Any material that contains partially or fully aligned molecules will absorb linearly polarized light differently depending on the direction and polarization of the incident light. The molecular alignment that gives rise to absorption anisotropy or linear dichroism can occur naturally in crystals or membranes or can be induced in an optically isotropic sample by electric field poling or mechanical stretching of doped polymers

There are two unique applications for the information that can be determined from measurements of linear dichroism: structural and spectroscopic. Structural information such as the orientation of the molecular species can be determined if information about the electronic dipole transition moments (EDTM) are known. Conversely, if the

orientation of the molecular species is known, spectroscopic information about directions of the transition moments within the molecule can be determined. This thesis will be concerned primarily with the former as many of the case studies involve rod-like,  $\pi$ -conjugated chromophores (guests) aligned within optically transparent hosts. Guests of this nature provide several distinct advantages: the high aspect ratio of the shape will typically lead to stronger alignment and the  $\pi$ - $\pi^*$  electronic transition (dominant, distinct, and computationally accessible) is typically coincident with the long axis of the molecule. Even with these advantages, numerous corrections and considerations must be taken into account when analyzing and interpreting linear dichroism measurements on dyes oriented within solid matrices.

Light is considered linearly polarized when the vectors describing the electric fields of the photons oscillate in a plane. A description of linearly polarized light in a vacuum as a function of time begins with<sup>1</sup>:

$$E(t) = E_0 \sin(2\pi\nu t + \theta)$$

where  $E_0$  is a constant vector constrained to oscillate in a plane perpendicular to the direction of propagation.  $E(t)$  describes the direction or polarization of the light in this plane as a function of time. At  $t = 0$ , the

phase of the light is  $\theta$ . The phase of the light as a function of time is  $(2\pi\nu t + \theta)$  which includes  $\nu$ , the frequency of the electric field oscillations in cycles per second. This frequency is related to the angular frequency by the equation,  $\omega = 2\pi\nu$ .

Constraining the  $E(t)$  to oscillate in the YZ plane with wave propagation along the X direction, the equation becomes:

$$E(t, X, 0, 0) = E_0 \sin [2\pi(\nu t - X/\lambda) + \theta] = E_0 \sin [2\pi\nu(t - X/c) + \theta]$$

where the wavelength of light is  $\lambda = c/\nu$  and the speed of light,  $c$ , is  $3 \times 10^8$  m/s. The phase of the light is  $\theta$  when  $X = t = 0$ .

The vector describing the corresponding magnetic field of the electromagnetic wave is given by

$$H(t, X, 0, 0) = H_0 \sin [2\pi(\nu t - X/\lambda) + \theta] = H_0 \sin [2\pi\nu(t - X/c) + \theta]$$

where  $H_0$  is a constant vector perpendicular to  $E_0$  in the YZ plane.

Light can also be characterized by a wave vector  $k$  in which  $k = (2\pi/\lambda)\epsilon_x$ . In this case,  $\epsilon_x$  is a unit vector parallel to the propagation direction, X. The  $k$  vector description provides a convenient means of determining the angular momentum of the photon which is simply  $k\hbar$ , where  $\hbar = h/2\pi$  and  $h$  is Plank's constant,  $6.6256 \times 10^{-27}$  erg s. Conversion between the vector length

$|k|$ , the wavelength  $\lambda$ , the frequency  $\nu$ , the angular frequency  $\omega$ , and the wavenumber  $\tilde{\nu}$  is given by the follow equations:

$$\nu = \tilde{\nu}c = c / \lambda = c|k| / 2\pi$$

$$\omega = 2\pi c / \lambda = c|k|$$

The majority of optical measurements in this thesis will be conducted using visible light ( $400 \text{ nm} < \lambda < 700 \text{ nm}$ ), although the anisotropic absorption of microwaves is described in chapter 2.

### 1.3 Absorption of Light

When a monochromatic parallel beam of radiation with intensity,  $I_0$ , is passed through an isotropic medium containing an absorbing species, the intensity of the radiation exiting the sample,  $I$ , is reduced. The transmittance, or the fraction of incident radiation transmitted by the medium, is given by the equation:

$$T = \frac{I}{I_0}$$

The transmittance is related to the absorbance,  $A$ , by the equation:

$$A = -\log_{10} T = \log \frac{I_0}{I}$$

In accordance with Beer-Lambert law, the sample absorbance is directly proportional to the sample of thickness,  $b$  (in centimeters), and concentration,  $c$  (in moles per liter,  $M$ ), of absorbing molecules given by

$$A = \varepsilon bc$$

where  $\varepsilon$  is the molar extinction coefficient having the units  $M^{-1} \text{ cm}^{-1}$  and is valid in the absence of concentration dependent intermolecular interactions.

Absorption in a medium occurs when the electric field and/or the magnetic field of the incident radiation initiates a transition into a higher energy state. The polarization of the transition is the direction describing the net linear displacement of charge following absorption. In the case of electronic transitions within a molecule, the electric dipole transition moment (EDTM) of the  $n$ -th transition is a vector,  $M_n$ , characterized by the polarization and the intensity of this transition.

The probability,  $W_n$ , that this transition will occur depends on of the square of the projection of  $M_n$  onto the electric vector of the linearly polarized incident radiation,  $E$ :

$$W_n \propto (\mathbf{M}_n \cdot \mathbf{E})^2 = |\mathbf{M}_n|^2 \cos^2(\mathbf{M}_n, \mathbf{E})$$

The transition probability is maximum when  $(\mathbf{M}_n, \mathbf{E})$ , the angle between  $\mathbf{M}_n$  and  $\mathbf{E}$ , is zero. The probability goes to zero when  $\mathbf{M}_n$  and  $\mathbf{E}$  are perpendicular. The square of the length of the EDTM,  $|\mathbf{M}_n|$ , for the  $n$ -th transition is related to  $f_n$ , the oscillatory strength of the transition:

$$f_n = |\mathbf{M}_n|^2$$

An electronic transition within a molecule can thus be characterized by two parameters: the energy ( $\xi$ ), a scalar quantity and the EDTM vector,  $\mathbf{M}_n$ . The direction of  $\mathbf{M}_n$  and the intensity of the transition,  $f_n$  within the molecular framework determines the molecular absorption properties. Transitions in which  $\mathbf{M}_n$  goes to zero are considered forbidden and have no absorption intensity.

The majority of linear dichroism measurements in this thesis probe the alignment of rod-like conjugated organic chromophores. In these chromophores, the  $\pi \rightarrow \pi^*$  transitions are the most intense transitions in the visible spectrum and are polarized in the plane of conjugation, co-linear with the long axis of the molecule. In these cases, a molecular orientation

within the matrix can easily be established based upon the orientation of the EDTM.

#### 1.4 Linear Dichroism in Birefringent Media

Linear dichroism (LD), the differential absorption of linearly polarized light between two orthogonal polarizations, can be expressed as

$$LD = A_{\parallel} - A_{\perp}$$

In birefringent samples,  $A_{\parallel}$  and  $A_{\perp}$  are always coincident with the observed extinction directions. The absorption along these two directions is determined by the projection of the EDTM vector onto the vectors describing the electric fields of the incident linearly polarized radiation (Figure 1.4).

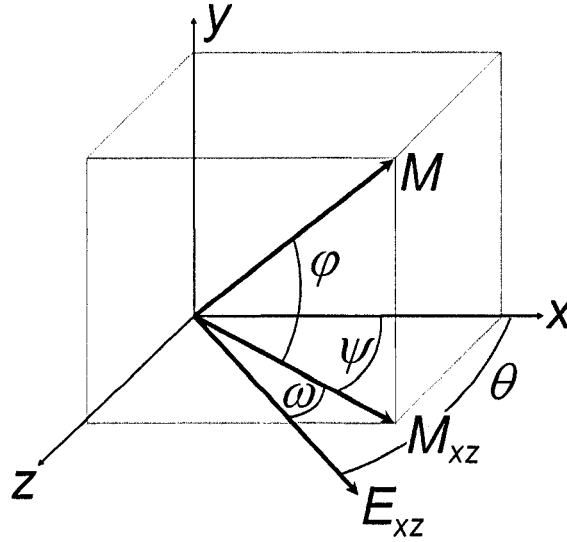


**Figure 1.4.** Schematic illustration for determining the orientation of an EDTM vector projected on to the  $xz$  plane where the  $x$  and  $z$  axes are the vibration directions. Light propagating along  $y$ .

For a measurement made in a birefringent direction, the electric field of a photon propagating in the  $y$ -direction is constrained to oscillate in one of the two orthogonal eigenmodes of the medium. The transition probabilities along these directions,  $x$  and  $z$ , become

$$W_x \propto |\epsilon_x \cdot M_x|^2 = |\epsilon_x \cdot M \cos \varphi \cos \psi|^2 = \epsilon_x \cdot M^2 \cos^2 \varphi \cos^2 \psi$$

$$W_z \propto |\epsilon_z \cdot M_z|^2 = |\epsilon_z \cdot M \cos \varphi \sin \psi|^2 = \epsilon_z \cdot M^2 \cos^2 \varphi \sin^2 \psi$$



where  $\varphi$  is the angle projecting  $M$  onto the  $xz$  plane and  $\psi$  is the angle between the subsequent vector and the  $x$ -axis (Figure 1.4) and  $\varepsilon$  is a unit vector parallel to  $E$ .

The absorption coefficients along the two eigen modes,  $\alpha_x$  and  $\alpha_z$ , are related to the probability of the  $f^{\text{th}}$  transition by the equations<sup>1</sup>

$$\alpha_x(\tilde{\nu}) = \frac{4\pi^2\tilde{\nu}}{\hbar} n' |\varepsilon_x \cdot M_{i,x}|^2 \frac{g'(\tilde{\nu})}{c} = \frac{4\pi^2\tilde{\nu}}{\hbar} n' |\varepsilon_x \cdot M_i \cos \varphi \cos \psi|^2 \frac{g'(\tilde{\nu})}{c}$$

$$\alpha_z(\tilde{\nu}) = \frac{4\pi^2\tilde{\nu}}{\hbar} n' |\varepsilon_z \cdot M_{i,z}|^2 \frac{g'(\tilde{\nu})}{c} = \frac{4\pi^2\tilde{\nu}}{\hbar} n' |\varepsilon_z \cdot M_i \cos \varphi \sin \psi|^2 \frac{g'(\tilde{\nu})}{c}$$

where  $\tilde{\nu}$  is the energy of the transition ( $\text{cm}^{-1}$ ),  $n'$  is the number of moles per cubic centimeter, and  $\frac{g'(\tilde{\nu})}{c}$  is a function describing the band-shape.

The differential intensity reduction,  $dI$ , for monochromatic collimated light of energy  $\tilde{\nu}$  propagating through an infinitesimally thin slice of an absorbing medium,  $dl$ , is described by the Beer-Lambert equation

$$dI(\tilde{\nu}) = -\varepsilon(\tilde{\nu}) \cdot c \cdot I(\tilde{\nu}) \cdot dl$$

where  $\varepsilon$  is the molar extinction coefficient and  $c$  is the concentration of the absorbing species. By specifying the polarization directions, this relationship is extended to linearly polarized light propagating along a birefringent direction. For the  $x$ -polarization the equations become

$$\begin{aligned}
dI_x(\tilde{\nu}) &= -\alpha_x(\tilde{\nu}) \cdot I_x(\tilde{\nu}) \cdot dl \\
dI_x(\tilde{\nu}) &= -C \cdot (\epsilon_x \cdot M_i \cos \varphi \cos \psi)^2 \cdot I_x(\tilde{\nu}) \cdot dl \\
\int_i^f \frac{dI_x}{I_x} &= \int_0^l -C \cdot (\epsilon_x \cdot M_i \cos \varphi \cos \psi)^2 \cdot dl = -C \cdot (\epsilon_x \cdot M_i \cos \varphi \cos \psi)^2 \int_0^l dl \\
\ln I_{x,f} - \ln I_{x,i} &= -C \cdot l \cdot (\epsilon_x \cdot M_i \cos \varphi \cos \psi)^2 \\
I_{x,f} &= I_{x,i} e^{-C \cdot l \cdot (\epsilon_x \cdot M_i \cos \varphi \cos \psi)^2}
\end{aligned}$$

Expressing the intensities in terms of absorbance, the equation becomes

$$I_{x,f} = I_{x,i} 10^{-A_x}$$

Likewise, the z-direction becomes

$$\begin{aligned}
I_{z,f} &= I_{z,i} e^{-C \cdot l \cdot (\epsilon_z \cdot M_i \cos \varphi \sin \psi)^2} \\
I_{z,f} &= I_{z,i} 10^{-A_z}
\end{aligned}$$

When the plane of polarization of the incident radiation is rotated by an angle  $\theta$  with respect to the  $x$ -axis, the initial intensity of the light propagating along the two eigen modes is given by

$$\begin{aligned}
I_{x,i}(\theta) &= I_i \cos^2 \theta \\
I_{z,i}(\theta) &= I_i \sin^2 \theta
\end{aligned}$$

The total transmitted intensity is the sum of the transmitted intensities along the two eigen modes.

$$\begin{aligned}
I_f(\theta) &= I_{x,f} + I_{z,f} \\
I_f(\theta) &= I_{x,i} 10^{-A_x} + I_{z,i} 10^{-A_z} \\
I_f(\theta) &= (I_i \cos^2 \theta) \cdot 10^{-A_x} + (I_i \sin^2 \theta) \cdot 10^{-A_z}
\end{aligned}$$

The angular dependence of the transmittance becomes

$$T(\theta) = \frac{I_f(\theta)}{I_i} = 10^{-A_x} \cdot \cos^2 \theta + 10^{-A_z} \cdot \sin^2 \theta$$

A geometric relationship between the orientation angle,  $\psi$ , of the EDTM and the dichroic ratio is given by the equation

$$DR = \frac{A_{\parallel}}{A_{\perp}} = \frac{\cos^2 \psi}{\sin^2 \psi} = \tan^2 \psi$$

Solving for  $\psi$  gives

$$\psi = \tan^{-1}(\sqrt{DR})$$

#### 1.4.1 Correction for Solvent Effects

Absorption spectra are frequently corrected for environmental effects when the absolute refractive indices are known. The precise perturbation of the local chemical environment on the interaction between the dye and the propagating radiation is generally unknown. Instead, corrections based

upon the concept of effective or internal fields provide a reasonable approximation for the fields in the actual solvent environment.

The effective electric field within a medium is given by the equation:

$$E_{\text{eff}}(\lambda) = \alpha(\lambda) \cdot E$$

where  $\alpha(\lambda)$  is the polarizability of the medium. The simplest procedure for determining a suitable expression for  $\alpha(\lambda)$  was derived by Lorentz. It assumes the effective electric field acting on a molecule is the average effective field over the entire solvent in the presence of a field,  $E$ . The resulting correction factor is thus

$$\alpha(\lambda) = \frac{n^2(\lambda) + 2}{3}$$

where  $n(\lambda)$  is the refractive index of the medium. The intensity of the radiation also requires a correction for the velocity of propagation through the solvent  $c/n(\lambda)$ . The final correction for absorption is thus  $[\alpha(\lambda)]^2/n(\lambda)$ ; the measured absorbance is effectively too large by this factor. While the correction is commonly ignored for measurements in weakly birefringent samples, it is significant in highly birefringent systems such as single crystals. The corrected absorbances for the two orthogonal polarizations are

$$A_{\parallel, \text{corr}} = \frac{A_{\parallel, \text{meas}} \cdot n_{\parallel}(\lambda)}{[\alpha(\lambda)]^2} = \frac{A_{\parallel, \text{meas}} \cdot 9n_{\parallel}(\lambda)}{[n_{\parallel}^2(\lambda) + 2]^2}$$

and

$$A_{\perp, \text{corr}} = \frac{A_{\perp, \text{meas}} \cdot n_{\perp}(\lambda)}{[\alpha(\lambda)]^2} = \frac{A_{\perp, \text{meas}} \cdot 9n_{\perp}(\lambda)}{[n_{\perp}^2(\lambda) + 2]^2}$$

#### 1.4.2 Fresnel Reflection Corrections

Reflection of an incident beam occurs whenever light crosses between two media having different refractive indices. For light at normal incidence, the magnitude of this effect depends on the refractive indices of the interface, the angle of incidence, and the polarization of the incoming ray. For light in which the electric field oscillates parallel to the plane of the interface (s-polarized), the reflectance,  $R_s$ , for the proportion of light reflected back is given by the equation

$$R_s = \left( \frac{n_t \cos \theta_t - n_i \cos \theta_i}{n_t \cos \theta_t + n_i \cos \theta_i} \right)^2$$

where  $n_i$  and  $n_t$  are the refractive indices of the media containing the incident and transmitted light, respectively, and  $\theta_i$  and  $\theta_t$  are trajectories of the light with respect to a vector normal to the interfacial plane. For the

orthogonal polarization of light (*p*-polarized), the reflectance,  $R_p$ , for the proportion of light reflected back is given by the equation

$$R_p = \left( \frac{n_t \cos \theta_i - n_i \cos \theta_t}{n_i \cos \theta_t + n_t \cos \theta_i} \right)^2$$

The transmittance,  $T$ , is related to  $R$  through the relationship  $R+T=1$ .

For a beam impinging on an air-glass interface at normal incidence approximately 4% of the light will be reflected back. While this reflection is equal for all incident polarizations in a medium with isotropic refractive indices, many of the measurements described herein are conducted on highly birefringent crystals ( $\Delta n \approx 0.2$ ). For light propagating through air ( $n=1.00$ ) incident on (010) of potassium acid phthalate polarized along *a* and *c* ( $n_a=1.62$ ,  $n_c=1.45$ )<sup>14</sup>, the reflectance of the two polarizations are 5.6% and 3.4%, respectively, a difference of 2.2% between the two polarizations. Thus, the impact of Fresnel reflections on measured absorbances was not considered significant and subsequent corrections were not applied in the case of normal incidence measurements on birefringent crystals.

Measurements of polymer thin films ( $n \approx 1.6$ ) were conducted at incident angles up to 40°. At this angle, if absorbance measurements are conducted

in air the reflectance is substantial,  $R_s \approx 9.6\%$  and  $R_p \approx 2.2\%$ . Conducting the experiments in light mineral oil ( $n=1.4680$ ) reduced the values to  $R_s \approx 0.50\%$  and  $R_p \approx 0.027\%$ . The absorbance of a blank substrate was subtracted from the measured polymer spectra providing an empirical correction to account for any substrate effects, including reflection.

## CHAPTER 2 - LINEAR DICHROISM OF SINGLE CRYSTALS

### 2.1 History

Quantitative spectroscopic analysis of organic dye impurities trapped within a single crystal host began in 1951 with Buckley's analysis of chromoptrope 2B oriented within crystals of potassium sulfate ( $K_2SO_4$ ) and ammonium perchlorate ( $NH_4ClO_4$ ).<sup>13</sup> The absorption spectra of the dyed crystals measured in orthogonal crystallographic directions reveal the linear dichroism present in these systems (Figure 1.3). While Buckley believed that his discovery would lead to "a new branch of chemistry", the study of dye-inclusion crystals failed to enter the mainstream of scientific research.

The linear and non-linear optical properties of dye-inclusion crystals has persisted as a topic of research in our laboratories. A combination of polarized visible absorption spectroscopy and calculations of electronic



dipole transition moments of three triphenyl methane dyes and pyranine oriented and overgrown by  $K_2SO_4$  was used to construct a sensible model for the inclusion of the dyes within the lattice.<sup>15</sup> The models supported previous researchers' hypotheses that dyes recognize ionic salts by substituting negatively charged functionalities for anions.<sup>16</sup>

Several years later, Gurney *et al.* published a study of functionalized benzene derivatives incorporated within  $K_2SO_4$ .<sup>17</sup> In addition to the routine polarized absorption measurements, the extensive characterization of the dyed single crystals also included polarized fluorescence and phosphorescence, luminescence lifetimes, a myriad of MO calculations, and single crystal EPR. Arising from the presence of two distinct and highly organized chemical species within the host, the remarkably clean EPR spectra provided researchers with enormous insight into the molecular structure of the mixed crystal. Presented herein are the results of similar EPR measurements involving larger and more complex guest and host molecules; the expansion of potential intermolecular non-covalent interactions contributes to a striking increase in the complexity of the observed EPR spectra.

“Dyeing Crystals”, the review by Kahr and Gurney, is the most comprehensive work on the history and science of organic impurities overgrown by crystals; a tome containing hundreds of examples of mixed crystal formation spanning the entire life of the field.<sup>18</sup> This paper is a critical first step for any scientist interested in the complex chemistry of dyeing crystals.

## 2.2 Dyeing Potassium Acid Phthalate

### *2.2.1 Potassium Acid Phthalate*

Seldom has a crystalline host investigated in the Kahr labs oriented and overgrown so large and diverse a collection of organic dyes as potassium acid phthalate, commonly abbreviated KAP. More than 100 dyes have been found in the lattice in millimolar concentrations. KAP is also an ideal host as it is easily grown from aqueous solution as large ( $> 10 \text{ cm}^3$ )  $\{010\}$  plates having perfect (010) cleavage. KAP crystals (polar space group  $Pca2_1$ , point group  $C_{2v}$  or  $mm2$ )<sup>19</sup> are built of layers of potassium and hydrogen phthalate ions stacked along [010] (Figure 2.1). The absolute configuration of the polar [001] axis to which all  $hkl$  indices refer was determined by the

anomalous dispersion of X-rays and is consistent with the assignment made previously.<sup>20</sup> The macroscopic polarity of the *c*-axis admits second order non-linear optical properties. As such, we can consider coupling of guest-host optical non-linearities.

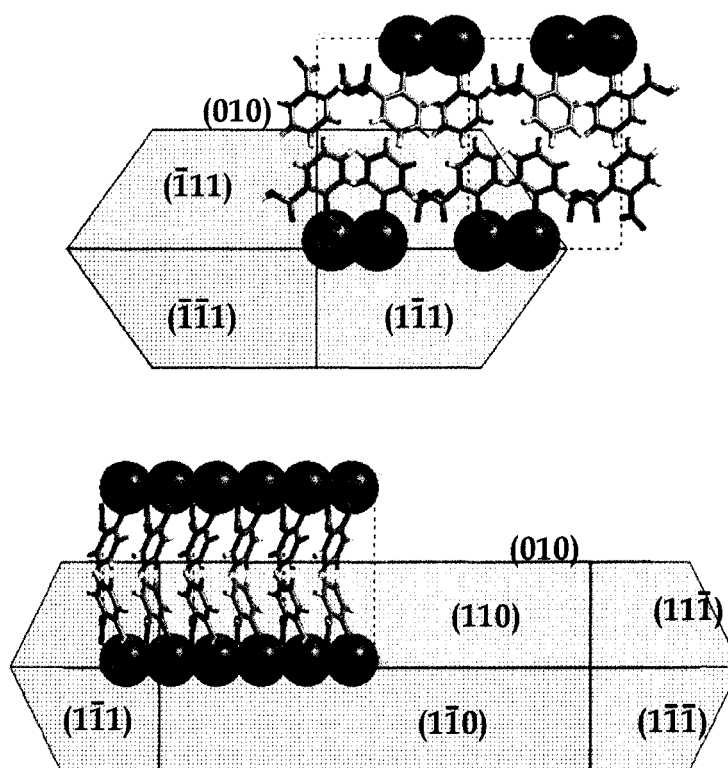


**Figure 2.1.** Crystal structure and idealized habit of KAP viewed down [100]. The horizontal axis is *c* and the vertical axis is *b*. Green spheres represent potassium ions.

KAP possess a highly regular habit with the following forms:  $\{010\}$ ,  $\{111\}$ ,  $\{11\bar{1}\}$ ,  $\{110\}$ , and very seldom  $\{121\}$ . Dyed crystals typically show patterns of color consistent with symmetry distinct facets having different affinities for the chromophores, intersectorial zoning. Dyes are thus contained in polyhedral growth sectors, sub-volumes of the crystals that have grown through particular faces. The highly luminescent growth sectors containing the positively charged basic fuchsin (**BF**) and negatively charged sulforhodamine 101 (**SR**) illustrate not only the dye's pronounced facial selectivity, but additionally reflect the presence and chemical sensitivity of the polar *c*-axis (Figure 2.2). While cationic and anionic species generally incorporate within  $\{11\bar{1}\}$  and  $\{111\}$  of KAP respectively, these trends cannot be reduced to firm rules.

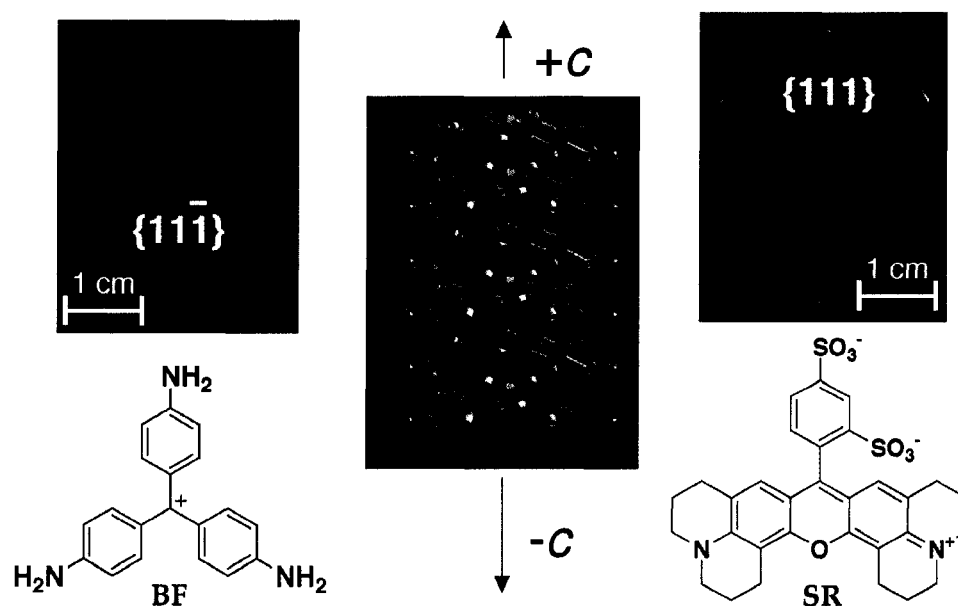


**Figure 2.2.** Images of black light (366 nm) irradiated KAP crystals (1 cm wide) grown in the presence of **BF** and **SR**. The crystals are similarly oriented with respect to the polar  $c$ -axis indicated in the view of the lattice along  $[010]$ . Indices of bright red growth sectors are indicated.

## 2.2.2 Diamino Acridine in Potassium Acid Phthalate

### 2.2.2.1 Diamino Acridine

KAP crystals grown in the presence of 3,6-diaminoacridine (**DAA**) provide one of the most striking examples of the complex non-covalent chemistry governing crystal growth from solution.<sup>21</sup>

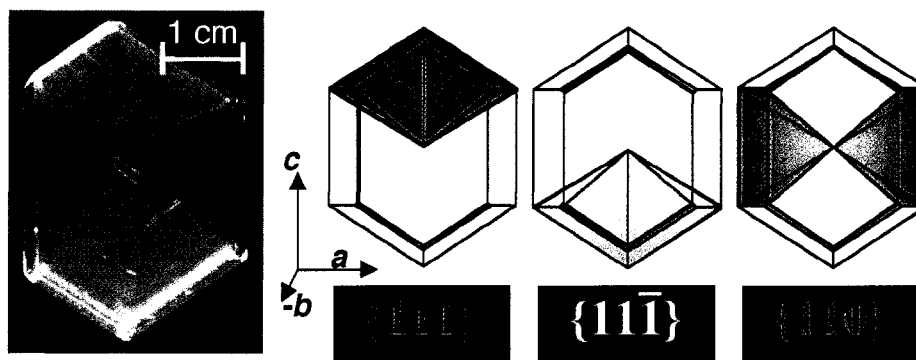


**Figure 2.3.** Fluorescence image of a KAP crystal (left) grown in the presence of **DAA** with idealized representations of the habit indicating the growth sectors and their respective colors of luminescence. The arrows indicate crystallographic directions of KAP.

In addition to recognizing  $\{111\}$  and  $\{11\bar{1}\}$ , the complimentary ends of the KAP polar axis, **DAA** also recognizes  $\{110\}$ . Each of these three crystallographically unique growth sectors emits a unique color of luminescence appearing yellow, green and red, respectively. Because of the complex pH chemistry of **DAA**, the colors presumably arise from the dye being overgrown in different states of protonation: commonly observed forms include neutral (**DAA**), monocation (**DAA**• $\text{H}^+$ ), and dication (**DAA**• $\text{H}_2^{2+}$ ).<sup>25</sup>

Large single crystals of KAP containing 3,6-diamino acridine were grown from aqueous solutions by slow evaporation at room temperature. Solutions were prepared by combining a 0.5 M KAP stock solution with an appropriate mass of **DAA** dissolved in a minimal amount of neat ethanol (typically 10-20 mL). Dark cabinets provided an ideal crystal growth environment by minimizing turbulent air circulation and avoiding potential photodegradation of the dye. Optimal '*tri-colore*' crystals were precipitated from growth solutions initially containing  $1.0 \times 10^{-4}$  M **DAA**. At this concentration, the mixed crystals contained the maximum amount of dye while maintaining sufficient contrast of the luminescence between the individual growth sectors. Absorbance measurements of dissolved crystals grown from  $10^{-4}$  *m* **DAA** solutions, where *m* equals moles of dye per kg of host, indicated that the concentration of **DAA** was  $10^{-5}$  *m* in the  $\{11\bar{1}\}$  sector.

Crystals were grown at higher initial dye concentrations ( $1.0 \times 10^{-3}$  M **DAA**), however the addition of 18% butanol and 9% ethanol was required for dye solubility. The resulting crystals lacked contrast between the  $\{111\}$  and  $\{11\bar{1}\}$  growth sectors; both sectors exhibited similar green luminescence. The habit of KAP was not significantly modified at any dye concentration examined.

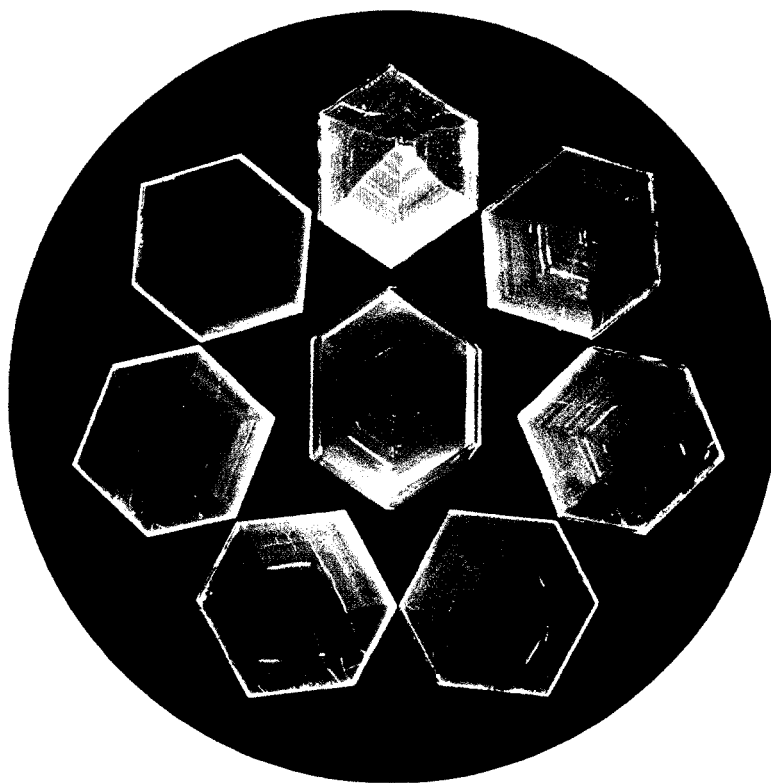


**Figure 2.4.** Contrast enhanced digital image of a KAP single crystal (center) grown in the presence of **DAA**. 200  $\mu\text{m}$  slices surround the crystal that run clockwise from 12:00 beginning with the underside. Faint luminescence (contrast enhanced) from the (010) sector is observed in the slices at 7:00 and 8:00 positions.

**DAA** also occasionally recognizes (010); a minor species in terms of luminescence intensity relative to the other three sectors (Figure 2.4). Although the optical properties of this species have not been characterized, the polygonal patterns of luminescence emitted from {010} indicate that this



species is not homogenously distributed within this growth sector. Unlike the *intersectorial* zoning observed in  $\{111\}$ ,  $\{11\bar{1}\}$ , and  $\{110\}$ , this *intrasectorial* zoning results from the selective affinity of the dye for chemically unique structures found on (010).<sup>22</sup>

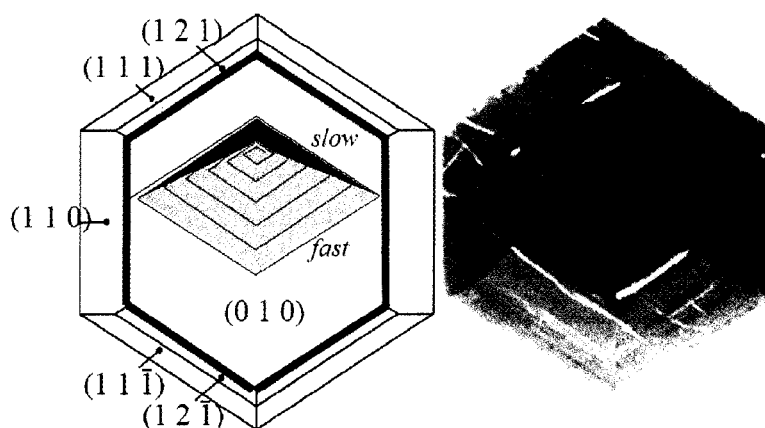


**Figure 2.5.** Left: Idealized KAP habit with absolute indices viewed down *b*-axis including (010) growth hillocks illustrating the expected patterns of luminescence from dyes recognizing the fast slope (orange) or the slow slope (blue). Right: Crystal slice from Figure 2.4 illustrating patterns of dye luminescence consistent with fast slope recognition.

The topology of (010) is a consequence screw dislocations formed during crystal growth.<sup>23</sup> These dislocations form a step edge that spirals around the dislocation core resulting in small shallow hills known as hillocks (Figure 2.5). Because the steps propagate along the chemically unique  $+c$  and  $-c$

directions, they possess different chemical structures and growth rates; growth in the “fast”  $-c$  direction is about 10 times faster than in the “slow”  $+c$  direction.<sup>24</sup> The selectivity of a luminescent dye for either the fast or slow slopes will result in the emission of a unique pattern of light resembling either diamonds or chevrons, respectively (Figure 2.5). The diamond-like emission patterns observed on (010) suggest that **DAA** recognizes and is overgrown by the fast slopes of hillocks on this face.

#### 2.2.2.2 Optical Properties of Diamino Acridine in Potassium Hydrogen Phthalate

The visible  $\lambda_{\max}$  for {110} and {111} are 481 and 460 nm, respectively (Figure 2.6). The spectrum for {11 $\bar{1}$ } is intermediate and is a superposition of the bands characteristic of {110} and {111}. The pH dependence of **DAA** has been examined previously.<sup>25</sup> The predominant species at neutral pH is **DAA**•H<sup>+</sup> ( $\lambda_{\max}$  = 445 nm). Protonation to **DAA**•H<sub>2</sub><sup>2+</sup> results in a hypsochromic shift of the absorption maxima ( $\lambda_{\max}$  = 455 nm) and the appearance of a small companion peak found in the UV region ( $\lambda_{\max}$  = 365 nm). Deprotonation of the monocation to **DAA** induces a bathochromic shift of the principle visible transition ( $\lambda_{\max}$  = 390 nm).

As the neutral species is only observed under basic conditions, its presence in the acidic KAP solutions and single crystals was considered highly unlikely and subsequently ruled out. The peak at 460 nm has been assigned as  $\text{DAA}\cdot\text{H}^+$  while the band at 481 nm has been assigned as  $\text{DAA}\cdot\text{H}_2^{2+}$ . The absorption maxima of both species are red-shifted by 10-20 nm relative to solution. Additionally, a similarly red-shifted small peak ( $\lambda_{\text{max}} = 380 \text{ nm}$ ) characteristic of  $\text{DAA}\cdot\text{H}_2^{2+}$ , found only in  $\{110\}$  and  $\{11\bar{1}\}$ , supports the assignment of this species to these sectors. The photoluminescence energy maxima for  $\{111\}$  and  $\{110\}$  were 519 and 542 nm, respectively. Again,  $\{11\bar{1}\}$  was intermediate emitting at 531 nm.

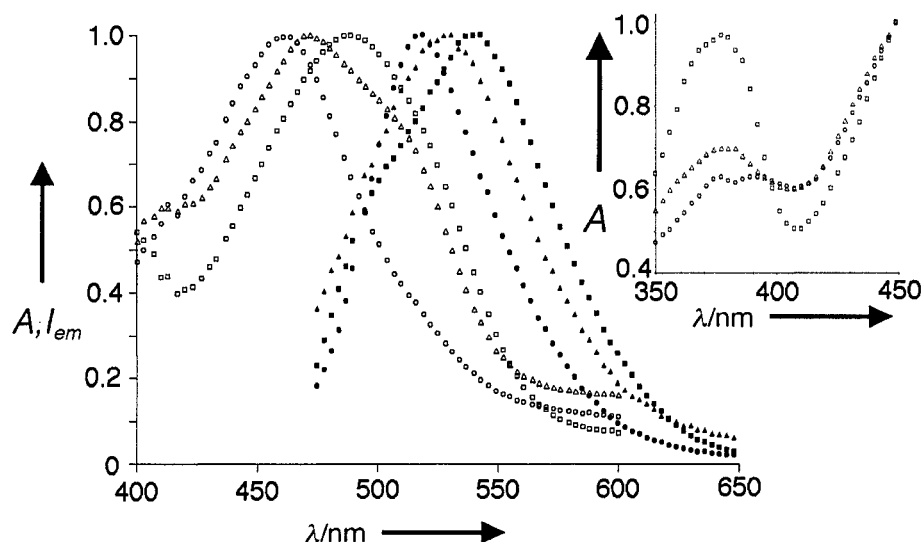


**Figure 2.6.** Absorption (open) and luminescence (solid) spectra for the individual  $\{111\}$  ( $\circ$ ),  $\{11\bar{1}\}$  ( $\Delta$ ), and  $\{110\}$  ( $\square$ ) sectors of KAP with DAA.

Linear dichroism of the main transitions was pronounced in all three sectors examined. Absorption spectra were measured along the vibration directions of the crystal:  $[100]$  and  $[001]$  for light incident on  $(010)$ ,  $[010]$  and  $[001]$  for light incident on  $(001)$ .<sup>\*</sup> The EDTM for the strongest transition is

---

<sup>\*</sup>  $(010)$  plates were prepared by cleaving the crystal by pressing a razor blade against the crystal parallel to this surface.  $(001)$  plates were first removed using a wet wire saw then polished until suitable optical transparency was achieved using a ground glass surface wetted with isopropyl alcohol.

oriented  $33^\circ \pm 3^\circ$ ,  $25^\circ \pm 3^\circ$ , and  $27^\circ \pm 3^\circ$  from  $[100]$  in the  $ac$  plane for  $\{111\}$ ,  $\{110\}$  and  $\{11\bar{1}\}$ , respectively. In the  $bc$  plane, the EDTM in the same growth sectors is oriented  $39^\circ \pm 3^\circ$ ,  $38^\circ \pm 3^\circ$ , and  $22^\circ \pm 3^\circ$  from  $[010]$ . Establishing a molecular orientation within the lattice on the basis of the orientation of the EDTM proved more complex than anticipated.

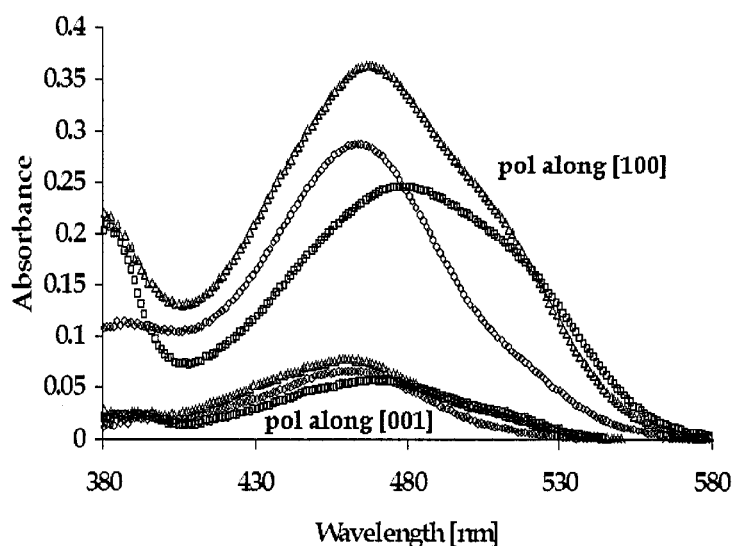


**Figure 2.7.** Linear dichroism spectra measured with light polarized along  $[001]$  and  $[100]$  incident to  $(010)$  for the individual  $\{111\}$  ( $\circ$ ),  $\{11\bar{1}\}$  ( $\Delta$ ), and  $\{110\}$  ( $\square$ ) sectors of KAP with **DAA**. The strongest absorbance for each sector occurs when the light is polarized along  $[100]$ .

While the order of protonation of **DAA** has been established for solutions, the anisotropy of the local chemical environment within the host can easily influence this order. These changes will affect the symmetry of the guest and result in different EDTMs for **DAA** of like charge.

To determine the EDTMs, the appropriate **DAA** species was constructed and its geometry optimized using the CVFF\_300\_1.01 force field<sup>26</sup> found in the open force field suite (OFF methods) of the molecular mechanics based *Cerius<sup>2</sup> minimizer*. The UV/visible absorption spectra of the minimized **DAA** structures were then determined using the INDO/1 Hamiltonian of the semi-empirical *Cerius<sup>2</sup> ZINDO* package. This package provides the EDTM vector and oscillator strength ( $f$ ) for each peak in the calculated absorption spectrum. The EDTM of the strongest transition, based on oscillator strength, occurring in the visible or long-wave UV region for each **DAA** species is shown in Figure 2.8. When a second strong transition (with an oscillator strength greater than 50% of the strongest transition) was observed in this region, both transitions were listed.

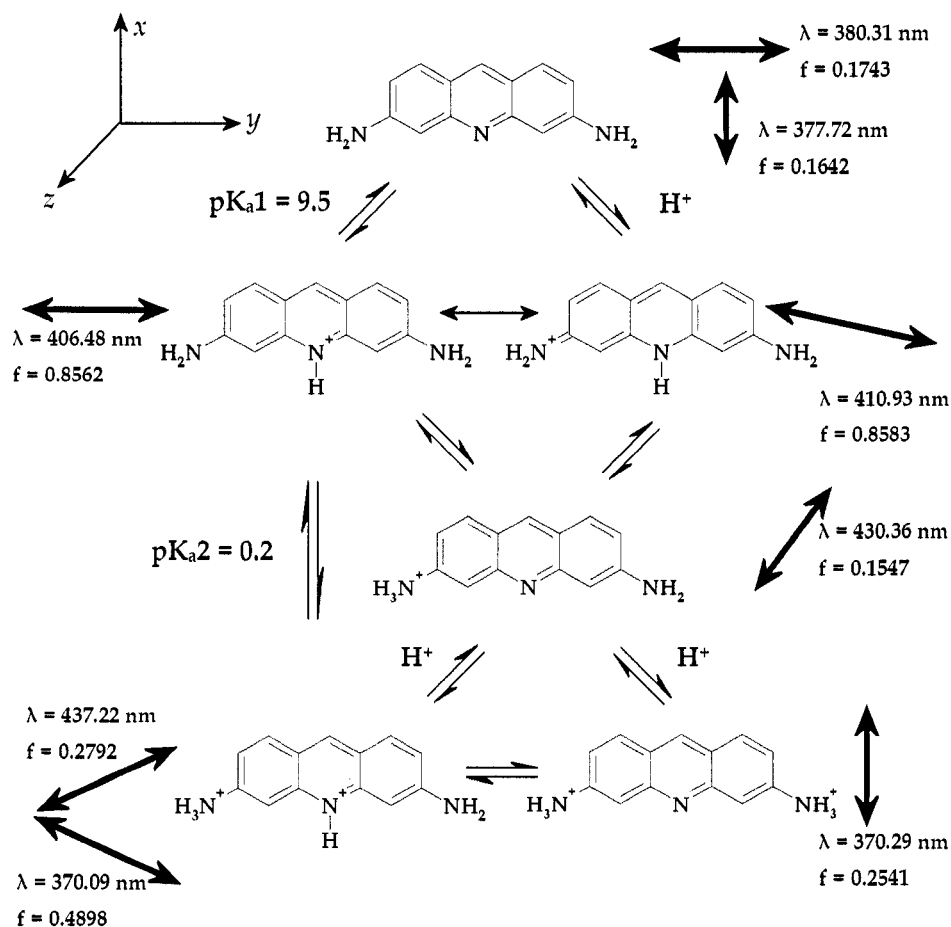


**Figure 2.8.** Protonation scheme for DAA including the ZINDO calculated EDTM vector, wavelength and oscillator strength,  $f$ , of the strongest visible transition(s) for each chemical species. In the case of two strong transitions of comparable energy, both transitions are given.  $pK_a$  values are given for solution equilibria previously reported in the literature.<sup>25</sup> Cartesian coordinates in upper left describe the molecular framework used in the TR-EPR studies. (section 2.2.2.3 )

In contrast to rod-like chromophores whose strongest visible transition is typically co-linear with the long axis of the molecule, the strongest transitions for **DAA** assume numerous directions within the molecular framework (Figure 2.8). While every strong transition is confined to the molecular *xy* plane, **DAA** possess two transitions, nearly equal in intensity but having orthogonal polarizations. The mono and di-cation exhibit markedly different transition orientations depending on the location of added protons.

While the assignment of the protonation site for the monocationic species is highly uncertain, the dication within the crystal is likely to be the species containing the pyridinium proton; the x-ray structure of this species has been determined<sup>27</sup> and ZINDO calculations show two strong transitions in the UV/visible region, the second transition being the UV companion peak observed in the crystal spectra. However, the general uncertainty of the **DAA** species and their associated transitions precludes modeling of the guest within the lattice solely on the basis of the dichroism of the visible transitions.

Moreover, recent studies of single molecules within KAP matrices reveal that guests can adopt a wide range of orientations.<sup>28</sup> In this report, guests



bearing no size or shape similarity to the host are oriented and overgrown as evidenced by the bulk dichroism of the dyed crystals. In the case of violamine R, the luminescence anisotropy of individual molecules revealed a vast array of orientations ranging from  $20.1^\circ$  to  $72.9^\circ$  relative to [100]. The average value for 108 molecules was  $42.3^\circ$  from [100], very close to the bulk values of  $44.5^\circ$  and  $45.0^\circ$  determined from absorption spectroscopy. As **DAA** also lacks strong isomorphism with the host, it is not unreasonable to surmise that the distribution of orientations within the lattice is large despite the pronounced linear dichroism.

#### *2.2.2.3 Time-Resolved Electron Paramagnetic Resonance Experiments*

Some doped-KAP crystals continue to luminesce for several seconds after the excitation source is removed. As long-lived luminescence is often the result of magnetically active triplet states in acridines<sup>29</sup>, we sought a collaboration with the group of Professor Marina Brustolon (University of Padova) to carry out time resolved-electron paramagnetic resonance (TR-EPR) measurements on isolated single crystal sectors of **DAA** dyed KAP.<sup>30</sup> The relatively narrow EPR lines enable the identification of sub-populations not detected in broader visible absorption spectra.

The triplet excited state of **DAA** involves two unpaired electrons as **DAA** possesses a singlet ground state. The three non-degenerate spin states of two unpaired electrons are described by the spin quantum numbers,  $m_s = -1, 0, +1$ . The degeneracy of these states, even in the absence of an external field, is lifted by the presence of dipole-dipole interaction between the electrons. The energy gap between these states is known as the zero-field splitting (ZFS) and increases in the presence of an external field. The selection rule for transitions between spin states is  $\Delta m_s = \pm 1$  resulting in two signals in the EPR spectrum: transitions between the  $m_s = 0$  and  $m_s = +1$  states and the  $m_s = 0$  and  $m_s = -1$  states.

For the analysis of the **DAA** EPR data, the Brustolon group utilizes a Hamiltonian consisting of Zeeman and electron-electron dipolar terms:

$$\hat{H} = \mu_B S g B + S D S$$

where  $\mu_B$  is the Bohr magneton,  $B$  is the applied field,  $g$  is a tensor which describes the anisotropy of a radical's  $g$ -factor,  $S$  is the spin operator, and  $D$  is the dipolar traceless tensor. For simplicity, the principle directions of  $g$  and  $D$  were assumed to be aligned.

Because the ZFS parameters of the triplet depend on the conformation and protonation state of the dye, the spectra of frozen glassy solutions were measured in 1:1 propionitrile/butyronitrile (PBCN) and 1:4 glycerol/water mixtures at various pHs. The species assigned to the ZFS obtained at these pHs was chosen in accordance with the room temperature equilibria.<sup>25</sup> Comparing the ZFS of these solutions to those obtained from powdered polycrystalline dyed KAP sectors enabled the determination of the protonation state of triplet **DAA** species within the growth sector.

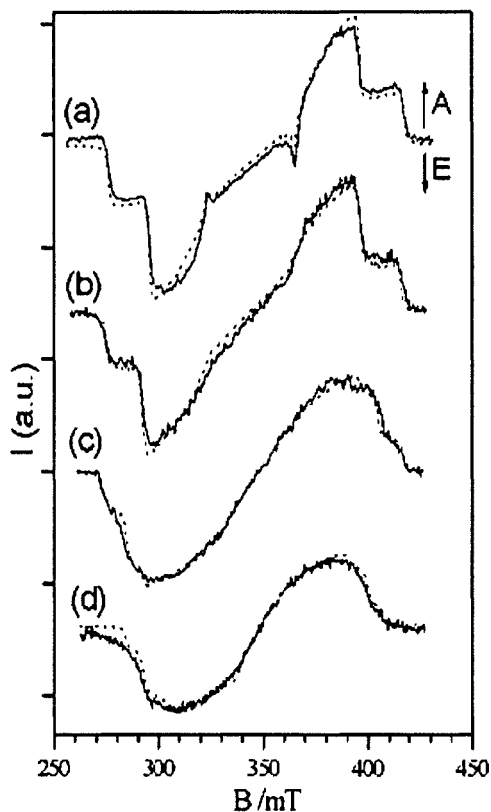


**Figure 2.9.** TR-EPR spectra at 80 K and simulation (dots) of **DAA** excited at 420 nm in (a) PBCN, and glycerol/water solutions (1:4) at different pH values: (b), pH = 12, (c) pH = 5, (d) pH = 2.

The spectrum measured in an aprotic PBCN matrix was similar to that obtained in the pH = 12 glycerol/water solution. The ZFS parameters  $D_{xx} = -0.0132$ ,  $D_{yy} = -0.0315$ ,  $D_{zz} = 0.0447$  cm<sup>-1</sup> and  $D_{xx} = -0.0126$ ,  $D_{yy} = -0.0324$ ,  $D_{zz} = 0.0450$  cm<sup>-1</sup>, respectively, are assigned to **DAA**. In the pH = 5 solution, shifts in the ZFS as the excitation wavelength was changed indicated that

$\text{DAA}\cdot\text{H}^+$ , the principal species at this pH, exists in two unique hydrogen bonding environments. Only one ZFS was observed at pH = 2 and is assigned to  $\text{DAA}\cdot\text{H}_2^{2+}$ .

**Table 2.1.** Eigenvalues,  $D_{ii}$ , in  $\text{cm}^{-1}$  ( $\pm 0.0005$ ) of ZFS tensors of **DAA** in glassy and polycrystalline samples. In PBCN  $g_x = 2.007$ ,  $g_y = 2.003$ ,  $g_z = 2.003$ ; in pH = 12  $g_x = 2.005$ ,  $g_y = 2.005$ ,  $g_z = 2.003$ . An isotropic  $g$  value was used in the polycrystalline samples.

	$D_{xx}$	$D_{yy}$	$D_{zz}$
PBCN	-0.0132	-0.0315	0.0447
pH 12	-0.0126	-0.0324	0.0450
pH 5	-0.0052	-0.0368	0.0420
pH 2	-0.0049	-0.0338	0.0387
{111}	-0.0048	-0.0334	0.0382
{11 $\bar{1}$ }	-0.0033	-0.0368	0.0401

For **DAA** in KAP, photoexcited triplets were observed in {111} and {11 $\bar{1}$ }; {110} was EPR silent at all temperatures and excitation wavelengths. The analysis of the powdered sectors is relatively straight forward; both sectors were well-simulated using a single triplet model (Figure 2.10).

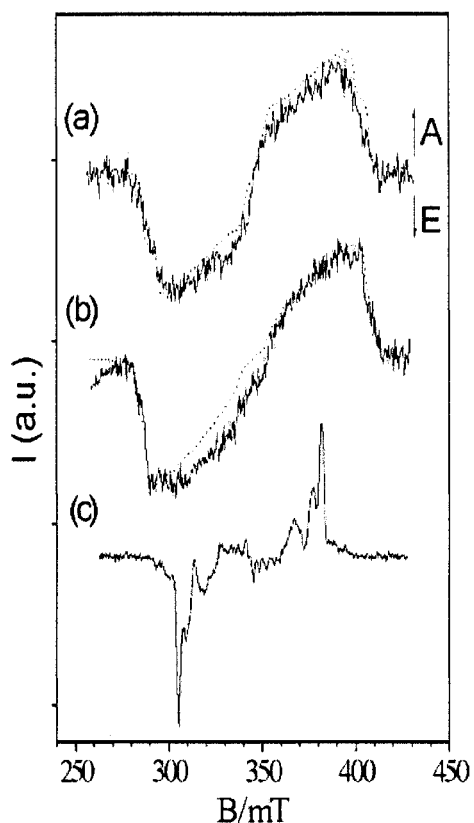


**Figure 2.10.** TR-EPR spectra of the triplet states of **DAA** in KAP. (a) Powdered sector  $\{111\}$ , (b) powdered sector  $\{11\bar{1}\}$ , and (c) single crystalline sector  $\{111\}$  with the magnetic field along the  $a$  axis. Positive lines represent absorption, negative lines indicate emission.

For the single crystal measurements, the crystal was rotated about the three crystallographic axes and a spectrum was recorded every  $7.5^\circ$ . A representative spectrum from  $\{111\}$  is shown in Figure 2.10. The angular dependencies of the EPR lines are illustrated in Figure 2.11. More than a

dozen distinct triplet orientations were observed within each sector. Such a broad distribution of orientations was surprising given the tidy single-species EPR of 2-aminonaphthalene-1,5-disulfonate in  $K_2SO_4$ .<sup>17</sup> Complete rotational curves could only be followed for the most intense signals.

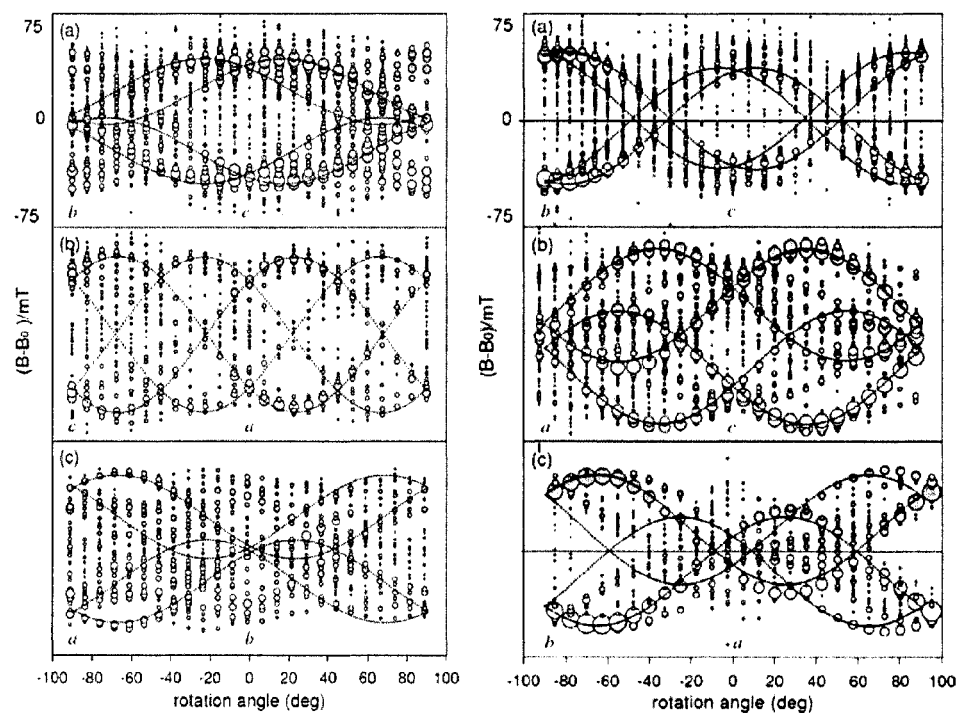


**Figure 2.11.** Angular dependencies of the resonance fields for **DAA** triplets in (left)  $\{111\}$  and (right)  $\{11\bar{1}\}$ . The area of the circle is proportional to the line intensity; open circles are for lines in emission, shaded circles represent absorption. (a), (b), and (c) correspond to rotations around the  $a$ ,  $b$ , and  $c$  crystallographic

axes, respectively. The dotted lines represent the fittings of the most intense transitions used to derive the ZFS tensor.

The six independent elements of the ZFS tensor were determined by fitting the angular dependencies to an expression derived from a first order approximation:

$$\Delta B = A\cos^2\theta + B\sin^2\theta + C\sin\theta\cos\theta$$

where  $\Delta B$  is the fine splitting of each pair of lines that varies with the orientation of the crystal. In each  $ij$  plane,  $A$  and  $B$  give the diagonal elements  $D_{ii}$  and  $D_{jj}$ , respectively.  $C$  is the off-diagonal element  $D_{ij}$  of the fine tensor in the crystal frame. Diagonalization of this tensor returns the principal values and corresponding principle directions of these values in the crystallographic framework. While the magnitudes of the ZFS for  $\{111\}$  and  $\{11\bar{1}\}$  were similar, the orientation of this tensor within the KAP lattice were not. By combining the orientation of the principal values of the crystal ZFS tensor with principle values of the molecule, a model establishing the orientation of acridine nucleus within the crystal can be determined. Inferences about the location of the nitrogenic functionalities relative to the acridine nucleus are discussed in the following section.



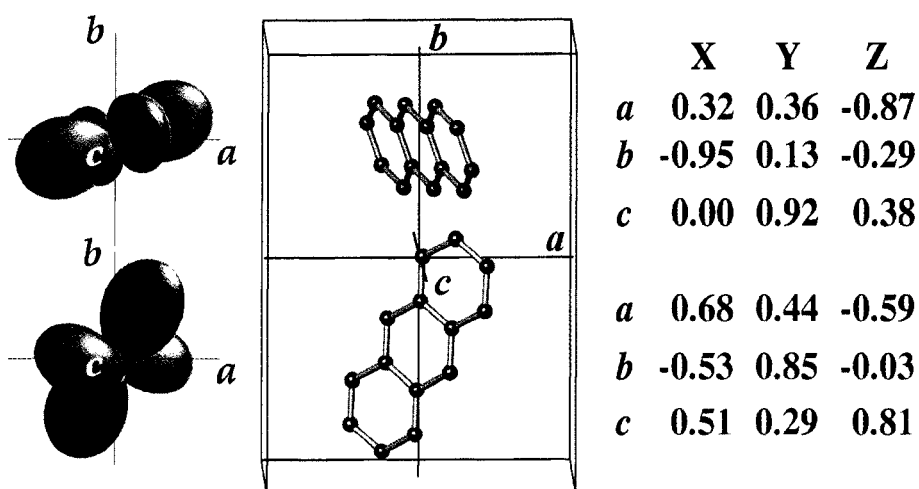


**Figure 2.12.** Left: Surface representations of the **DAA** ZFS tensor in KAP. Center: Orientation of the acridine nucleus in the KAP unit cell derived from the EPR data. Right: Direction cosines for the diagonalized ZFS tensor. Upper (blue) is {111}; lower (red) is {111̄}.

The assignment of the principal directions of the ZFS tensor to directions in the acridine molecular framework has been previously reported.<sup>31</sup> As the spin distribution of **DAA** is similar to that of acridine, the ZFS parameters  $D_{xx}$ ,  $D_{yy}$ , and  $D_{zz}$  correspond to three orthogonal directions in the molecule: parallel to the in-plane  $C_2$  axis ( $x$ ), parallel to the long axis of the molecule ( $y$ ), and perpendicular to the aromatic plane ( $z$ ), respectively (Figure 2.8). The unique orientations obtained for the ZFS tensor of the principal species

in  $\{111\}$  and  $\{11\bar{1}\}$  and the resulting **DAA** orientations within the lattice are illustrated in Figure 2.12.

#### 2.2.2.4 *Surface Calculations*

In order to understand the non-covalent interactions are responsible for the different selectivity and orientations of **DAA**, we sought an additional collaboration with the research group of Professor Andrew Rohl (Curtin University, Perth). A number of discrete surfaces can exist for a set of indices  $(hkl)$ , especially in the case of multi-component crystals. It is well established for salts that the electrostatic contribution to the lattice energy is singularly dominant; others have used only the electrostatic contribution to study surface energetics.<sup>32</sup> Using this approximation, the energetically stable surfaces and their associated electrostatic potentials can be quickly determined without going through the intensive process of deriving a force-field.

The difference between the electrostatic potential surfaces (EPS) of  $(111)$ ,  $(11\bar{1})$ , and  $(110)$  is remarkable.  $(111)$  is strongly and uniformly electropositive, the result of a preponderance of protons from carboxylic

acid groups present on this surface (Figure 2.13). In contrast, the carboxylate rich ( $11\bar{1}$ ) is strongly electronegative. Comparatively neutral (110) contains a mixture of these groups. While symmetry requires no net charge, the molecular surface for (110) is slightly negative.

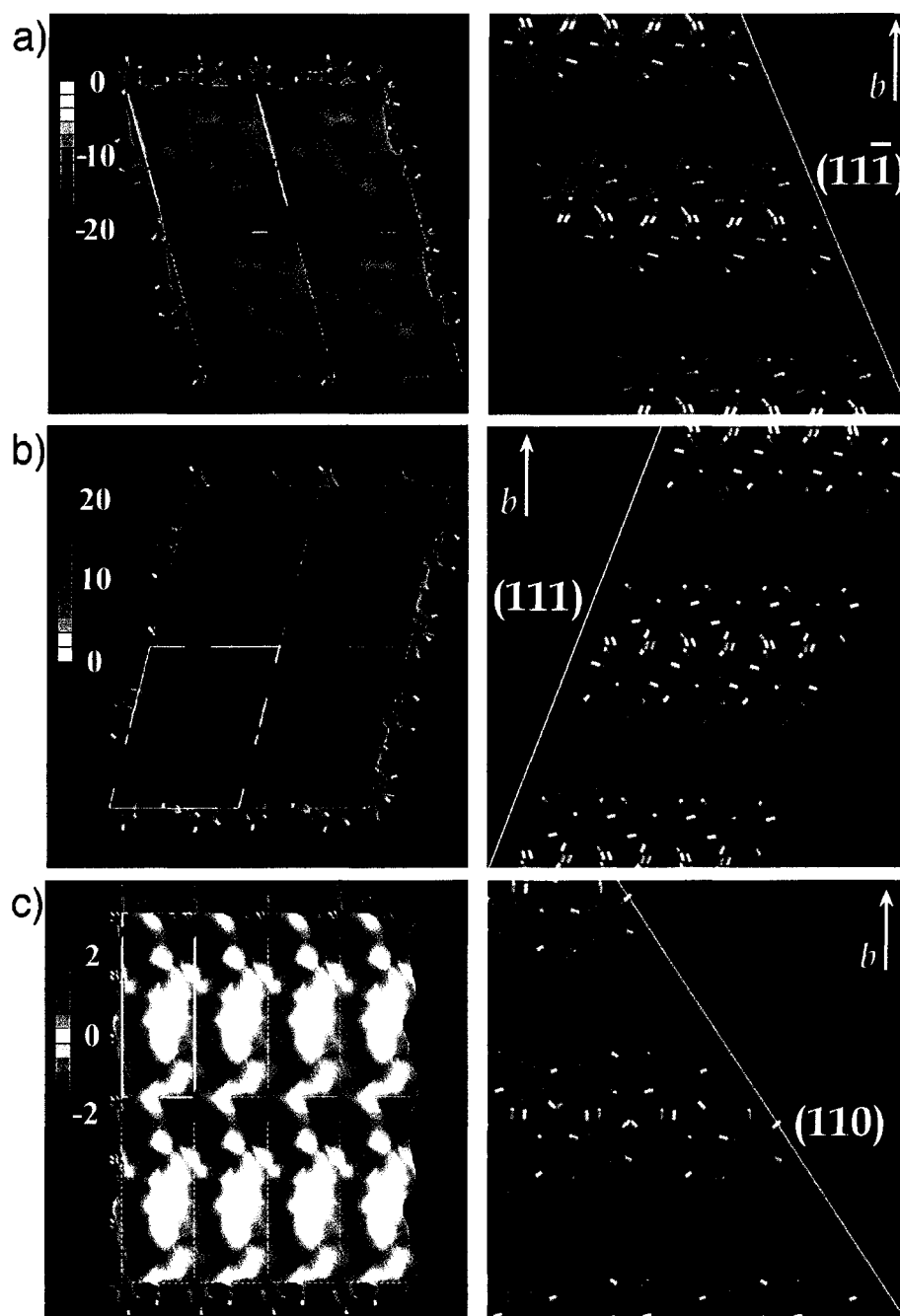


**Figure 2.13.** Left: EPS for the stable terminations of (a)  $(11\bar{1})$ , (b)  $(111)$  and (c)  $(110)$  surfaces of KAP. Red and blue regions are areas of

negative and positive potential in electron volts, respectively. Note that the scale on (c) is ten times smaller than that of (a) and (b). Right: Corresponding crystal structures of the stable terminations. All surfaces structures are viewed parallel to the plane indicated with the *b*-direction pointing towards the top of the page.

From the EPS, the general propensity for positively charged (111) and negatively charged ( $11\bar{1}$ ) to attract anions and cations, respectively, is immediately evident and is simply a consequence of electrostatic forces.

#### 2.2.2.5 Discussion

##### 2.2.2.5.1 Face Selectivity

In the case of **DAA**, the strongly negative ( $11\bar{1}$ ) sensibly adsorbs any cation, **DAA·H<sup>+</sup>** and **DAA·H<sub>2</sub><sup>2+</sup>**. The anionic carboxylate groups provide a favorable electrostatic interaction for the cationic dye. The carboxylate groups also act as complimentary hydrogen bond acceptors for the strong ammonium and pyridinium hydrogen bond donors.

The slightly electronegative (110), presenting a mixture of electronegative carboxylate groups and electropositive aromatic protons, attracts only the dication; for an electrostatic interaction to be substantive, either the field or

the corresponding charge must be large, the latter being the case in this system. On (110), the carboxylate groups are separated by a distance of 6.5 Å. The distance between a pair of oxygens in these groups measures 5.1 Å closely matching the  $N_{\text{pyridinium}} - N_{\text{ammonium}}$  distance of 4.9 Å. *Why then does the strongly electropositive (111) attract  $\text{DAA} \cdot \text{H}^+$ ?*

The acidic protons of the  $-\text{COOH}$  groups terminating (111) are strong hydrogen bond donors that compliment the pyridine and amino acceptor moieties of **DAA**. Assuming  $\text{DAA} \cdot \text{H}^+$  is drawn to the surface via a  $-\text{COOH} \cdots \text{NH}_2$  hydrogen bond, electrostatic repulsion between the surface and the dye is minimized if the long axis of the molecule remained perpendicular to the surface, precisely what is observed in the TR-EPR experiments. The hydrogen bonds are strong enough to overcome the dye-surface coulombic repulsion.

#### 2.2.2.5.2 Diamino Acridine Excited State Photophysics

The complex excited state behavior of acridines in solid matrices has been reported previously.<sup>29</sup> At ambient temperatures  $\{111\}$  and  $\{11\bar{1}\}$  exhibit long-lived high-energy luminescence (delayed fluorescence). When measured with a stopwatch, both sectors glow green ( $\lambda_{\text{em}} = 495$  and 507 nm,

respectively) for  $0.95 \pm 0.09$  seconds after the excitation sources is removed. When the sectors are then placed into a dry ice/acetone bath ( $T \approx -78\text{ }^{\circ}\text{C}$ ) the steady state luminescence appeared to the eye identical to that at room temperature. When the excitation source is removed, the luminescence persists for  $5.3 \pm 1.2$  seconds and undergoes a dramatic bathochromic shift (phosphorescence) glowing distinctly orange.

The long-lived luminescence observed in related acridines is phosphorescence.<sup>29</sup> Within several nanoseconds of electronic excitation to the first excited singlet state of **DAA** in KAP, approximately 30% of the dye molecules return to the ground state via prompt fluorescence. The fraction of molecules that do not fluoresce undergo forward intersystem crossing to a triplet excited state. Diffusion processes such as triplet quenching by oxygen are greatly reduced within solid matrices, limiting decay pathways from the triplet excited state to phosphorescence ( $T_1 - S_0$ ) and reverse intersystem crossing ( $T_1 - S_1 - S_0$ ).

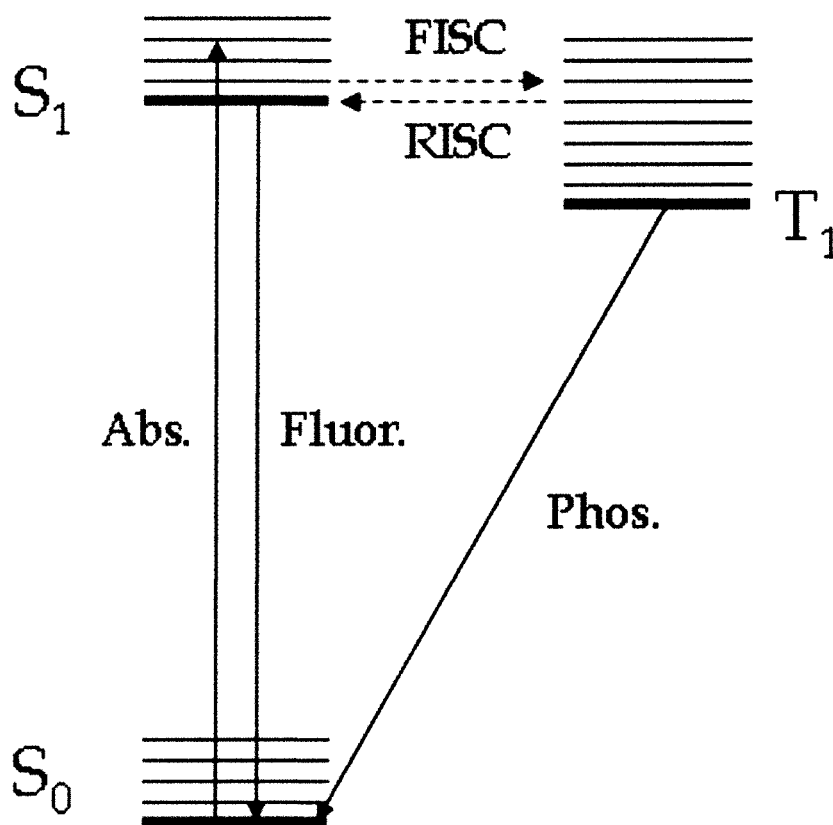


**Figure 2.14.** Energy-level diagram illustrating the decay pathways for DAA.

The reverse intersystem crossing (RISC) decay pathway dominates at room temperature; molecules in thermally populated vibrational levels of the triplet state will repopulate the singlet excited state when the thermal energy is greater than the singlet-triplet splitting energy. Upon return to the singlet excited state, the molecules promptly radiatively decay back to the



singlet ground state. At low temperatures, lacking the thermal energy required to populate the vibrational levels required for RISC, molecules phosphoresce to the ground state evidenced by the longer lifetime and bathochromic shift of the radiative emission.

#### 2.2.2.6 *Experimental*

**Crystal Growth:** The crystal growth solution was prepared by the addition of A.C.S. grade KAP (Aldrich) in deionized water (Barnsted NANOpure, 18.2 M $\Omega$ /cm) that was subsequently covered, boiled, and finally filtered through a medium grade frit filter to remove any residual particulates. Used without further purification, an appropriate amount of 3,6-diaminoacridine (Aldrich) was dissolved in a minimal amount of neat ethanol (typically 10-20 mL) before being added to the KAP solution that had equilibrated to room temperature.

The solubility data of Solc *et al.* were used for the preparation of KAP solutions and in the calculation of supersaturation.<sup>33</sup>

$$c(T) = 9.283 - 0.059 \times T + 0.0058 \times T^2$$

where  $c(T)$  is the concentration of KAP in H<sub>2</sub>O in g/L at the temperature,  $T$ , in degrees Celsius.

**X-ray crystallography:** Crystals were indexed with a Nonius KappaCCD diffractometer. After collecting a data set suitable for determining the unit cell of the sample (typically 10 frames), the diffractometer is instructed to point a specified  $hkl$  plane up, defined as the  $y$ -axis in the Nonius system. The presence of a crystal facet ( $hkl$ ) is confirmed when light impinging on the sample from a collimated lamp that is collinear, but oriented  $90^\circ$  with respect to the diffractometer CCD, results in an intense reflection off the crystal surface.

**Spectroscopy:** Solution molar absorptivities were determined with a Hitachi U-2000 spectrophotometer controlled by Spectracalc software (Galactic Industries). Crystal absorption spectra were obtained with a SpectraCode Multipoint Absorbance Imaging (MAI-20) Microscope. Freshly cleaving the upper and lower surfaces of the crystal ensuring a clean plane-parallel sample for the measurement. The extinction directions of the crystals were used to orient the sample relative to the input polarization. Pure solvents or KAP solutions, in the case of liquids, or glass slides, in the case of solids, were used as references. All spectra were background corrected.

Fluorescence spectra of solutions were made using the Jobin-Yvon Fluoromax-2. To collect the fluorescence spectra of dyed single crystals, the same instrument was fiber-optically coupled to an IMT-2 inverted Olympus microscope. To avoid the cross-contamination of the luminescence from additional domains, each sector was removed from the single crystal using a wet wire saw and measured individually. Thin slices from the underside of the crystal were removed to ensure a clean, plane-parallel surface for the measurement.

**Time-Resolved Electron Paramagnetic Resonance (measured by Brustolon in Padua):** Pieces of individual growth sectors were removed with a wet wire saw and were mounted on quartz rods along the three crystallographic axes. Spectra were recorded every  $7.5^\circ$  by rotating the crystals around the crystallographic axes. The triplet excited states were generated by 465 nm excitation with a Nd-YAG laser equipped with harmonic generators and an optical parametric oscillator. Pulses were 5 ns wide with an energy at the sample of 1 mJ/shot ca at 10 Hz. The light was conveyed into the cavity through an optical window in the cryostat (Oxford CF935) of a Bruker 380E EPR spectrometer equipped with a high quality factor (Q) dielectric cavity. The pure absorptive EPR signal, generated

under continuous microwave irradiation, was taken from the detector, preamplified and digitalized from a LeCroy 3560 digital oscilloscope. The response time of the apparatus was estimated to be around 800 ns. A surface was obtained by acquiring 50 sweeps ca of the time decay traces for different field positions. Integration with time windows of around 400 ns allowed obtaining slices along the field at the maximum of the transient signal (1  $\mu$ s after the laser flash ca).

### 2.2.3 *Rhodamine 110 in Potassium Acid Phthalate*

#### 2.2.3.1 *Materials Science – Up-conversion Solid State Dye Lasers*

Beginning in 1990, the promise of compact, portable dye lasers and the possibility of obviating the chemical waste associated with solution dyes motivated attempts to develop solid state dye lasers using polymers<sup>34</sup> and hybrid inorganic sol-gel glasses<sup>35</sup> as hosts for the dyes. Solid state dye lasers have been considered for a variety of medical applications<sup>36</sup> and are currently in use for the remote sensing of ozone from aircraft.<sup>37</sup> However, irrespective of the current uses and technological gains of SSDLs, including the first continuous-wave SSDL,<sup>38</sup> this technology has escaped wide-spread

commercial implementation; the principal issue concerning polymer and hybrid SSDLs remains the photochemical stability of the dyes within the matrices.<sup>39</sup>

Dye doped single crystals as a laser gain medium are an attractive alternative because of their higher thermal conductivity, reduced scattering, and intrinsic polarization. More importantly, the photostability of the fluorophore is enhanced due to the restriction of both intra and intermolecular dynamic processes within the lattice. Previous studies have demonstrated that single crystals doped with luminescent dyes could be fashioned into lasers (Figure 2.15), thereby extending the range of solid state dye laser (SSDL) gain media that had been restricted exclusively to polymers and glasses.<sup>40,41</sup>



**Figure 2.15.** Single crystal potassium sulfate dye laser. Square yellow object between blueish and greenish mirrors is the gain medium,  $K_2SO_4$ /pyranine (basic). Laser spot in upper left corner.<sup>18</sup>

The field of self-frequency doubled lasers (SFDLs) developed in the 1990s in parallel with the field of SSDLs. Self-frequency doubling eliminates the need for a nonlinear optical element within or external to the laser resonator.<sup>42</sup> To date, only a few frequency-doubling crystals have been synthesized with luminescent dopants. These crystals are  $LiNbO_3$ ,  $LaBGeO_5$ ,  $Ba_2NaNb_5O_{15}$ ,  $Gd_2(MoO_4)_3$ ,  $YAl_3(BO_3)_4$ ,  $BaY_4(BO_3)_3O$ ,  $CaGd_4(BO_3)_3O$  which have invariably been doped with transition metal or lanthanide ions. Such crystals are typically very difficult to grow, very expensive and lack the tuneability of conventional dye lasers.<sup>43</sup>

This work aims to unite SFDLs and SSDLs by developing single crystals doped with organic chromophores as gain media for more practical *up-conversion*<sup>44</sup> SSDLs. Such lasers are based upon an efficient second harmonic generating host crystal that can be doped with luminescent, two photon absorbing dyes.<sup>45</sup> By pumping the crystal at near infrared wavelengths, dye

dopants will be excited at the second harmonic frequency in phase matching directions in addition to two-photon absorption in directions where the second harmonic generation is minimal.<sup>46</sup>

Observed phase-matching directions for the frequency doubling of an 800 nm pump laser to 400 nm are approximately perpendicular to the  $\{11\bar{1}\}$  faces are consistent with the values reported by Belyaev *et al.*<sup>47</sup>

#### 2.2.3.2 Rhodamine 110

Rhodamine 110 (Rh110), *o*-(6-amino-3-imino-3H-xanthen-9-yl)-benzoic acid CI# [13558-31-1], is an efficient chromophore for pulsed and CW solution dye lasers.<sup>48</sup> Unlike many of the 80 other dyes we have incorporated into KAP, several of which are shown in Figure 2.16, the solid-state photophysical properties of Rh110 in the KAP lattice are similar to those in solution and in polymer matrices enabling direct comparisons of the optical properties of various materials. Additionally, absorbance spectra of dissolved crystals are identical to the solution spectra prior to crystallization indicating inclusion within the KAP lattice does not modify Rh110.

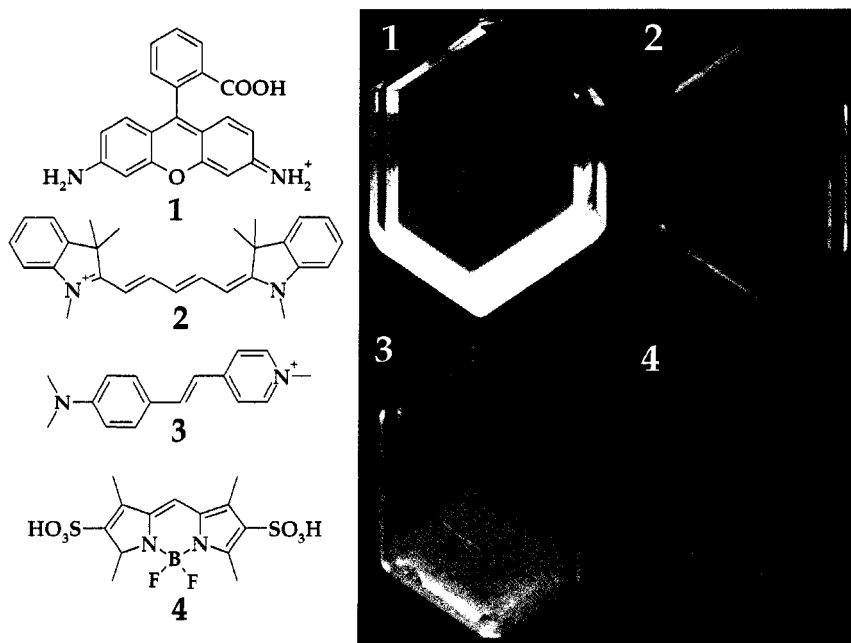


**Figure 2.16.** Photoluminescence of laser dyes doped in KAP. (1) Rhodamine 110 chloride (Rh110); (2) trans-4-[4-(diethylamino)-styryl]-1-methylpyridinium iodide (DEDASI); (3) 1, 1', 3, 3, 3', 3', hexamethyl indodicarbocyanine iodide (HIDCI); (4) 4-sulfonato-3, 3', 5, 5'-tetramethyl-2,2'-pyrromethene-1,1'-BF<sub>2</sub>. Counter-ions not drawn.

### 2.2.3.3 Mixed Crystal Growth and Characterization

Large dyed KAP crystals were grown from seeds in aqueous solutions containing  $10^{-6}$  to  $10^{-3}$  M quantities of Rh110 during programmed 5 °C temperature reduction sequences (0.5 °C/day) near 30 °C. The Rh110 was primarily contained in the four  $\{11\bar{1}\}$  growth sectors with faint inclusions in the  $\{010\}$  and  $\{110\}$  growth sectors. Absorbance measurements of a



dissolved crystal grown from  $4.9 \times 10^{-4} m$  dye solutions, where  $m$  = moles of dye/kg of host, indicated that the concentration of Rh110 in  $\{11\bar{1}\}$  was  $3.6 \times 10^{-6} m$ .

Rh110 is incorporated in the negative direction of the polar  $[001]$  axis, by adsorbing to the  $\{11\bar{1}\}$  faces in preference to  $\{111\}$ , verified by anomalous dispersion of x-rays during crystal indexing. The selectivity is presumably an electrostatic consequence of the fact that  $\{111\}$  faces are OH rich, whereas on the  $\{11\bar{1}\}$  faces display the negatively charged carboxylate groups which attract the cationic dye.

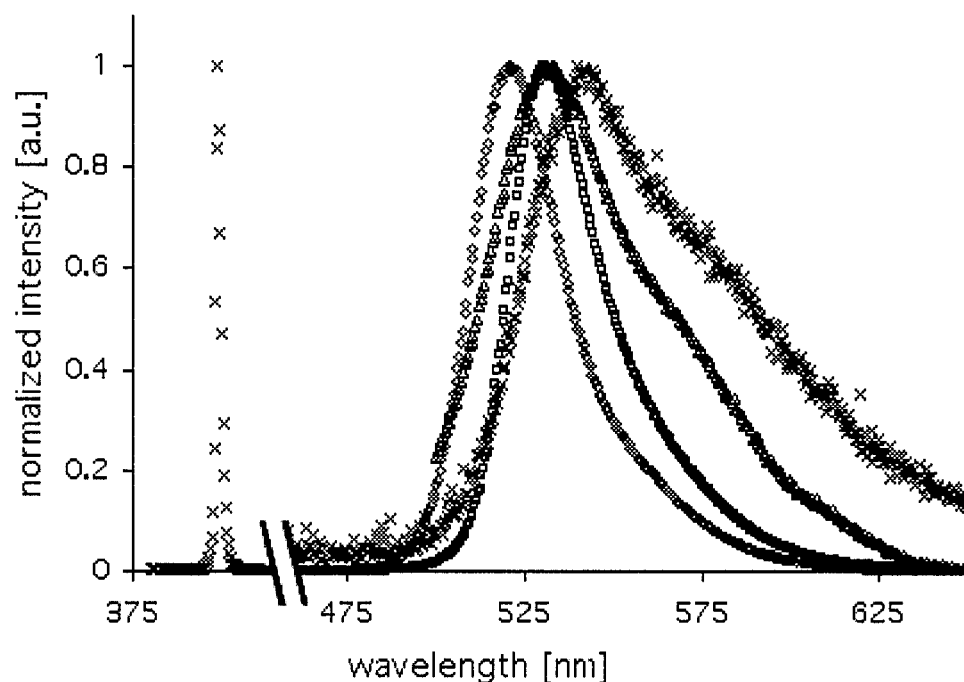


**Figure 2.17.** Normalized one photon luminescence spectra of Rh110 ( $\lambda_{\text{ex}} = 400$  nm) in water ( $\diamond$ ), KAP solution ( $\square$ ), KAP crystal ( $\triangle$ ), and up-conversion ( $\lambda_{\text{ex}} = 800$  nm) of Rh110 in KAP crystal ( $\times$ ).

The absorption maximum of Rh110 is 498 nm in water, 502 nm in a saturated KAP solution, and 505 nm in the crystal. The luminescence maxima were 523 nm, 532 nm, 532 nm, respectively (Figure 2.17). Upon irradiation with an 800 nm laser close to the phase matching direction<sup>49</sup>, a sharp 400 nm band was observed (SH) in addition to the dye luminescence maximum at 544 nm. The dyes are oriented within the lattice as evidenced by the fluorescence anisotropy where  $I_{\parallel}/I_{\perp}$  (532 nm) = 0.62.

Lifetime measurements of Rh110 dyed KAP crystals were carried out on a Photon Technology International pulsed nitrogen dye laser fluorescence lifetime spectrometer. The instrument response function was determined by placing a crystal of pure KAP, similar in size and shaped to the dyed crystal, within the sample cavity. The luminescence lifetime of Rh110 in KAP ( $\lambda_{\text{ex}} = 400 \text{ nm}$ ,  $\lambda_{\text{em}} = 532 \text{ nm}$ ) was measured to be  $3.7 \pm 0.2 \text{ ns}$ .

The photoluminescence efficiency ( $\Phi_{\text{PL}}$ ) of a Rh110/KAP crystal was determined using the method proposed by Palsson and Monkman for determining the  $\Phi_{\text{PL}}$  of luminescent thin films<sup>50</sup> using a Jobin-Yvon Fluoromax-2 fluorimeter fiber-optically coupled to a Newport integrating sphere where

$$\Phi_{\text{PL}} = \frac{E_i(\lambda) - (1 - A)E_o(\lambda)}{L_e(\lambda)A}$$

and

$$A = \frac{L_o(\lambda) - L_i(\lambda)}{L_o(\lambda)}$$

$E_i(\lambda)$  and  $E_o(\lambda)$  are, respectively, the integrated luminescence intensities (500-650 nm) resulting from direct and indirect excitation of the dyed crystal, the indirect measurement providing a correction for secondary

excitation due to scattering within the sphere.  $A$  is the sample absorbance determined by measuring the integrated excitation (380-420 nm) intensities  $L_i(\lambda)$ ,  $L_0(\lambda)$ , and  $L_e(\lambda)$  resulting from direct crystal excitation, indirect excitation, and an empty sphere, respectively. Using this approach, the  $\Phi_{PL}$  for a 2.4 mm thick slice of Rh110 dyed KAP was determined to be  $8.1 \pm 10\%$ . While this value is lower than typical efficiencies of 50% reported in polymer<sup>51</sup> and sol-gel matrices<sup>52</sup>, our value was measured far from resonance in keeping with the self-doubling theme.

#### 2.2.3.4 Photostability Measurements

Photobleaching experiments were carried out to assess the improvement single crystal isolation affords when compared to traditional polymer doping. A slice of a KAP crystal and a polyvinylalcohol (PVA) film (80% hydrolyzed  $MW_{ave} = 9,000-10,000$ ), both prepared from solutions containing equivalent dye mole ratios, were mounted on an inverted microscope using an 800 nm femtosecond laser excitation source.

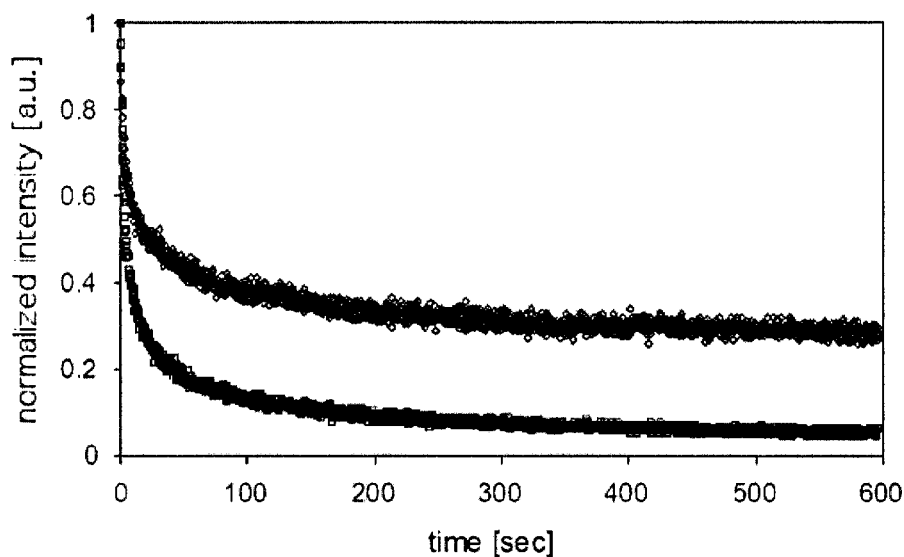


**Figure 2.18.** Normalized up-conversion luminescence of Rh110 in KAP (upper) and PVA (lower) as a function of time ( $\lambda_{\text{ex}} = 800 \text{ nm}$ ,  $P_{\text{ave}} = 1.0 \text{ mW}$ ).

The up-conversion fluorescence was measured as a function of time. As illustrated in Figure 2.18, dyed KAP crystals exhibited persistent luminescence compared with doped PVA. Scans of the surfaces of the crystal and polymer, for excitations of  $<5 \text{ mW}$  average power, indicated that the loss of fluorescence intensity was the result of fluorophore degradation, rather than the failure of the host.

#### 2.2.3.5 *Laser Cavity*

Without taking special steps to find the phase matching direction, crystals placed in the beam path of the excitation source emitted both the violet second harmonic signal of the source, as well as the dye luminescence. Initial attempts to demonstrate up-conversion lasing using an femtosecond pulsed 800 nm excitation source and the cavities described below were unsuccessful. We therefore attempted to construct a cavity suitable for traditional lasing with a 355 nm excitation source using the dyed crystal as a gain medium.

Two cavity configurations were utilized in the attempts to demonstrate lasing: the linear standing wave cavity and the offset standing wave cavity. In both cases, the soundness of the cavity was demonstrated using a solution of Rh110 ( $10^{-3}$  M) in EtOH in a 1 mm<sup>2</sup> quartz cuvette. The medium was optically pumped by a Q-switched frequency tripled Nd:YAG operating at 355 nm pulsed at 30 Hz with a 7 ns pulse width. Optical components were aligned using a 5 mW HeNe (CW) laser. The pump beam was de-magnified from 10 mm to 2.5 mm just prior to the sample cavity. The cavity was considered viable when strong green emission exiting the

output coupler was accompanied by the coherent specular reflections characteristic of lasers.

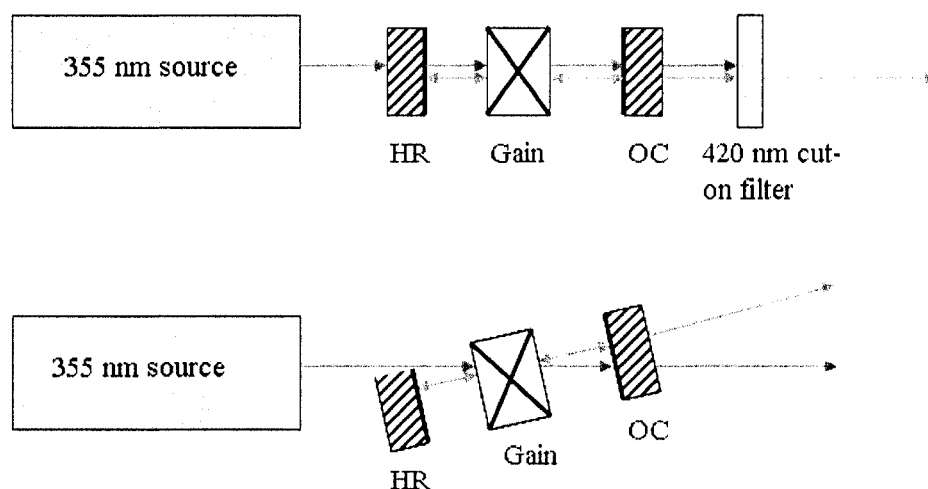


**Figure 2.19.** Schematic representations of the linear standing wave cavity (upper) and the offset standing wave cavity (lower). Blue arrows indicate 355 nm pump beam trajectory; green arrows represent the trajectory of the gain emission. HR = high reflector; OC = output coupler.

The linear standing wave cavity was constructed first, as alignment is straight forward and the close proximity of the mirrors to the gain medium reduced losses due to scattering. The 1.5 cm long cavity was constructed with high reflector and output coupler mirrors (reflectivities of >99% and 87% at lasing wavelengths, respectively) sandwiching the gain medium.

While lasing in this configuration was obtained quickly with the solution as the gain medium, input powers needed to generate lasing easily damaged the highly reflecting mirror in this geometry.

To construct the offset cavity, mirrors in the linear arrangement were offset by about  $15^\circ$  from the optical pump beam path by a combination of rotation and cavity elongation. This low offset angle provided good co-linearity between the laser gain and the pump beam. A consequence of the low offset angle meant that our cavity spacing was now 20 cm, much longer than the linear cavity, requiring alignment of higher precision. Again, the principle benefit of this cavity geometry was avoiding damage to the high reflectance mirror with the pump.

Prior to placement within the laser cavity, the dyed crystals (1-3 mm thick) were cleaved, proving a sample with smooth, clean, plane parallel surfaces. Unfortunately at powers well below the lasing threshold, small plumes were observed rising from the crystal. Inspection of the crystal revealed the material had begun to burn at the laser site with rings of interference fringes visible within the crystal below the pit.



Numerous crystals were mounted in different orientations (face parallel to pump, parallel to cavity mirrors, skewed geometries, etc...) however, decomposition of the material persisted. Inclusion of the dye within the lattice greatly reduced the damage threshold for KAP as undyed crystals mounted within the cavity easily passed the pump radiation.

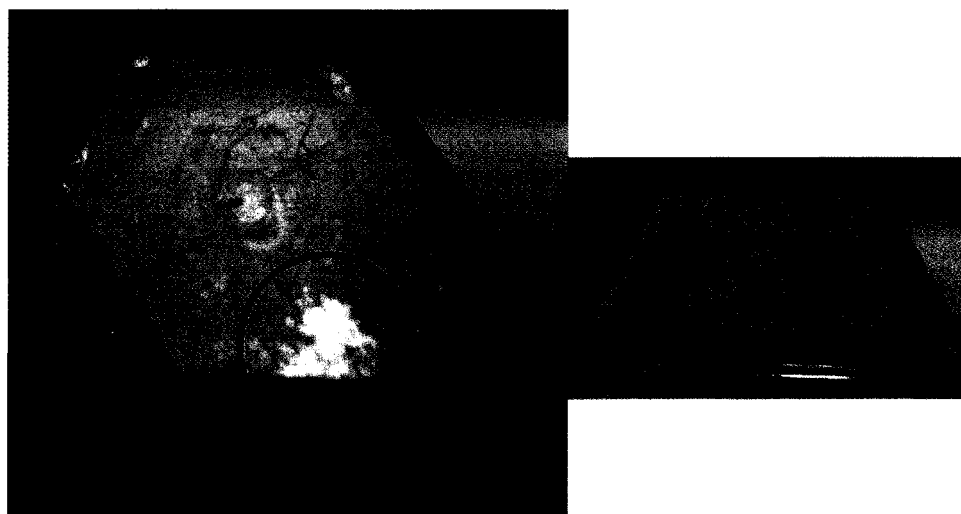


**Figure 2.20.** Laser damaged crystals illustrating strong scattering from internal cleavage plane separation (left) and topical burning (right).

The mechanism of decomposition for the material was not explored in great detail, however, the presence of the interference fringes surrounding the burn site suggests that considerable pressure was generated within the crystal, likely generated by the vaporization of water due to solution

inclusions; occasionally small amounts of liquid were observed on freshly cleaved surfaces.

While lasing, let alone up-conversion lasing, was not successfully demonstrated in the KAP/Rh110 system, the concept of an optically transparent non-centrosymmetric host doped with a variety of luminophores does remain viable. Crystal hosts enhance the photostability of included molecules. Non-centrosymmetric hosts provide a convenient means of generating high energy photons from readily available low energy sources. Inclusion of a variety of organic dyes provides a tunability not found in lasers limited to harmonics of the input radiation. However, crystal hosts possessing cleavage planes should in general not be considered for this type of application as the mechanical weakness of the cleavage plane will likely result in device failure. Gains in processability cannot accompany a sacrifice in host integrity.

#### 2.2.3.6 *Experimental*

**Crystal Growth:** The crystal growing solution was prepared by the addition of A.C.S. grade KAP (Aldrich) in deionized water (Barnsted

NANOpure, 18.2 M $\Omega$ /cm) that was subsequently covered, boiled, and finally filtered through a medium grade frit filter to remove any residual particulates. An appropriate amount of dye was then added to the solution (typically, [Rh110] =  $1.0 \times 10^{-4}$  M; 8.1 mg Rh110/0.5 L KAP solution) after the KAP solution equilibrated to room temperature. Rhodamine 110 chloride (Aldrich) was used without further purification.

Additional details including KAP solubility data, X-ray crystallography, and spectroscopy can be found in Section 2.2.2.6

**Second Harmonic Generation:** Two photon excitation provided by a Millennia pumped, Tsunami Ti:sapphire oscillator operating at 800 nm pulsed at 80 MHz and 120 fs was channeled into a homebuilt inverted microscope.<sup>53</sup> Up-conversion fluorescence was detected utilizing a single photon counting PMT (Hamamatsu HC135-01). The up-conversion luminescence spectrum was measured using a fiber-optically coupled Ocean Optics photospectrometer.

### 2.3 Methyl Red in Phthalic Acid

In 1900, Gaubert coined the term *syncrystallization*, a contraction of *synchronous crystallization*, that subsequently came to describe the rare occurrence of two seemingly disparate substances that crystallize at the same time such that oriented crystallites of one substance are overgrown by the other.<sup>54</sup> There are many examples of two or more things that crystallize at the same time<sup>55</sup> and *syncrystallization* is sometimes used literally.<sup>56</sup> The meaning that evolved from Gaubert's early work is restricted in the above sense. A classic example of a supposed syncrystal studied first by Gaubert, and later by Neuhaus, is that of phthalic acid (PA) containing oriented crystallites of the acid-base indicator, methyl red (MR, CI# 13025). We could not reckon the nature of these curious objects from reading the literature alone and therefore embarked upon an experimental history in order to achieve a contemporary understanding of one *syncrystal*, and the general process of syncrystallization.<sup>57</sup>

In 1996, Mitchell *et al.* reported the linear dichroism (LD) of some dyed PA crystals but gave no mention of MR.<sup>58</sup> Subsequently, we reported that adjacent PA growth sectors were colored yellow and red by MR, respectively.<sup>59</sup> In reviews, Kahr published a photograph of one such crystal,<sup>60</sup> and paintings of them by Vasquez.<sup>61</sup> As MR is a classic acid-base indicator, it was natural to assume that the red color was associated with the protonated  $\text{MRH}^+$  and the orange-yellow was from neutral  $\text{MR}^\circ$  (Figure 2.21). However, nothing about our PA/MR crystals resembled descriptions from the last century of crystallites of MR oriented within PA. Where was the so-called syncrystal, and what was it?

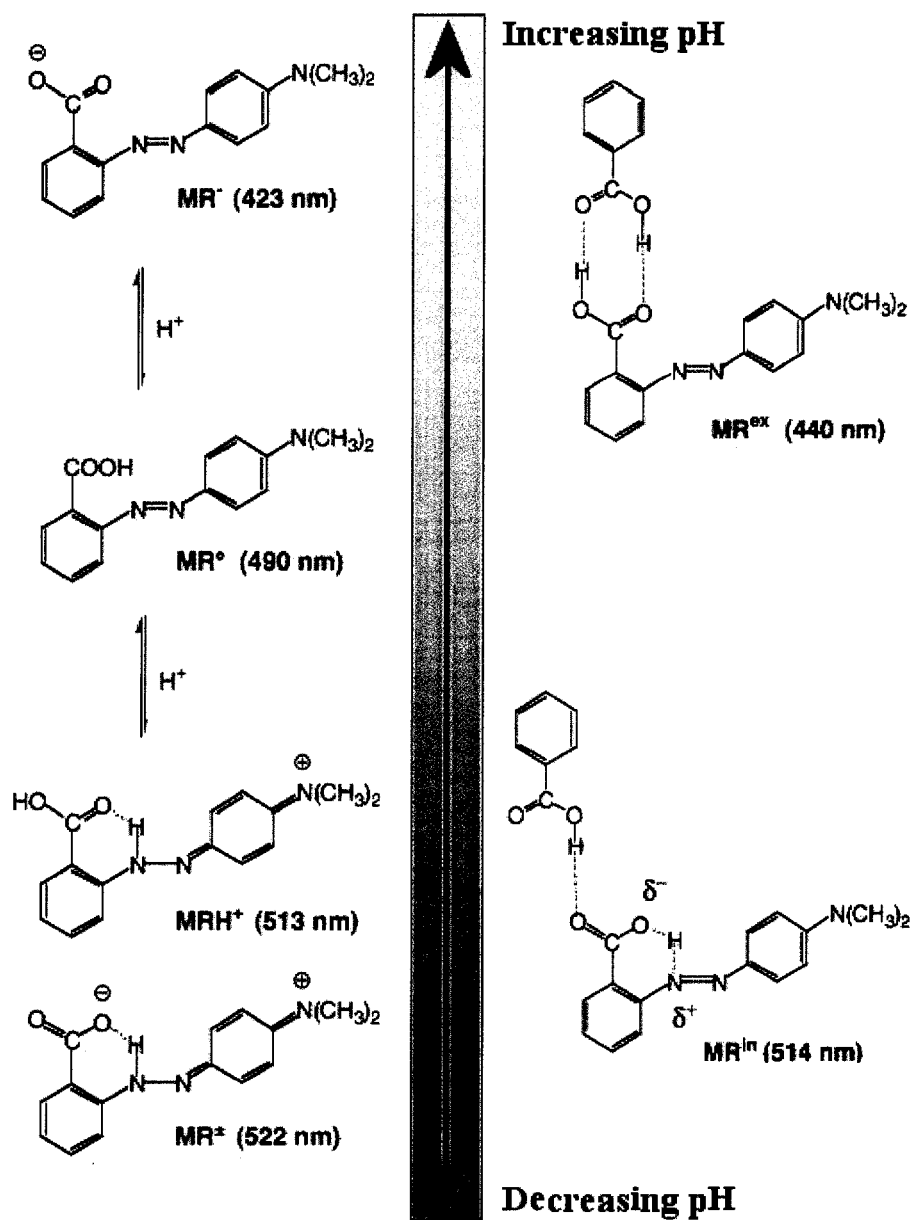


**Figure 2.21.** Left column: methyl reds identified in solution equilibria. Right column: proposed high and low energy absorbing H-bonding patterns with aromatic acids. Center bar: range of colors observed in mixed crystals of PA and MR. The data 423

(aq.), 513 (aq.), and 522 (aq.) nm are from ref. 77. The data 490 (EtOH), 440, and 514 nm are from this work.

### 2.3.1 *Syncrystallization*

Lehmann first discovered that PA crystals, grown in the presence of dye solutions, are often colored in particular growth sectors.<sup>62</sup> He did not use MR although he did report pleochroic crystals when PA was grown in the presence of related azo dyes, chrysoidin (CI# 11270) and methyl orange (CI# 13020). The crystallization of PA from dye solutions was further studied by Gaubert.<sup>63</sup> Initially, he introduced the term syncrystallization to describe isomorphous barium, lead, and strontium nitrates grown in the presence of methylene blue.<sup>54</sup> He concluded that microcrystals of the dye were oriented within heavily colored lead nitrate crystals, because deposition usually only occurred when the dye and salt were saturated in solution.

When Gaubert first studied dyed PA crystals, though not with MR, he was emphatic that these were not nitrate-like syncrystals<sup>63</sup> because PA was colored even when the dye was under-saturated in the growth solution. Nevertheless, Gaubert left open the possibility of using the term

syncrystallization for coloring transparent crystals with dilute dye solution.<sup>64</sup> A generation later, he reversed himself by restricting syncrystallization to those cases of colored crystals that could only be produced at great dye strength<sup>65</sup> prompting Buckley to characterize Gaubert's work as "intermittent and discursive".<sup>66</sup> Bunn argued that Gaubert's conclusion of crystals within crystals was given "without much evidence."<sup>67</sup>

In 1937, Gaubert returned to PA with MR.<sup>68</sup> He reported that these highly dichroic dyed crystals became more or less isotropic in their absorption for light incident along [010] when heated to temperatures of approximately 150°C. Gaubert assumed that dye molecules diffused through the PA lattice. Upon cooling these crystals, he observed the formation of oriented crystalline *bâtonnets*<sup>69</sup> within the bulk PA lattice and concluded that microcrystals of the dye were oriented within the host.

Gaubert's concept of syncrystallization predated X-ray diffraction. It gave way to epitaxy, the oriented overgrowth of one crystalline substance on another. Neuhaus, a pioneering epitaxy researcher,<sup>70</sup> brought his experience to studies of dye inclusion crystals and thereby carried some of Gaubert's results into the post-diffraction era. By measuring lattice constants of



crystalline dyes and the salts with which they had ostensibly syncrystallized, Neuhaus proposed epitaxial relationships. In hindsight, it appears to us that Neuhaus tried to force lattice matches upon host/guest pairs.<sup>71</sup> For example, in support of epitaxial growth, he indicated that four thirds of the (110) *d*-spacing in PA was approximately equal to the (110) spacing in MR, and that three halves the  $[\bar{1}10]$  vector in PA was equal to the  $[\bar{1}10]$  vector in MR. While this kind of lattice matching may well make sense in some cases, it is little more than numerology in others.

### 2.3.2 *Phthalic Acid*

Phthalic acid (PA) crystals have an unusually rich habit. The following forms have been observed: {010}, {001}, {110}, {111}, {021}, {112},  $\{11\bar{2}\}$ , {131},  $\{11\bar{1}\}$ .<sup>72</sup> Their relative importance is sensitive to solvent and additives. The {010} face is dominant when PA is crystallized from water but absent when crystallized from ethanol. Figure 2.22 illustrates the idealized habit of PA when grown from an evaporating 20% EtOH/H<sub>2</sub>O solution at room temperature.

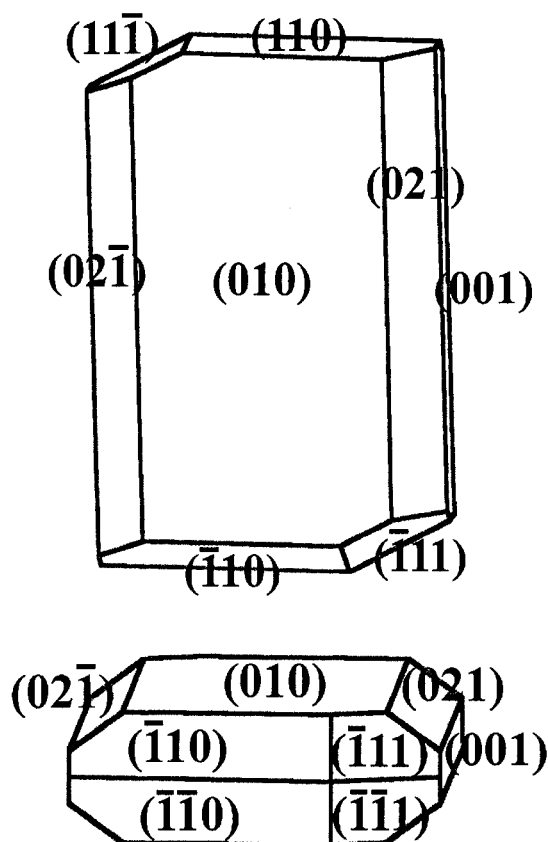


**Figure 2.22.** Idealized habit of PA grown by slow evaporation from a 20% ethanol/water solution

We began a collaboration with Prof. Andrew Rohl to calculate the structure of the PA surfaces and the ground state geometry of MR, information crucial to explain the selectivity of the various facets. The crystal structure of PA (space group  $C2/c$ , Table 2.2) was optimized with the GULP simulation engine<sup>73</sup> using the CVFF force field<sup>26</sup>. The Coulombic

interactions, evaluated using the Ewald sum, and the long range van der Waals terms described by a Lennard Jones potential, were truncated at 12 Å. This yielded a cell that was 2.1% smaller than the experimental cell listed in Table 2.2.\* The structures of all possible terminations of the 15 surfaces with the largest  $d_{hkl}$  were then generated using the GDIS program<sup>74</sup> and optimized in GULP.<sup>73</sup>

---

\* CVFF relaxed PA unit cell:  $a = 4.837$  Å,  $b = 14.382$  Å,  $c = 9.877$  Å,  $\beta = 95.701^\circ$

**Table 2.2.** Crystallographic data

Substance	MR	0.5PA · MR	2,5-DHB · MR	MR · HBr · H <sub>2</sub> O	PA <sup>75</sup>
Formula	C <sub>15</sub> H <sub>15</sub> N <sub>3</sub> O <sub>2</sub>	C <sub>19</sub> H <sub>18</sub> N <sub>3</sub> O <sub>4</sub>	C <sub>22</sub> H <sub>21</sub> N <sub>3</sub> O <sub>6</sub>	C <sub>15</sub> H <sub>18</sub> BrN <sub>3</sub> O <sub>3</sub>	C <sub>8</sub> H <sub>6</sub> O <sub>4</sub>
Mol. wt. (amu)	269.30	352.36	423.42	368.23	166.13
Space group	$P\bar{1}$	$C2/c$	$P2_1/c$	$P2_1/c$	$C2/c$
<i>a</i> (Å)	8.2370(5)	9.0830(5)	7.0220(3)	7.8900(2)	5.0698(4)
<i>b</i> (Å)	8.4990(6)	14.1850(7)	13.5530(7)	11.8980(4)	14.318(1)
<i>c</i> (Å)	11.211(1)	26.653(2)	21.840(1)	16.6620(7)	9.6305(5)
<i>a</i> (deg)	92.478(3)	90	90	90	90
<i>β</i> (deg)	110.281(3)	98.042(4)	99.984(2)	92.568(1)	93.260(4)
<i>γ</i> (deg)	113.705(3)	90	90	90	90
<i>V</i> <sub>cell</sub> (Å <sup>3</sup> )	658.66(9)	3400.3(4)	2047.0(2)	1562.58(9)	697.81(4)
Temp (K)	130 (2)	130 (2)	298	130 (2)	298
<i>Z</i>	2	8	4	4	4
<i>R</i> <sub>1</sub>	0.0635	0.0757	0.0625	0.0375	0.040
<i>wR</i> <sub>2</sub>	0.1615	0.2338	0.1530	0.0977	Not reported
GOF	0.990	1.012	0.925	0.999	Not reported
<i>e</i> <sub>min</sub> / <i>e</i> <sub>max</sub> ( <i>e</i> / Å <sup>3</sup> )	0.216 / - 0.269	0.373 / -0.393	0.288/-0.221	0.504 / -0.777	0.44/-0.22

The surface energy, the energies of surfaces compared to the bulk per unit surface area, and the attachment energy, the energy released when a new slice of depth  $d_{hkl}$  is attached to a crystal face, respectively, were calculated for the (*hkl*) faces with the largest inter-planar spacings. They are listed in Table 2.3. The most striking feature is that the values for the surface energies as well as for the attachment energies span small ranges. This is reflected in the calculated growth morphology (based on attachment

energies) and equilibrium morphology (based on surface energies), where five and nine forms are present, respectively. Such a preponderance of forms is rare but is consistent with the sensitivity of the morphology to growth conditions.<sup>72</sup>

**Table 2.3.** Computed phthalic acid surface and attachment energies for various facets for the relaxed phthalic acid unit cell.

Face	$d_{hkl}$ (Å)	Surface energy (J m <sup>-2</sup> )	Attachment energy (eV/mol)
(020)	7.172	0.324	-1.055
(021)	5.783	0.267	-1.032
(002)	4.889	0.258	-1.157
(110)	4.594	0.249	-1.141
(111)	4.310	0.329	-1.328
(022)	4.039	0.291	-1.316
(11 $\bar{1}$ )	4.021	0.204	-1.031
(11 $\bar{2}$ )	3.509	0.355	-1.775
(130)	3.405	0.308	-1.653
(041)	3.367	0.305	-1.350
(13 $\bar{1}$ )	3.284	0.313	-1.557
(112)	3.207	0.228	-1.461
(131)	3.151	0.293	-1.800
(023)	2.967	0.293	-1.328
(13 $\bar{2}$ )	2.885	0.340	-1.701

### 2.3.3 Methyl Red

Methyl red (MR) has complex acid-base equilibria.<sup>76</sup> Four different forms have been proposed in various solutions: neutral ( $\text{MR}^0$ ), zwitterionic ( $\text{MR}^\pm$ ), protonated ( $\text{MRH}^+$ ), and deprotonated ( $\text{MR}^-$ )<sup>77</sup> (Figure 2.21) supposedly corresponding to absorption maxima at 490 (EtOH), 522 (aq.), 513 (aq.), and 423 (aq.) nm, respectively. When used as a pH indicator, the red color of MR is generally ascribed to  $\text{MRH}^+$  although a comparable absorption at 522 nm has been assigned to the red  $\text{MR}^\pm$  in mildly acidic ( $3 < \text{pH} < 6$ ) solutions. Despite the barely distinguishable red colors of  $\text{MR}^\pm$  and  $\text{MRH}^+$ , the isosbestic point observed by titration indicates the presence of two species at low pH. The  $\text{pK}_a$  of  $\text{MRH}^+$  is  $2.1 \pm 0.1$  in water.<sup>77</sup> The predominant species in the solution from which we grow mixed crystals was the zwitterion,  $\text{MR}^\pm$  ( $\lambda_{\text{max}} = 522 \text{ nm}$ ).

To further verify that the species in *slightly* acidic, aqueous solutions is not  $\text{MRH}^+$ , we analyzed the  $^1\text{H}$ -NMR spectrum of MR in three  $\text{CD}_3\text{OD}$  solutions: (1)  $5.9 \times 10^{-3} \text{ M}$  MR; (2) the same, saturated with PA (0.12 M,  $\text{pK}_{a1} = 2.95$ )<sup>78</sup>; (3) the same as (1) with HCl (0.12 M). In (2), the resulting spectrum was essentially the superposition of the  $^1\text{H}$ -NMR spectra of PA

and MR. In (3), the addition of HCl produces a sharp downfield shift of the aromatic region, consistent with protonation.\*

We obtained a high-resolution crystal structure of MR. The published structure<sup>79</sup> was based only on the refinement of the heavy atom positions ( $R = 0.093$ ); hydrogen atoms were ill-defined. After locating and anisotropically refining heavy atoms, a difference map revealed the positions of all hydrogens, the placement of which are pivotal in understanding PA/MR mixed crystals. (Throughout, the symbol PA/MR indicates non-stoichiometric mixed crystals, whereas PA·MR would indicate a 1:1 co-crystal.) The MR<sup>o</sup> carboxylic acid proton was located on the oxygen nearest an azo nitrogen, and intramolecularly hydrogen bonded to it ( $N-O = 2.591(2) \text{ \AA}$ ). The molecules pack as head-to-tail dimers. MR has a distinctly quinoidal geometry in the crystalline state; the aromatic bond length variation in the dimethylaminophenyl group is  $0.050 \text{ \AA}$ . Summaries of crystallographic data are given in Table 2.2.

To probe the relative stabilities of the neutral species compared to the zwitterion, Andrew Rohl undertook first principles calculations. The work

---

\* A comparison of the six most downfield peaks in spectra were the following for MR (MR in 0.12 M PA) [MR in 0.12 M HCl]:  $\delta = 7.974 \text{ ppm}$  (7.983) [8.069]; 7.948 (7.959) [8.040]; 7.786 (7.788) [7.997]; 7.760 (7.762) [7.969]; 7.686 (7.667) [7.787]; 7.655 (7.635) [7.755].

of Tuble and coworkers on norleucine demonstrates that its zwitterion is unstable *in vacuo* and requires the presence of a solvent for stabilization.<sup>80</sup> To see if the same is true for the larger MR molecule potential energy was computed as a function of the N to H distance between 0.95 and 2.0 Å in 0.05 Å increments. The Gaussian 03 program was employed.<sup>81</sup> The 6-31G\* basis set was used with the Hartree-Fock, B3LYP and MP2 methodologies. The calculations were performed both *in vacuo* and under aqueous conditions using the continuum IEFPCM solvation model. The results of these calculations are summarized in Figure 2.23.

All three methodologies predict that the zwitterion is not stable *in vacuo*, although all three curves show a change in slope at about 1.05 Å. Adding solvation via the continuum IEFPCM model results in a double well potential in each case. The zwitterion minimum is shallow, particularly in the MP2 curve. The B3LYP curves are very similar to the MP2 curves; these are quite different than the HF curves. All subsequent first principles calculations have used the B3LYP hybrid functional with the larger 6-311G\*\* basis set as they are much quicker than the MP2 calculations but offer similar accuracy. MR° is calculated to be 37 kJ/mol lower in energy than MR±, with N-H distances of 1.75 and 1.05 Å respectively.



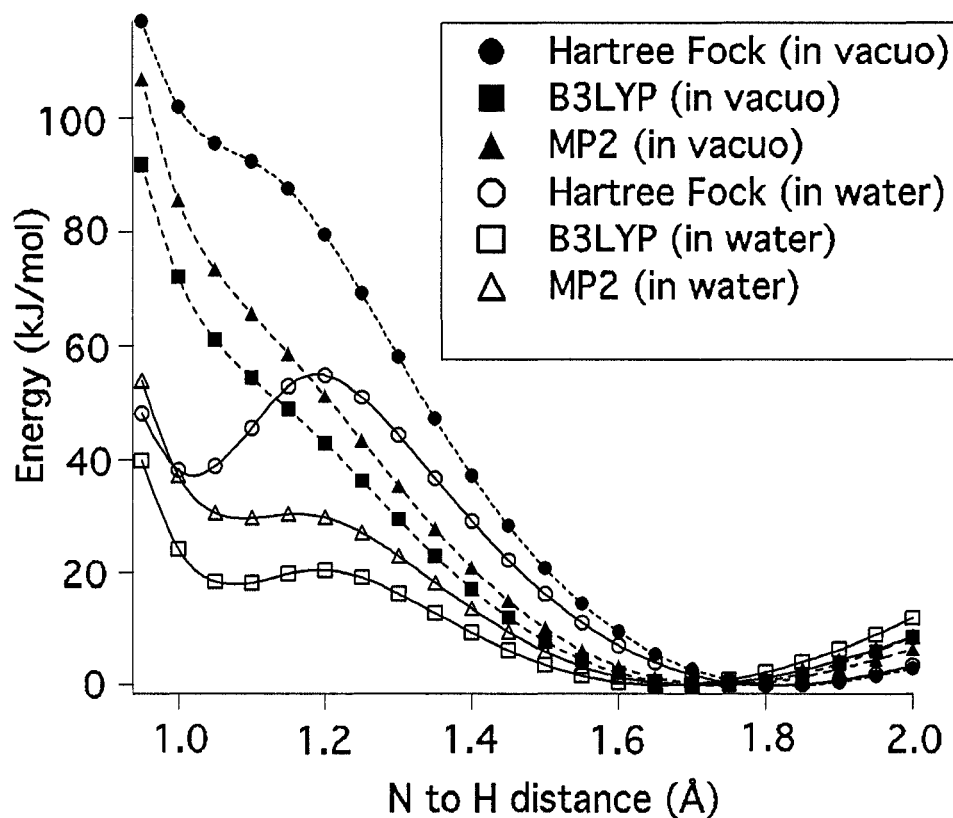


**Figure 2.23.** Computed energies MR molecule as a function of the N to H distance using various first principles methods. The dashed lines are *in vacuo* calculations and the solid lines are the results in water using the continuum IEFPCM model (see text).

MR<sup>o</sup> in the crystal structure was also slightly quinoidal; the aromatic bond length variation in the dimethylamino group was 0.46 Å. The calculated gas phase anti-parallel dimer, was only slightly more quinoidal (aromatic bond length variation = 0.53 Å). In other words, the

centrosymmetric arrangement of MR<sup>o</sup>s induces only a modest distortion of the individuals.

#### 2.3.4 Co-Crystals of Methyl Red and Phthalic Acid

Attempts to grow PA/MR mixed crystals at high dye concentrations, at or above  $3 \times 10^{-4}$  M MR, precipitated 0.5:1 co-crystals of PA and MR (0.5PA·MR).<sup>\*</sup> Crystallographic parameters are given in Table 2.2. Again, electron density difference maps revealed all protons. The MR molecule in the co-crystal structure was not protonated MRH<sup>+</sup>, nor the NH<sup>+</sup> zwitterionic tautomer MR<sup>±</sup>. Nevertheless, MR in the 0.5PA·MR co-crystal was slightly quinoidal (Figure 2.24), with an aromatic bond length variation in the dimethylaminophenyl ring of 0.057 Å, matching surprisingly well the geometry of the calculated MR<sup>o</sup> monomers or dimers. Similarly, the co-crystals had an intramolecular H-bond to the nearest azo nitrogen atom (N-O = 2.549(4) Å). There is a single H-bond to a neighboring PA donor that sits on a special position, the diad axis, giving rise then to the 1:2

---

<sup>\*</sup> Thin red plates were collected. The crystals first deposited and those from the recrystallization had the same unit cell.

stoichiometry. Pairs of MRs in 0.5PA·MR are anti-parallel and virtually superimposable on the dimers in the pure MR crystal structure.

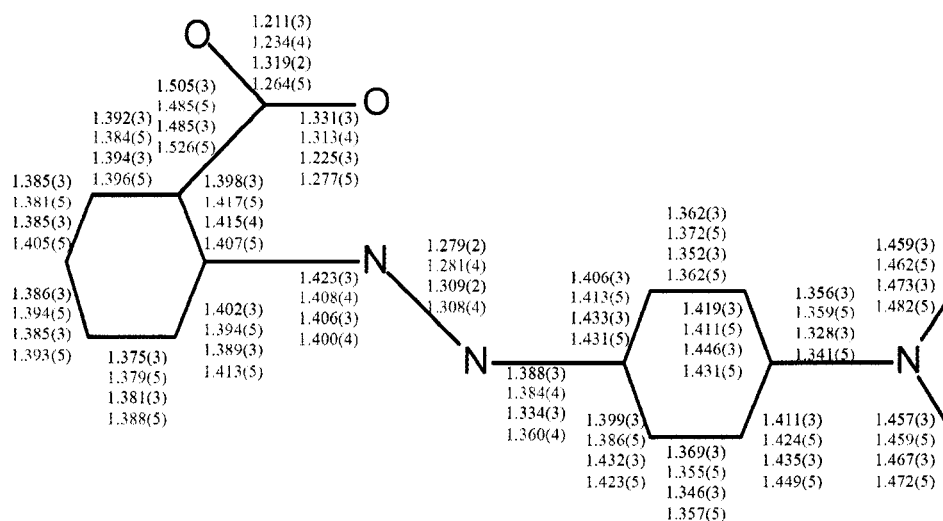


**Figure 2.24.** MR skeleton with crystallographic bond lengths of pure MR crystal (black), 0.5PA·MR (red), MR·HBr·H<sub>2</sub>O (blue), and 2,5-DHB·MR (green).

Given that O-protonated MR<sup>o</sup> was observed in both the MR and 0.5PA·MR we aspired to establish structures of the purported red species MRH<sup>+</sup> and MR<sup>±</sup> as models of the species contained within PA mixed crystals (see next section). MR·HBr·H<sub>2</sub>O crystals were prepared from aqueous solutions to which HBr had been added drop wise. A proton was unambiguously located on an azo nitrogen atom nearest the COOH group.

The ion is quinoidal. The aromatic bond length variation in the dimethylaminophenyl group is 0.104 Å with  $\pi$  electrons considerably more localized than in MR°.

Whither the zwitterion, MR<sup>±</sup>? We ultimately observed it while analyzing co-crystals of methyl red with another aromatic acid, 2,5-dihydroxybenzoic acid (2,5-DHB), deposited from ethanol solutions. Figure 2.25 shows the hydrogen bonding contacts that MR makes with two 2,5-DHB molecules. Because two acid molecules serve as H-bond donors to the MR carboxylic acid group, the latter's proton is passed to the azo-nitrogen atom. The quinoidal character of MR<sup>±</sup>, as judged from the dimethylaminobenzene aromatic bond length variation (0.69 Å), was intermediate between that of MR° and MRH<sup>+</sup>. However, molecules are pair-wise anti-parallel in precisely the manner as observed for MR° in MR and 0.5PA·MR crystal structures.

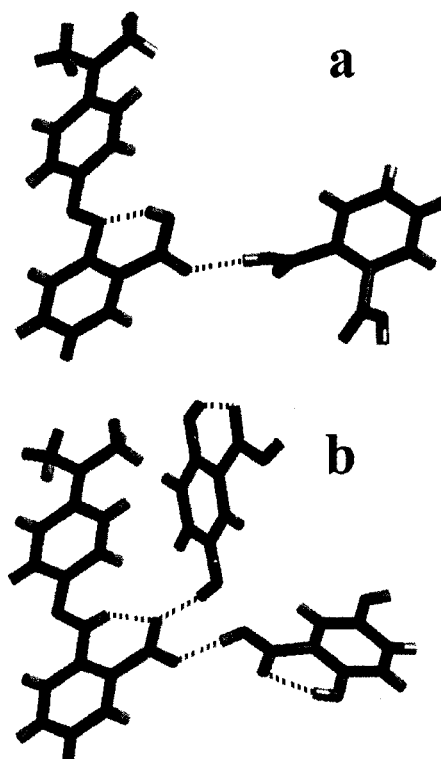


**Figure 2.25.** Hydrogen bonds of methyl red with (a) phthalic acid and with (b) 2,5-DHB, in respective co-crystals.

It was hoped that features in the absorption spectra of the MR co-crystals could be correlated to the x-ray determined MR geometries in the various crystalline environments. The spectra were obtained by smearing various co-crystals of MR between glass slides in order to produce fragments thin enough to transmit light (Figure 2.26). The  $\lambda_{\text{max}}$  for crystalline MR, 0.5PA·MR, 2,5-DHB·MR $\pm$ , and MR·HBr·H<sub>2</sub>O were 510 nm, 509 nm, 476 nm, and

518 nm (with a pronounced shoulder at 610 nm), respectively. This data is curious in that the spectra of MR and 0.5PA·MR are identical, despite the H-bonding in the latter case of MR to PA, and are unusually red. The latter shift could be a consequence of charge transfer interactions. Also, of note is that comparative blue shift of 2,5-DHB·MR. This could be a consequence of a hypsochromic shift due to close anti-parallel dipoles. We acknowledge that these spectra were made under non-ideal conditions (crushed crystals) with directions unspecified. Furthermore, collective interactions as yet undetermined could dominate the spectra of single dye crystals.<sup>82</sup>

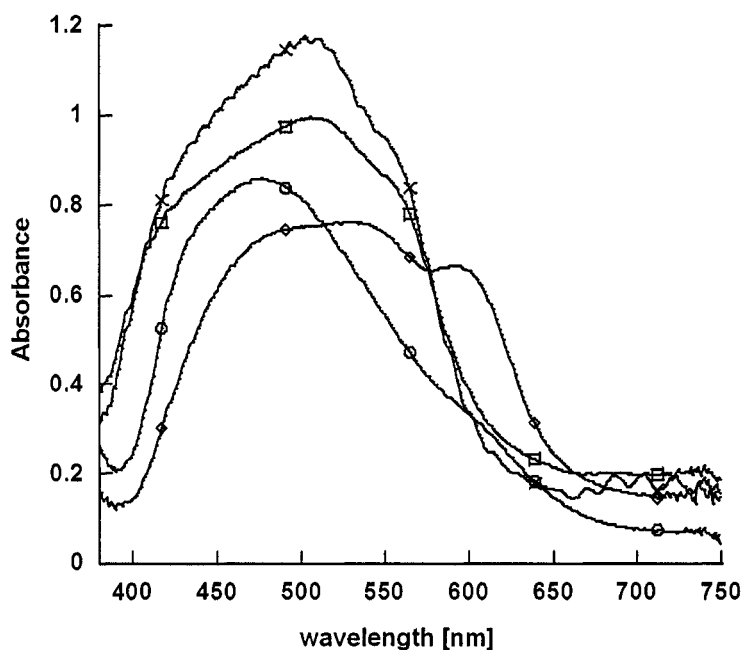


**Figure 2.26.** Crushed powder absorption spectra of crystals of pure MR ( $\times$ ), 0.5PA·MR ( $\square$ ), 2,5-DHB·MR ( $\circ$ ), MR·HBr·H<sub>2</sub>O ( $\diamond$ ).

### 2.3.5 Mixed Crystals of Methyl Red and Phthalic Acid

Mixed crystals of PA and MR (PA/MR) were easily grown on microscope slides (Figure 2.27).<sup>\*</sup> We observed {010} plates with {021}, {110}, and {001}

---

<sup>\*</sup> Larger crystals can be obtained by slow evaporation of a 20% EtOH/H<sub>2</sub>O solution (0.75 g PA/ mL) at room temperature, however, care must be taken to retrieve the crystals approximately 6-8 hours after nucleation to ensure crystals are grown with a nearly constant solvent composition. Typical MR concentration was  $5 \times 10^{-5}$  M. Absorbance measurements of dissolved mixed crystals grown from  $1.8 \times 10^{-3}$  mass % starting solution were found to contain  $3.3 \times 10^{-3}$  mass %.

facets. The crystals deposited were stunning in their dual color. They contained a red hourglass pattern associated with the {001} growth sectors as well as a yellow-orange tinge throughout as a result of dye adsorption by (010) and (110). Larger crystals ( $\sim 2 \text{ mm}^3$ ) were obtained by slow evaporation. The dye content, determined by measuring the absorbance of dissolved mixed crystals, was typically  $3.3 \times 10^{-3}$  weight percent when precipitated from solutions containing  $1.8 \times 10^{-3}$  weight percent ( $\epsilon_{\text{MR (EtOH, 490 nm)}} = 3.08 \times 10^3 \text{ M}^{-1} \text{ cm}^{-1}$ ). PA crystals concentrate MR and clean solutions of it. The segregation coefficient is 1.8.



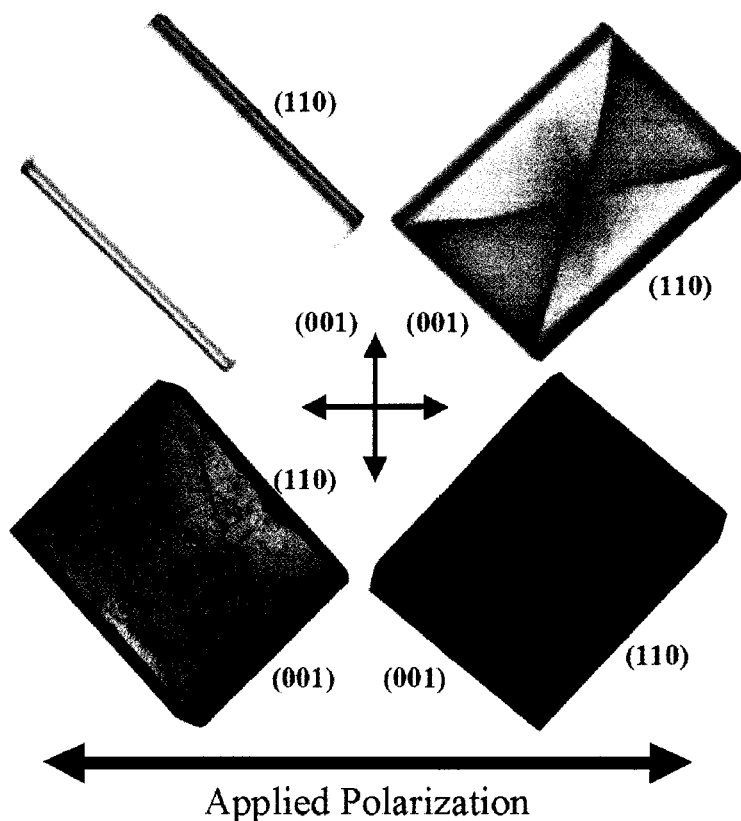


**Figure 2.27.** Pair of phthalic acid crystals grown in the presence of methyl red each in two positions with respect to applied plane polarized light. Crystals grown from solutions containing  $5 \times 10^{-5}$  M MR. Top: Crystal grown on a glass slide ( $0.8 \text{ mm} \times 0.45 \text{ mm}$ ). Bottom: Crystal grown in crystallizing dish by slow evaporation ( $5 \text{ mm} \times 7 \text{ mm}$ ). Crossed arrows represent crystallographic vibration directions.

Crystals were grown on slides over a range of MR concentrations ( $5 \times 10^{-4}$  to  $1 \times 10^{-5}$  M MR), albeit a small range in which dye could be detected and mixed crystal growth proceeded. There was no evidence of a concentration

dependence of the two species in the spectra. Aggregation therefore does not seem to play a large part in mixed crystal phenomenology.

#### 2.3.5.1 *Optical Properties of Methyl Red in Phthalic Acid*

The crystals are strongly dichroic for polarized light incident upon (010) with maximum absorbances for both the yellow and red species when the input polarization was aligned at  $42^\circ$  to the crystallographic  $a$  axis, or along  $[20\bar{1}]$ . The vibration directions are then very nearly the  $[201]$  and  $[20\bar{1}]$  directions.\* Larger crystals grown by slow evaporation were cleaved along (101) in slices approximately 0.5 mm thick allowing dichroic ratios to be measured for light polarized along  $[010]$  and  $[10\bar{1}]$  (Figure 2.28). The polarized absorption spectra of the various growth sectors are illustrated in Figure 2.29.

---

\* These directions, with an angle of  $87^\circ$  between them, are not strictly the vibration directions but they provide a convenient reference. As (010) is highly birefringent ( $n_{[20\bar{1}]} = 1.696$ ,  $n_{[201]} = 1.456$ ), a Lorentz approximation,  $A_{\text{obs}} = [(n^2+2)^2/9n] \times A_{\text{corr}}$ , was applied where  $n$  and  $A$  are the refractive index and absorbance in similar directions.

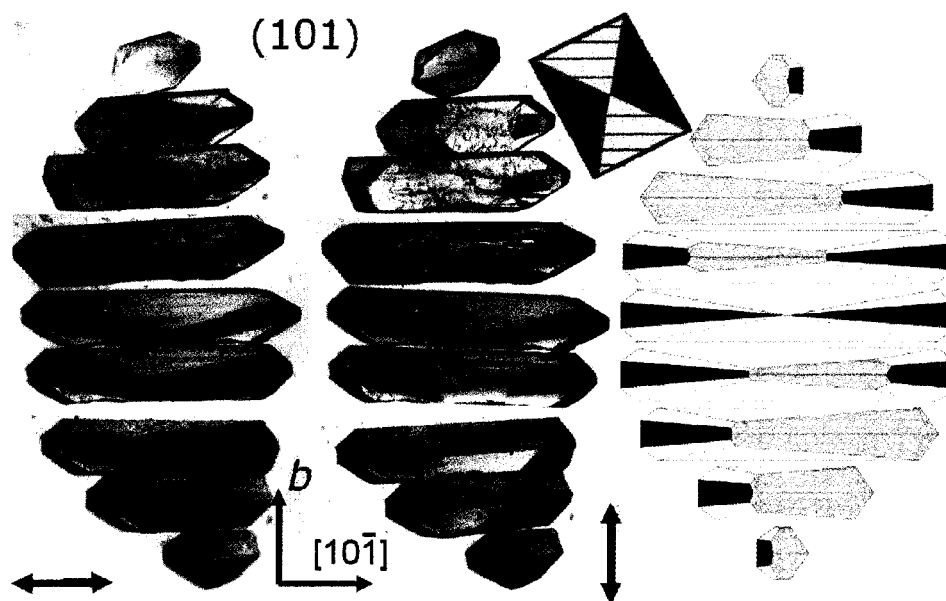


**Figure 2.28.** Contrast enhanced photographs of (101) slices of a MR dyed PA crystal viewed normal to the cleavage plane. Applied polarization indicated with red arrows. Right column illustrates idealized (101) slices of a {010} plate laid side by side. Inset shows {010} sliced to give rightmost composite illustration made with WinXMorph (Kaminsky, W. J. *Appl. Crystallogr.* **2005**, 38, 566-567).

The observed visible absorption bands of MR originate from  $\pi$ - $\pi^*$  electronic transitions. MR exists within PA crystals in at least two states, on the basis of energy, one absorbing in the green (513 nm) part of the visible spectrum that appears red, and the other in the blue (440 nm) part of the spectrum, appearing yellow (Figure 2.29).<sup>83</sup> The absorption of the yellow species is closest in energy to MR<sup>-</sup>. However, existence of MR<sup>-</sup> in the acid

crystals is unlikely. The hypsochromic shift is more likely the consequence of the MR carboxylic acid proton participating in a strong 'external' intermolecular H-bond with a phthalic acid acceptor, MR bound as an  $R_2^2(8)$  dimer ( $MR^{ex}$ ), Figure 2.21.<sup>84</sup>

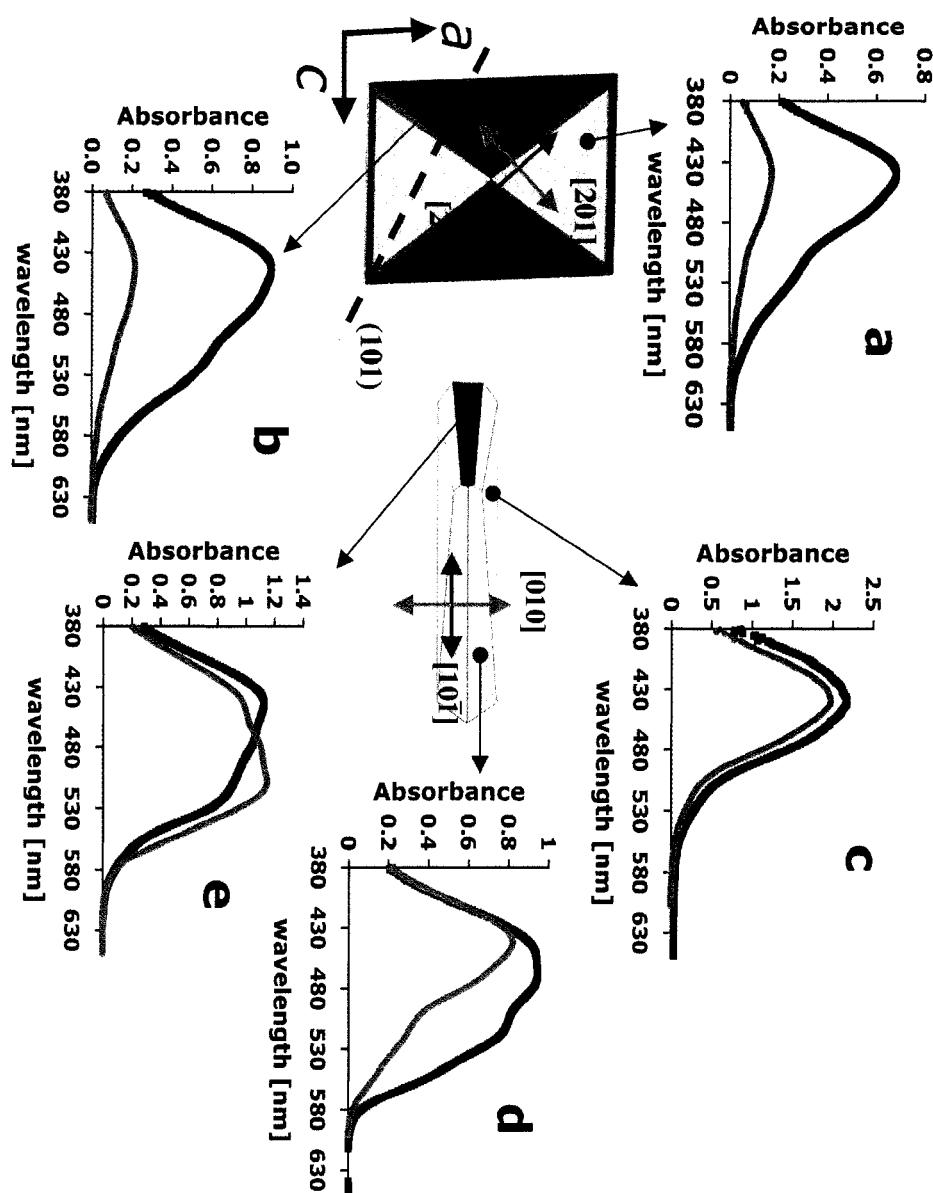


**Figure 2.29.** Polarized absorbance spectra of the various PA growth sectors dyed by MR. Vibration directions indicated are approximate. Input polarization direction: a, b:  $[20\bar{1}]$  (black),  $[201]$  (grey); c, d, e:  $[10\bar{1}]$  (black),  $[010]$  (grey).

In their electronic structures,  $\text{MR}^{\text{ex}}$  and  $\text{MR}^-$  should resemble one another. In order to test this notion we carried out ZINDO calculations of the electronic transitions of the various MR species conjectured. To model the  $\text{MR}^{\text{ex}}$  species, a MR H-bound to benzoic acid forming an  $\text{R}_2^2(8)$  dimer was constructed.\* The energies of the transitions with the greatest oscillator strengths for  $\text{MR}^-$ ,  $\text{MR}^{\text{ex}}$ ,  $\text{MR}^{\circ}$ ,  $\text{MR}^{\pm}$ , and  $\text{MRH}^+$  were 309, 359, 386, 491, and 467 nm, respectively.<sup>85</sup> The transition for  $\text{MR}^{\text{ex}}$  is intermediate in energy when compared to  $\text{MR}^-$  and  $\text{MR}^{\circ}$ , precisely what is observed experimentally. The virtually parallel electric dipole transition moments were used as the molecular axes for all orientation measurements (Figure 2.30).

---

\* The benzoic acid and MR dimer was constructed in Gaussian 03 using the hybrid B3LYP functional and the 6-311G\*\* basis set. The continuum IEFPCM solvation model was used with the water solvent parameters. The united atom model was used to construct the cavity, except for the two carboxylate groups where explicit H atoms were used.



**Figure 2.30.** EDTMs of the strongest transitions overlaid on MR structure for (top, clockwise)  $\text{MR}^-$ ,  $\text{MR}^\circ$ ,  $\text{MR}^{\text{ex}}$ ,  $\text{MR}^\pm$ ,  $\text{MRH}^+$ . EDTM vectors for the latter four MR species are nearly identical.

On the basis of studies of the protonation of MR in solution and in co-crystals, we have concluded that the red species is unlikely to be  $\text{MRH}^+$  as we had earlier conjectured.<sup>60</sup> The absorbance of the red species is intermediate with respect to  $\text{MR}^\circ$  and  $\text{MR}^\pm$ , presumably a consequence of the 'internal' location of the COOH proton residing in between the oxygen and nearest azo nitrogen. We hereafter call this species  $\text{MR}^{\text{in}}$ .

The yellow species ( $\text{MR}^{\text{ex}}$ , 440 nm) was observed in {010}, {001}, and {110} growth sectors whereas the red species ( $\text{MR}^{\text{in}}$ , 514 nm) was observed only in {001} and {110}. The deconvolution of the absorbance spectra in sectors containing both species was achieved by subtracting the spectrum of the pure yellow species found exclusively in {010} multiplied by a variable scaling factor (Figure 2.31). The difference spectra had the same  $\lambda_{\text{max}}$  for all polarizations and growth conditions.



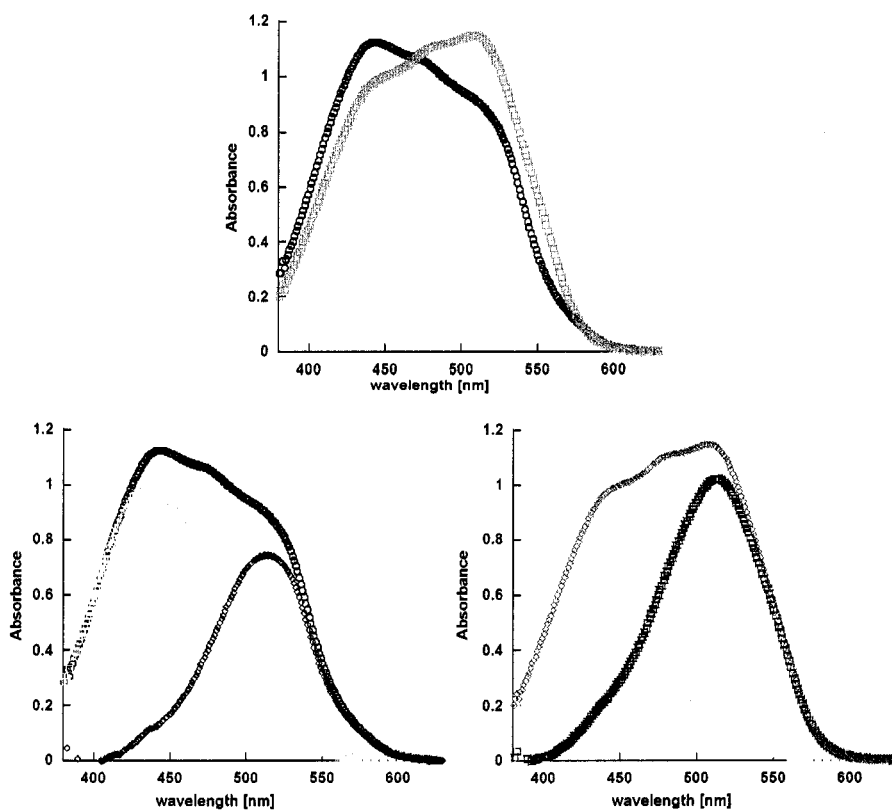


**Figure 2.31.** Example of spectral deconvolution required for linear dichroism measurements. (upper) Polarized absorption spectra of [001] measured normal to (101) using input polarization  $[10\bar{1}]$  (black) and  $[010]$  (grey). (lower left) Deconvolution of  $[10\bar{1}]$  by subtracting the spectra of  $MR^{ex}$  found in (010) multiplied by a scaling factor (left, yellow) resulting in spectra for  $MR^{ex}$  (right, red). (lower right) deconvolution of  $[010]$  using the same technique.

The orientations of the four symmetry related electric dipole transition moments for  $MR^{in}$  and  $MR^{ex}$  were calculated from the dichroic ratios (Figure 2.29).<sup>\*</sup> The angle with respect to the vibration directions in which it is measured is equal the inverse tangent of the dichroic ratio to the  $-1/2$  power. The orientation of the yellow species in {001}, {010}, and {110} is relatively invariant being  $49^\circ$ ,  $46^\circ$ , and  $44^\circ$  from [010] in the (101) plane, respectively. The orientation of the red species in the {001} and {110} growth sectors was  $40^\circ$  and  $62^\circ$  from [010], respectively.

Mo  $K\alpha$  radiation from a sealed tube was indistinguishably diffracted from mixed PA/MR crystals and pure PA. It has been observed previously by us and others, that X-ray scattering experiments are ill suited to the analysis of dye inclusion crystals.<sup>60,67,86</sup>

#### 2.3.5.2 Docking Simulations

Docking simulations of MR to the lowest energy surfaces of (001) and (110) were conducted using a molecular replacement approach. Comparable docking to (010) was not possible as neither H-bond donors

---

<sup>\*</sup> Measurement of the dichroic ratio ( $A_{\perp}/A_{\parallel}$ ) along vibration directions in a plane enables the calculation of the orientation of the electric dipole transition moments within the plane. A three dimensional orientation of the electric dipole transition moments within the crystal lattice can be calculated from dichroic ratios obtained in two orthogonal planes. The small size of {021} prevented accurate absorbance measurements in this growth sector.

nor acceptors are exposed; removal of multiple PAs would be necessary. Single PA molecules were removed from the 2-D periodic surfaces of the relaxed cell and replaced with MR allowing for hydrogen bonding between COOH groups. Cerius2 was used to perform a constrained geometry optimization using the CVFF force field (Figure 2.32).<sup>26,87</sup> The PA atomic positions were fixed and the energy of MR was minimized as a function of position with its geometry fixed. The (001) surface has a single PA molecule presentation. The (110) surface displays two PA molecules related by symmetry in the bulk but dissymmetric on the surface. These two sites are distinguished as I and II (Figure 2.32). The long axis of MR is inclined  $40^\circ$  with respect to [010], parallel to PA hydrogen bonds, when docked to (001) and position I on (110). When docked to position II on (110), MR is nearly parallel to [100].

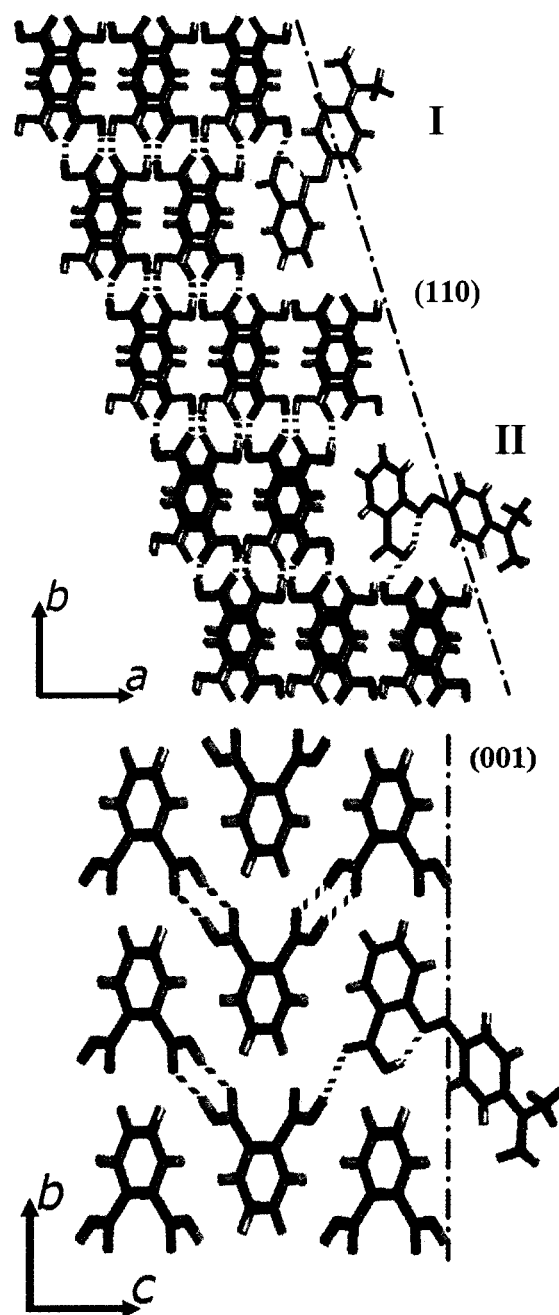


**Figure 2.32.** Simulations of MR<sup>in</sup> docking to two distinct sites (I) and (II) on (110) (upper) and one site on (001) (lower). Black dashed

lines denote lowest energy stable surfaces for the indicated facets.

#### 2.3.5.3 *Inclusion Modeling*

Computational modeling of MR<sup>in</sup> within the PA lattice was carried out to determine the lowest energy orientations for MR (Figure 2.33). The volume of two PA molecules, calculated from the crystal structure, is 349 Å<sup>3</sup>. Likewise, the volume of one MR is 329 Å<sup>3</sup>. Thus, we must remove at least two PA molecules from the lattice to accommodate one MR molecule. Assuming that MR is oriented approximately along  $[10\bar{1}]$  when viewed down  $[010]$ , consistent with the LD, three distinct substitutions of one MR for two PA molecules in the CVFF minimized lattice were considered: the long axis of MR parallel to  $[001]$ , parallel to  $[010]$ , and parallel to a hydrogen-bound PA dimer. MR<sup>ex</sup> parallel to a hydrogen-bound PA dimer, the only orientation possible to maintain proper hydrogen bonding geometry, was also analyzed. The MR geometry from the crystal structure was used to model MR<sup>in</sup>. The MR geometry from the calculated R<sub>2</sub><sup>2</sup>(8) benzoic acid complex was used to model MR<sup>ex</sup>.

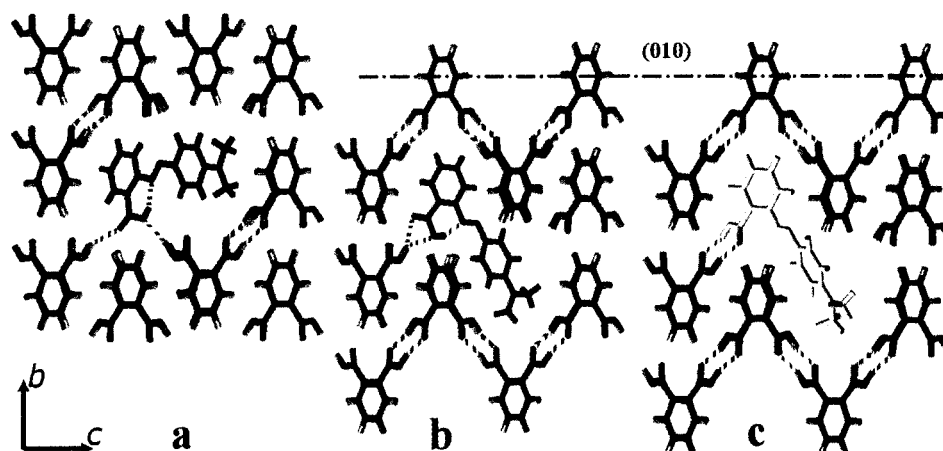


**Figure 2.33.** Models of  $\text{MR}^{\text{in}}$  (red) and  $\text{MR}^{\text{ex}}$  (yellow) within the PA lattice.  $\{110\}$  contains A, B, and C;  $\{001\}$  contains B and C;  $(010)$  contains only C. Lowest energy  $(010)$  surface denoted by dashed black line.

Initially, energies were minimized with MR restrained as a rigid body within a fixed PA lattice. The restraints on the PA lattice were then removed and the energy was again minimized. The replacement energies ( $RE$ s) were calculated as

$$RE = E_{\text{mc}} + n(E_{\text{PA}}) - (E_{\text{pc}}) + n(E_{\text{MR}})$$

where  $E_{\text{(mc)}}$  is the total minimized energy of the mixed crystal,  $n(E_{\text{PA}})$  is the energy of  $n$  isolated phthalic acid molecules removed to accommodate the host, and  $E_{\text{pc}}$  is the energy of the pure PA crystal, and  $n(E_{\text{MR}})$  is the energy

of  $n$  isolated MR molecules ultimately accommodated in the mixed crystal.

Energies for various models are tabulated in Table 2.4.

**Table 2.4.** Computed replacement energies (RE) for mixed crystal models

Model	Guest orientation	RE (kcal/mol)
Fig. 10a	MR <sup>in</sup> parallel to [001]	76.9
not shown	MR <sup>in</sup> parallel to [010]	82.4
Fig. 10b	MR <sup>in</sup> parallel to PA H-bonds	74.2
Fig. 10c	MR <sup>ex</sup> as R <sub>2</sub> <sup>2</sup> (8) dimer	72.3

#### 2.3.5.4 Heating Experiments

Gaubert refined the concept of syncrystallization while heating heavily dyed PA/MR mixed crystals. We repeated his experiment in crystals with a PA/MR mol ratio of  $5 \times 10^{-5}$ . At 150°C, the LD at 513 decreases and transmittance increases throughout the crystal.<sup>88</sup> We imaged the linear dichroism at 547 nm using the rotating polarizer technique (Figure 2.34).<sup>88</sup>

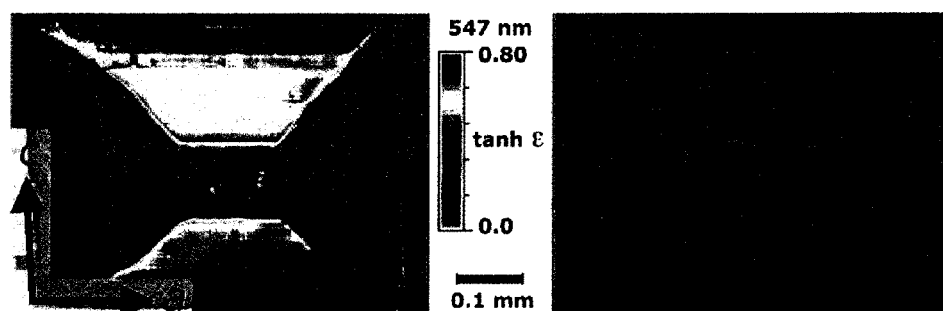


**Figure 2.34.** Linear dichroism images of a PA/MR crystal grown on a glass slide before heating (left) and after heating (right) at 150 °C for two hours. For a discussion of  $\tanh \epsilon$  see experimental.

After heating for 10 - 15 min, dark spots called bâtonnets by Gaubert, began to accumulate in the crystal (Figure 2.35). They grew lozenge-like with time along the cleavage planes. They advanced in the (010) planes perpendicular to the direction of elongation. Once the choice between symmetry related perpendicular directions in the centrosymmetric crystals was established, the bâtonnets never change direction. As they grew while traversing the crystal, they left behind red-dye depleted wakes (Figure 2.35). The birefringence of the depleted areas was unperturbed suggesting the bulk PA lattice reassembled in the wakes of the bâtonnets. The wakes remained orange and linearly dichroic, indicating that the diffusing species was  $\text{MR}^{\text{in}}$ . Analysis of the bâtonnets by micro-Raman spectroscopy



indicated that they were rich in methyl red but we could not unequivocally distinguish them as MR or as 0.5PA·MR due to signal from the sea of host PA.

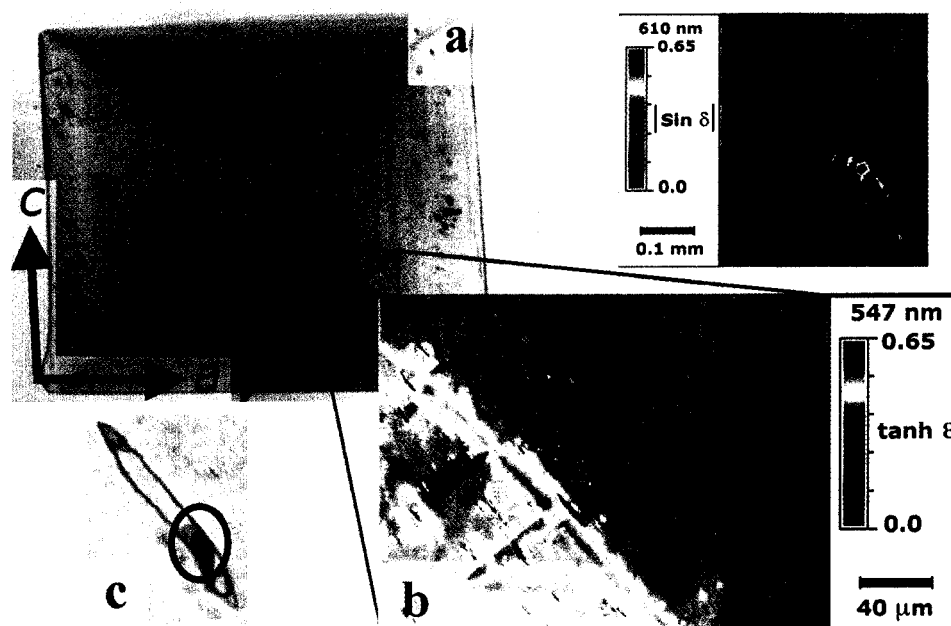


**Figure 2.35.** (a) PA/MR mixed crystal heated at 150 °C for 15 min and cooled to room temperature showing the appearance of dark bâtonnets. (b) Linear dichroism image showing migration of bâtonnets. (c) photograph of a bâtonnet after cooling and (d) the corresponding linear birefringence image showing the high birefringence, circled in red, of the syncrystal.  $\delta = 2\pi\Delta nL/\lambda$

### 2.3.6 Discussion

#### 2.3.6.1 Color

Our first task, when confronted with Gaubert's crystals, was to explain etiology of the different colors. The preponderance of evidence developed from mixed and co-crystals led to the conclusion that the difference between the yellow and red colors depended merely on whether the COOH proton was intramolecularly ( $\text{MR}^{\text{in}}$ ) or intermolecularly ( $\text{MR}^{\text{ex}}$ ) hydrogen bound. According to our ZINDO calculations,  $\text{MR}^{\text{ex}}$  is most like the basic  $\text{MR}^-$  species.  $\text{MR}^{\text{in}}$  is zwitterion-like,  $\text{MR}^\pm$ . Our experiments cannot determine whether the  $\text{O}\cdots\text{H}\cdots\text{N}$  proton is closer to O or N within PA. In any case, whether the intramolecular H-bonding does or does not represent a genuine tautomerism, electrons are drawn from  $-\text{N}(\text{CH}_3)_2$ , giving the MR considerable quinoidal character and a red color.

A lone 2001 paper, standing apart from the early 20<sup>th</sup> century studies of PA/MR, describes the dyeing of another aromatic acid, 2,5-dihydroxybenzoic acid (DHB), with MR.<sup>89</sup> DHB, unlike some of its constitutional isomers, is an effective MALDI (matrix assisted laser desorption ionization mass spectrometry) matrix, but why it is effective

remains a subject of active research. In an effort to determine whether ions observed by MALDI were pre-formed in the host matrices, Krüger et al. used acid-base indicators such as MR as analytes.<sup>89</sup> They reasoned that the color of the mixed crystals formed between dye and host could be taken as a clear indication of the protonation state of the dye in the solid state. DHB micro-crystallites were red (judged only by eye, not with a spectrophotometer) when grown in the presence of MR, leaving the authors to conclude that the  $M + H^+$  ion observed in the gas phase was pre-formed in the mixed crystals. From our work with MR and PA, we can conclude that the state of a solvatochromic acid-base indicator in a crystal is not simply judged by color. We must modulate this criticism by emphasizing that we had earlier made the identical rush to judgment.<sup>59,60</sup>

#### 2.3.6.2 *Face Selectivity and Polarization*

The dominant intermolecular interaction in the 0.5PA·MR co-crystal structure is H-bonding between PA and MR COOH groups (see Figure 2.36). We might then reasonably assume that the H-bond donating ability of different surfaces might explain their selectivity for MR. The lowest energy surfaces of the expressed faces (110), and (001) are shown in Figure 2.32.

Indeed, both surfaces of which have exposed COOH groups and incorporate MR<sup>in</sup>.

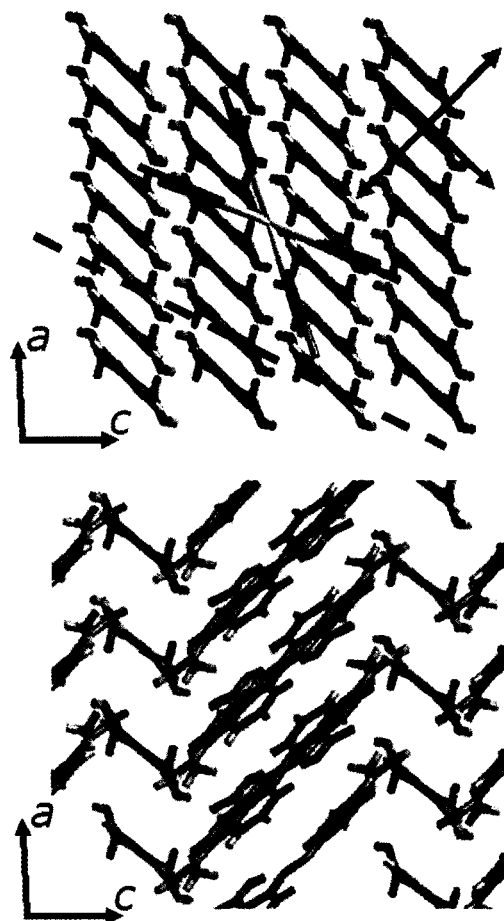


**Figure 2.36.** (Upper) Experimental MR orientations superimposed upon the PA lattice for the red species in {001} (red tips), red species in {110} (blue tips), and averaged MR<sup>o</sup> (purple tips). Dashed blue line is the (101) cleavage plane. (Lower) Co-crystal structure of 0.5PA·MR shows remarkable agreement with respect to PA sheets in both structures. The MR positions are

inconsistent with polarized absorbance data for the mixed crystals.

The long-axis of  $\text{MR}^{\text{in}}$  projected in (101) was inclined  $\sim 40^\circ$  from  $b$  when docked to the one unique site on (001) (Figure 2.32) in agreement with the dichroic ratio (see previous section). On the other hand, two unique positions are available for docking to (110):  $\text{MR}^{\text{in}}$  inclined approximately  $40^\circ$  from  $b$  and approximately parallel to  $a$ . Dichroic ratios for the (110) sector indicate that  $\text{MR}^{\text{in}}$  is oriented in (101) projection on average  $62^\circ$  from  $b$ . Thus, a combination of both orientations in a ratio of 3:5 respectively would give rise to this intermediate average orientation.

$\text{MR}^{\text{in}}$ , model I adsorbed to (110) (Figure 2.32), and MR adsorbed to (001), give rise to the orientation inside the crystal pictured in Figure 2.33b.  $\text{MR}^{\text{in}}$  model II adsorbed to (110) gives rise to the orientation inside the crystal pictured in Figure 2.33a. The difference in replacement energies between models Figure 2.33a and Figure 2.33b is less than 3 kcal/mol (Table 2.4). The third calculated orientation consistent with the replacement of one MR for two PAs, that with  $\text{MR}^{\text{in}}$  parallel to  $b$ , is nearly 6 kcal/mol higher in energy than  $\text{MR}^{\text{in}}$  parallel to  $a$ . No stable surfaces can dock  $\text{MR}^{\text{in}}$  parallel to

*b* via H-bonding. This geometry is not found within the PA crystals examined. It is not illustrated and is not considered further.

MR<sup>ex</sup> was found in every sector. Unlike MR<sup>in</sup>, the R<sub>2</sub><sup>2</sup>(8) hydrogen-bonding constraint permits only one orientation for this species within the PA lattice. The replacement energy for the MR<sup>ex</sup> inclusion was determined to be 2 kcal/mol less than the lowest energy MR<sup>in</sup> inclusion. Furthermore, the computed orientation of MR<sup>ex</sup> is 4° closer to [100] than MR<sup>in</sup> which agrees with the measured dichroic ratios.

### 2.3.6.3 *Phase Separation*

On heating PA/MR, the principal observation is the loss of dichroism for the low energy band when light is incident on (010). Loss of dichroism is consistent with the rotation of a subpopulation of MR<sup>in</sup> molecules by approximately 90° around *b*. Such a reorientation would position the molecules with respect to PA as is found in 0.5PA · MR. Could microscopic 0.5PA · MR domains form within PA/MR mixed crystals? Might we consider this process a syncrystallization but one that could not have been forecast in earlier generations because the structure of 0.5PA · MR had not been established?

**Table 2.5.** Similarities between 0.5 PA·MR structure and respective pure crystal structures

	MR	MR plane of co-crystal	% difference
Side 1	[100] = 8.235 (Å)	[110] = 8.422 (Å)	-2.27
Side 2	[110] = 9.160 (Å)	[100] = 9.083 (Å)	0.84
Angle	58.3°	57.4°	1.54

	PA	PA plane of co-crystal	% difference
Side 1	[010] = 14.318 (Å)	[010] = 14.185 (Å)	0.93
Side 2	[001] = 9.630 (Å)	[100] = 9.083 (Å)	5.68
Angle	90°	90°	0

The similarities between the crystals of PA and MR, with co-crystals 0.5PA·MR, are striking. For example, the disposition of rows of PA molecules in co-crystals matches very well with every fourth PA row in the pure crystal (Figure 2.36). A more quantitative comparison is achieved by describing the 2-D periodicity of the sheets of the 'pure' substances in the co-crystal, as well as matching planes in the pure crystals, by two vectors and the angle between them. The spatial distribution of the individual components in a plane in the co-crystal agrees quite well with planes found in the respective pure lattices (Table 2.5). By choosing a hydrogen bonded tetrad consisting of a MR dimer and two PA molecules from the co-crystal,

and superimposing the PA molecules of this tetrad onto the PA positions of the co-crystal, we find that the MR dimers are inclined by  $82^\circ$  with respect to the aromatic planes of PA layers in the pure acid. This model for the mixed crystals would imply that the polarization of maximum absorbance should be along [201]. This model is inconsistent with the polarization of  $\text{MR}^{\text{in}}$  in the mixed crystals that absorbs light maximally when the polarization is along  $[20\bar{1}]$ . Inferences of guest orientations within a host, established on the basis of the analysis of co-crystal structures - even when remarkable correspondences between the pure and co-crystal structures exist - should be drawn cautiously. The traditional importance of lattice matching in the overgrowth of one substance on another has been de-emphasized by Ward and coworkers in their studies of edge-directed epitaxy.<sup>90</sup>

$\text{MR}^{\text{in}}$  migrates within PA crystals following prolonged heating. It ultimately aggregates to form bâtonnets which then also migrate through the crystal. By contrast, the yellow species remains fixed within the lattice at elevated temperatures (Figure 2.37). This behavior is consistent with the model in which  $\text{MR}^{\text{ex}}$  is held tightly in place through the comparatively strong  $R_2^2(8)$  hydrogen bonds.



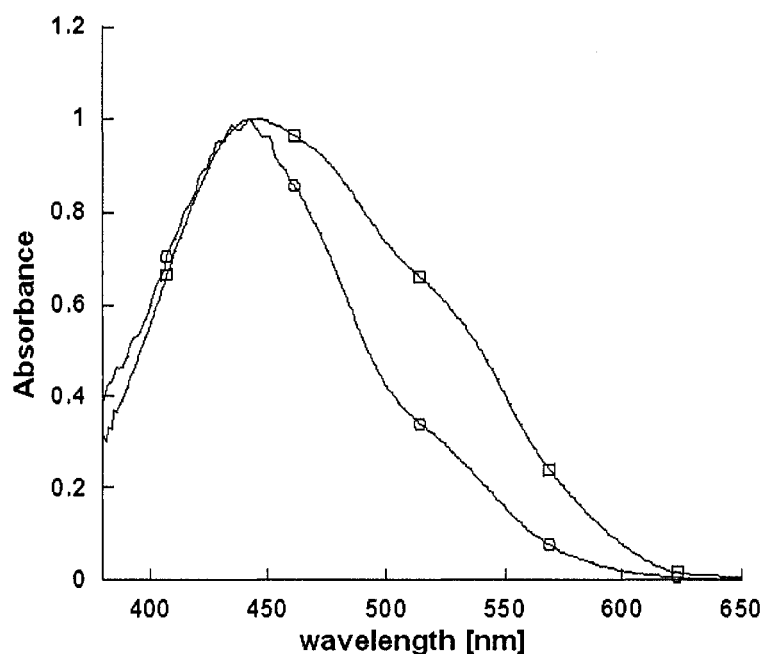


**Figure 2.37.** Normalized absorption spectra of {001} measured down [010] before (□) and after (○) heating. The intensity of the shoulder at 510 nm corresponding to  $MR^{in}$  is greatly diminished.

The hydrogen bonds between  $MR^{in}$  and the lattice lack the specificity and complementarity of  $MR^{ex}$  allowing for rearrangement and migration when heated. The unidirectional migration is most probably a consequence of initial fluctuations leading to a small MR rich aggregate. As PA recrystallizes in spaces vacated by  $MR^{in}$  it presumably lowers the free energy of the crystal and drives the aggregate in the direction opposing the

recrystallization. To the extent that MR rich crystals can be oriented within dyed PA, we can fairly state that we have witnessed a syncrystallization.

### 2.3.7 Conclusions: What is Syncrystallization?

Adjacent growth sectors of phthalic acid crystals grown from solutions containing MR are alternately yellow and red. The color difference is not a consequence of acid-base chemistry as earlier conjectured.<sup>60</sup> Rather, it is a consequence of the H-bond acceptor (intramolecular or intermolecular) to which neutral MR directs its COOH proton. The intermolecularly H-bonded yellow species (MR<sup>ex</sup>) is less selectively included in the crystal while the red dipolar species (MR<sup>in</sup>) is associated with hydrogen bonding surfaces. Sorting out the chromo-chemistry in PA/MR necessitated a detailed investigation into the structure of MR in various environments. We have thus compared MR crystal structures containing the neutral, zwitterionic, and protonated forms. Yet, the intermolecular interactions between MR and PA that were observed in co-crystals failed to predict the polarization of the MR in the mixed crystals. The absorption anisotropy could only be reckoned by considering the docking of MR to the most stable computed

surfaces and the replacement energies associated with variously oriented MRs within the PA lattice.

PA precipitation from MR containing solutions, of whatever relative concentration, does not yield PA crystals containing oriented microcrystals of MR. The interpretation of *syncrystallization* in the PA/MR system as an oriented overgrowth is baseless. Heating of the mixed crystals causes a MR reorientation, followed by a phase separation and recrystallization of a MR rich phase. Establishing whether or not these dynamic processes are consistent with the notion of syncrystallization is facilitated by placing the Gaubert/Neuhaus papers within the context of accepted terminology for the phenomena of regular mutual orientation of crystals of disparate substances.<sup>91</sup>

*Epitaxy*, the concept championed by Neuhaus, is used to describe the oriented growth of one substance on the crystal surface of another substance. Minerologists use *syntaxy*<sup>92</sup> to describe the simultaneous growth of mutually oriented crystals to two or more phases. Syntaxy is an accepted contemporary substitute for syncrystallization. *Endotaxy*<sup>93</sup> is used to designate oriented segregation taking place in the bulk of a crystal. Endotaxy embodies the process of exsolution, the disintegration of solid

solutions where the inclusions of the new phase are regularly oriented within the matrix. The terms *anomalous mixed crystals*, *partial-isomorphic mixed systems* (proposed by Spangenberg and Neuhaus<sup>94</sup>), and *adsorption mixed crystals*<sup>95</sup> have been proposed to account for oriented overgrowths/intergrowths/inclusions, but these terms have failed to gain wide currency.

Loss of MR dichroism on heating is consistent with MR reorientation so as to form supramolecular ensembles that resemble the 0.5PA-MR co-crystals. Strictly speaking, this process could well be considered endotactic, although the microcrystals formed may not be bigger than a few MR molecules.

The recrystallization of a MR rich phase within PA/MR mixed crystals may also be considered endotactic. We reemphasize that this is not the epitaxial co-crystallization assumed by Neuhaus.<sup>71</sup>

Other potential examples of syncrystallization/syntaxy of dyes with transparent host crystals from Gaubert's repertoire include methylene blue (CI# 52015) with lead nitrate<sup>96</sup> or urea oxalate<sup>97</sup>. The understanding of these

phenomena and others<sup>98</sup> could similarly benefit from contemporary reinvestigations.

### 2.3.8 *Experimental*

**Crystal Growth:** PA and MR were purchased from Aldrich and used without further purification. The growth solutions for crystals grown in a dish were prepared by dissolving proper amounts of the solids in neat ethanol followed by dilution with de-ionized water (Barnsted NANOpure, 18.2 M $\Omega$ /cm). Dye concentrations were based upon the molar concentration of initial growth solution volume. Solutions were evaporated in a dark cabinet at ambient temperature (23 °C). To grow microscopic crystals on glass slides a saturated aqueous solution of PA was heated to approximately 50 °C. 1.0 mL of the hot solution was placed on a microscope slide with appropriate volumes of a 1.0 mg/mL ethanol solution. Crystals grew in approximately 20 minutes. The slide was then rinsed with hexane.

Crystals of MR suitable for X-ray diffraction were obtained by cooling a saturated hot toluene solution to room temperature. Crystals of 0.5PA · MR were obtained by slow evaporation of an acetone solution containing 50 mg MR and 31 mg PA. Crystals of MR · HBr · H<sub>2</sub>O were obtained by slow

evaporation of 60 mL of methanol containing 100 mg MR and 0.968 mL 48% HBr in H<sub>2</sub>O. Crystals of 2,5-DHB · MR were obtained by slow evaporation of a saturated ethanol solution containing 0.10 g MR and 1.0 g 2,5-DHB.

**Spectroscopy:** Solution spectra were obtained with the cuvette sampling bench of the SI Photonics model 440 UV/Vis spectrophotometer. Crystal absorption spectra were obtained by coupling the spectrometer to an Olympus BX50 transmission microscope via a 200 μm fiber-optic. The extinction directions of the crystals were used to orient the sample relative to the input polarization. Instec HS400 heating stage with a platinum resistance temperature detector was used to drive the formation of the bâtonnets.

**Metripol:** In order to quantify linear anisotropies we have employed the rotating polarizer technique as embodied in the Metripol microscope.<sup>88</sup> The optical train consists of a filter as monochromator, a mechanically rotating polarizer, a sample inducing the phase shift  $\delta$ , a quarter wave retarder and a polarizer aligned at 45° towards the quarter wave plate's eigenray directions:

$$\mathbf{A}' = \mathbf{M}_{45-pol} \mathbf{M}_{\lambda/4} \mathbf{M}_{sample} \mathbf{R}_\theta \mathbf{J}_x \cdot$$

where  $J_x$  is the Jones matrix<sup>99</sup> for linearly polarized light operated on by a rotation matrix  $(R_\theta)$ , and Jones matrices representing the sample that is linearly birefringent ( $M_{\text{sample}}$ ), a quarter wave plate ( $M_{\lambda/4}$ ), and a linear polarizer ( $M_{45\text{-pol}}$ ). The position of the sample with respect to the rotating polarizer is defined by the angle  $\theta$ ,  $\theta = \alpha - \phi$ , where  $\alpha$  is the rotation angle of the polarizer and  $\phi$  the angle between the slow vibration direction of the sample and the polarizer when  $\alpha = 0$ . From the amplitudes, the normalized intensity  $I/I_0$  is found directly as:

$$\begin{aligned} \frac{I}{I_0} &= A'^* \cdot A' = 2 \cdot \frac{1}{4} \left[ (\cos \theta e^{ix} - \sin \theta e^{-ix}) (\cos \theta e^{-ix} - \sin \theta e^{ix}) \right] \\ &= \frac{1}{2} [1 + \sin 2(\alpha - \phi) \sin \delta] \end{aligned}$$

In the MetriPol method, intensity measurements at discrete steps ( $\alpha_i$ ) generate expressions that are easily converted to linear polynomials. Data collected over full periods yield Fourier coefficients from which the variable parameters are extracted analytically.

Simple modifications of the optical train permit the measurement of LD.<sup>100</sup> The anisotropic absorption may be determined by removing the quarter wave plate and analyzer. The Jones vector for a LD measurement using MetriPol is:

$$\mathbf{A}' = \mathbf{M}_{LD, LB} \mathbf{R}_\theta \mathbf{A}_x$$

$$\mathbf{A}' = t \cdot \begin{bmatrix} t_x e^{i\frac{\delta}{2}} & 0 \\ 0 & t_y e^{-i\frac{\delta}{2}} \end{bmatrix} \cdot \begin{bmatrix} \cos\theta & \sin\theta \\ -\sin\theta & \cos\theta \end{bmatrix} \cdot \begin{bmatrix} 1 \\ 0 \end{bmatrix} = t \cdot \begin{bmatrix} t_x e^{i\frac{\delta}{2}} \cos\theta \\ -t_y e^{-i\frac{\delta}{2}} \sin\theta \end{bmatrix},$$

where  $t$  is the average transmission coefficient,  $t_{x/y}$  are the transmission coefficients in the  $x$ ,  $y$  directions, and  $\theta$  is the initial angle between the polarizer and the slow vibration direction of the sample. After some manipulation,<sup>99</sup> we can relate  $\tanh\varepsilon$  ( $\varepsilon$  is the difference between optical densities in orthogonal directions) to the orthogonal transmission terms  $T'''$  giving:

$$\tanh\varepsilon = \frac{\sinh\varepsilon}{\cosh\varepsilon} = \frac{(e^{+\varepsilon} - e^{-\varepsilon})/2}{(e^{+\varepsilon} + e^{-\varepsilon})/2} = \frac{T' - T''}{T' + T''}.$$

**X-ray crystallography:** Crystals were indexed with a Stoe 2-circle Model J optical goniometer and a Nonius KappaCCD diffractometer. Data was collected with the KappaCCD using Mo  $K_\alpha$  radiation ( $\lambda = 0.71073$  Å). Integration of intensities and cell refinement was carried out using HKL2000<sup>101</sup> and HKL SCALEPACK respectively. Solution by direct methods (SIR97)<sup>102</sup> produced a complete heavy atom phasing model



consistent with the proposed structure. Structures were refined using SHELXL-97.<sup>103</sup> Non-hydrogen atoms were refined anisotropically by full-matrix least squares. All hydrogen atoms were refined with a riding model.

### CHAPTER 3 - LINEAR DICHROISM OF POLED POLYMERS

The assembly of optically responsive molecules so as to realize materials with macroscopic polarity is a popular challenge among engineers driven in part by the desire for fast electrooptic (EO) light modulators. The potential benefits of organic EO materials include low drive voltage operation, high bandwidth, and a multitude of processing techniques.<sup>104</sup> So compelling is the promise of organic EOs that the National Science Foundation established a Materials and Devices for Information Technologies Research Science and Technology (MDITR) Science and Technology Center at the University of Washington.

The EO modulator, a principal goal of MDITR researchers, is a device that can alter the phase or amplitude of a beam of light when a small driving voltage ( $\sim 1$  volt) is applied to the medium. A substantive change in a material's refractive index with the application of an electric potential will

only occur if the material lacks a center of inversion. Non-centrosymmetry is achieved in polymers doped with dye molecules having large dipole moments by the application of a large electric potential ( $\sim 1$  kV). This technique is called electric field poling.

Poling is applied to spun coat, thin polymer films ( $\sim 5$  microns) containing randomly oriented chromophores. After heating the film to a temperature that enhances molecular mobility, typically at or above the glass transition temperature of the matrix, the external electric field is applied to the film via a suitable system of electrodes. The material is then cooled such that the molecular orientations persist after the electric field is removed.

Chromophore reorientation impacts both the linear and non-linear optical (NLO) properties of the films. Because researchers are primarily interested in the EO properties fundamental to device operation, experimental characterization of the poled films typically emphasizes the measurement of EO coefficients.<sup>105</sup> While it is true that the EO parameters are of pivotal importance in terms of device performance and potential, they do not answers important questions requisite for rational device engineering and improvement: How many dyes are rotated during the poling process and to

what extent? What is the mechanism of decay of the EO activity? Does the poling field induce dye decomposition? These are questions that can be answered when NLO measurements are complimented by thorough characterization of the linear optical properties, in particular measurements of absorption anisotropy (linear dichroism) which occurs whenever an anisotropic distribution of chromophores is present.

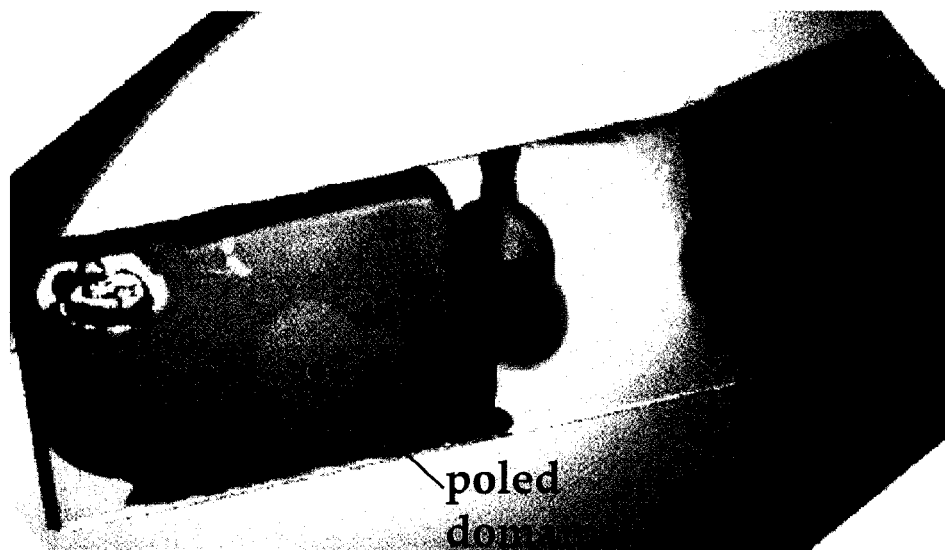


**Figure 3.1.** Photograph of Jen 3-3; a poled polycarbonate film doped with AJL-7. The lighter, more transmissive, poled domain is identified in the image.

Shown in Figure 3.1 is a photograph of a typical polycarbonate doped with a green charge transfer dye spun coat onto a conducting indium-tin

oxide (ITO) substrate. A gold dogbone had been applied to the top of the film, and subsequently removed by soaking in an aqueous potassium iodide solution. It is apparent that the optical density of the poled region that had been beneath the gold dogbone is less than that of the un-poled surroundings. Such an observation is consistent both with dye reorientation such that the electric dipole transition moments of the chromophores, likely aligned with the molecular dipoles in charge transfer dyes, are now perpendicular to the film plane. Thus, the cross section for absorption in normal incidence is diminished. On the other hand, it is quite possible that the delicate, highly conjugated chromophores have been destroyed or otherwise transformed in the poling process. This chapter describes a general method for measuring and characterizing the linear optical properties of poled polymer thin films using a polarized light microspectrophotometer. We show how the same set of measurements can be used to define both dye reorientation as well as the dye decomposition/transformation.

### 3.1 Background - Theory

The distribution of dipoles established in a medium by a dc electric field can be described as a function of solid angles,  $g(\phi, \theta)$ . Normalization gives:

$$\int_0^{2\pi} \int_0^\pi g(\theta) \sin \theta d\theta d\phi = 1$$

Assuming that the poling field is uniaxial, the distribution will be independent of  $\phi$ . The new distribution function is therefore:

$$\int_0^\pi g(\theta) \sin \theta d\theta = 1$$

This function can be expanded in terms of Legendre polynomials  $P_n$  according to standard procedures.<sup>106</sup>

$$g(\theta) = \sum_{n=0}^{\infty} \frac{i_n}{i_0} \frac{2n+1}{2} P_n(\cos \theta)$$

where  $i_n$  are spherical modified Bessel functions.

$$P_0(\cos \theta) = 1$$

$$P_1(\cos \theta) = \cos \theta$$

$$P_2(\cos \theta) = \frac{1}{2}(3 \cos^2 \theta - 1)$$

$$P_3(\cos \theta) = \frac{1}{2}(5 \cos^3 \theta - 3 \cos \theta)$$

$$P_4(\cos \theta) = \frac{1}{8}(35 \cos^4 \theta - 30 \cos^2 \theta + 3)$$

The first and third order polynomials or order parameters describe the part of the distribution responsible for the linear electro-optic effect.

Assuming a molecule aligned with the poling field in the  $z$  direction, having a dominant hyperpolarizability along  $z$ , then the microscopic polarization is:

$$p_z^\omega = \beta_{zzz} E_z^\omega E_z^0$$

The macroscopic polarizations that result from the optical field oriented perpendicular and parallel to the poling field are:

$$\chi_{333} = fN\beta_{zzz} \langle \cos^3 \theta \rangle$$

$$\chi_{113} = fN\beta_{zzz} \frac{1}{2} (\langle \cos \theta \rangle - \langle \cos^3 \theta \rangle)$$

So much has been said locally about the linear and cubic dependence on  $\theta$  in connection with electro-optic devices that we need not further concern ourselves with them. The even order parameters have been comparatively neglected. The fourth order parameter is difficult to measure requiring multi-photon techniques. This leaves the second order parameter which is related to the linear dichroism:

Wu has shown how the properties of spherically modified Bessel functions can be used to establish the following recurrence relation that links the linear and non-linear parts of the distribution function:<sup>107</sup>

$$\langle P_{n-1}(\cos\theta) \rangle - \langle P_{n+1}(\cos\theta) \rangle = [(2n+1)/x] \langle P_n(\cos\theta) \rangle.$$

Here, the proportionality constant  $x = \mu E/kT$  where  $\mu$  is the dipole moment and  $E$  is the poling field. The linear and non-linear properties that are a consequence of poling are intimately connected and one should not be considered in the absence of the other. They provide internal checks and balances.

Using transverse electrodes to pole a thermotropic polymer doped with a prototypical non-linear optical dye, 4-(dimethylamino)-4'-nitrostilbene (DANS), Meredith *et al.* were able to directly measure the linear dichroism resulting from the alignment of the chromophores. They stressed that the measurement of LD was "a necessary prerequisite for probing the second order non-linear optical properties."<sup>108</sup>

Generally, linear dichroism data is not reported in papers on poled polymers because researchers use a poling setup in which the field is applied perpendicular to the film plane, as opposed to the transverse scheme employed by Meredith *et al.*<sup>108</sup> This arrangement of electrodes, while convenient for poling and NLO measurements, precludes facile measurement of induced linear dichroism. We have, however, developed a method for characterizing the linear optical properties of poled polymer



films that may provide additional insight into potential chromophore degradation occurring within the film.

### 3.1.1 Angular Dependence of Linear Dichroism

In order to interpret the LD of films, we must first establish the function that describes the angular dependence of LD. In 1964, Zbinden proposed an ellipsoid to describe the absorption of infrared light incident on a dipole.<sup>109</sup> When a collection of dipoles is homogenously distributed about a main axis of orientation, as in a poled polymer film, Zbinden described the absorption ellipse according to the equation:

$$\frac{\cos^2 a}{\left(\sqrt{\frac{1}{A_x}}\right)} + \frac{\cos^2 b}{\left(\sqrt{\frac{1}{A_y}}\right)} + \frac{\cos^2 c}{\left(\sqrt{\frac{1}{A_z}}\right)} = A_{a,b,c}$$

where  $A$  is the absorption intensity and  $a$ ,  $b$ , and  $c$  represent the angles between the electric vector and the  $x$ ,  $y$ , and  $z$  axes, respectively. Unfortunately, for this model to yield an ellipse  $A_{a,b,c}$  would need to be a constant value. This will only occur when  $A_{a,b,c}$  is equal to  $A_x$ ,  $A_y$ , and  $A_z$ , the values for an isotropic system. As  $A_{a,b,c}$  varies in all other systems, a new model is requisite.

Gregoriou *et al.* have developed a model<sup>110</sup> based upon a core theorem of optics: Malus's law.<sup>111</sup> When linearly polarized light with an intensity,  $I_o$ , passes through a linear polarizer, the intensity of the transmitted light,  $I$ , is attenuated by a factor of  $\cos^2 \theta$ , the square of the projection of the electric vector of the light upon the polarizer axis, leading to the equation:

$$I = I_o \cos^2 \theta$$

Replacing the polarizer with an array of dipoles oriented parallel to the polarizer axis and a smaller number of dipoles oriented along a perpendicular axis, the transmitted intensity becomes

$$I(\theta) = I_o \cdot 10^{-A_{max}} \cdot \cos^2 \theta + I_o \cdot 10^{-A_{min}} \cdot \sin^2 \theta$$

where the decay terms account for the attenuation of light due to chromophore concentration and pathlength. Division by the common  $I_o$  term yields an expression for the transmittance of the sample:

$$T(\theta) = \frac{I(\theta)}{I_o} = 10^{-A_{max}} \cdot \cos^2 \theta + 10^{-A_{min}} \cdot \sin^2 \theta$$

Expressing the decay in terms of transmittance gives

$$T(\theta) = T_{min} \cdot \cos^2 \theta + T_{max} \cdot \sin^2 \theta$$

where  $\theta$  is the angle between the principle axes and the electric vector of the linearly polarized light and will be referred to as *the transmittance/absorbance model*.<sup>110, 112</sup>

The absorptance of the material,  $\alpha$ , is related to the materials transmittance by

$$T = 1 - \alpha; T_{min} = 1 - \alpha_{max}; T_{max} = 1 - \alpha_{min}$$

Substitution into the angular transmittance equation with subsequent rearrangement gives

$$\alpha(\theta) = \alpha_{max} \cdot \cos^2 \theta + \alpha_{min} \cdot \sin^2 \theta$$

Also appearing in the literature is a similar expression for the angular dependence of the absorbance<sup>1,113</sup>

$$A(\theta) = A_{max} \cdot \cos^2 \theta + A_{min} \cdot \sin^2 \theta$$

This function assumes that absorption transforms like a second rank polar tensor and will be referred to as *the absorbance model*. However, this assumption may not be valid as spectroscopic properties involving the interactions of photons with particles are not directly representable by tensors.<sup>114</sup> The fact that this function should still be at issue is remarkable.

But in stressing the use of absorptance as the quantity with a  $\cos^2 \theta$  dependence, Gregoriou *et al.* remark in 2004, “we settle, once and for all, the confusion that exists in the spectroscopic literature with regard to the dependence of absorption and transmission vis-à-vis the angle of incidence of the incoming light.”<sup>110</sup> Both models will be considered in our analysis of the linear optical properties of the polymer films.

The absorbance of a spherical sample containing an isotropic distribution of chromophores,  $A_{\text{iso}}$ , is related to its average absorption along the Cartesian coordinates by

$$A^{\text{iso}} = \frac{A_x^{\text{iso}} + A_y^{\text{iso}} + A_z^{\text{iso}}}{3} = A_x^{\text{iso}}$$

where  $A_x^{\text{iso}}$ ,  $A_y^{\text{iso}}$  and  $A_z^{\text{iso}}$  are the sample absorbances in the un-poled domains when the electric vector of linearly polarized light is co-linear with the sample  $x$ ,  $y$ , and  $z$  directions, respectively (1. Figure 3.2). Because all three directions are equivalent in an isotropic system,  $A^{\text{iso}}$  is equal to the most experimentally accessible value  $A_x^{\text{iso}}$ .

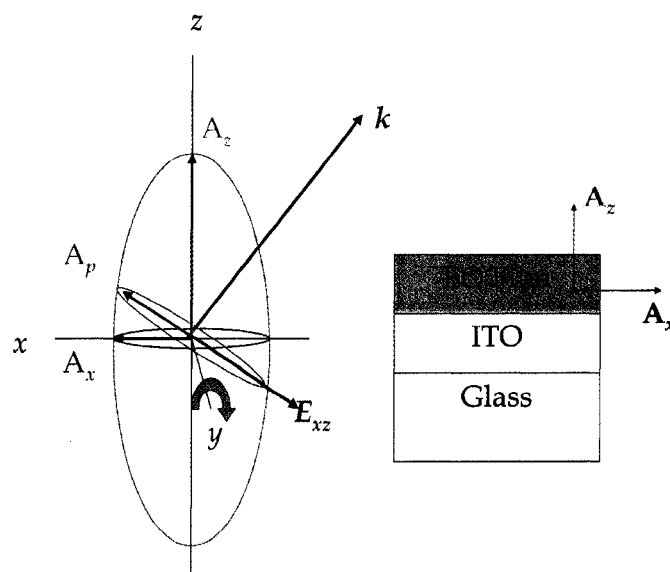


**Figure 3.2.** Schematic representation of the electric vector,  $E$ , in relation to the sample. Curved gray arrow indicates the axis of rotation.

In a uniaxial system where  $z$  is defined as the unique direction,  $x$  and  $y$  are degenerate; the anisotropic absorbance,  $A^{\text{anis}}$ , is related to the isotropic absorbance

$$A^{\text{iso}} = \frac{2A_x^{\text{anis}} + A_z^{\text{anis}}}{3}$$

Such a direct relationship between the optical density along principle axes and the isotropic absorption can only be expressed in terms of absorbance. The analogous absorptance (transmittance) equation

$$\alpha^{\text{iso}} = \frac{2\alpha_x^{\text{anis}} + \alpha_z^{\text{anis}}}{3}$$

would in some cases result in absorbances greater than 1. For example, if  $\alpha^{\text{iso}} = 0.8$  and  $\alpha_x^{\text{anis}} = 0.5$ , then  $\alpha_z^{\text{anis}} = 1.4$ , a physical impossibility. Such values are permitted for absorbance.

If chromophore reorientation is solely responsible for the induced absorption anisotropy, the orientationally averaged absorption ellipsoids for the poled and un-poled regions should be equivalent. The absorption in the z direction of the poled region becomes

$$A_z^{\text{anis}} = 3A_x^{\text{iso}} - 2A_x^{\text{anis}}$$

Because the absorbance in the poled region could be reduced by degradation or transformation to a non-absorbing species, measurement of  $A_z^{\text{anis}}$  would provide crucial experimental evidence to support the assumption that the differential absorption is entirely the result of chromophore reorientation. Unfortunately, directly measuring  $A_z^{\text{anis}}$  would require measuring the absorbance of the film with the light path parallel to the plane of the film. Knowledge of the theoretical  $A_z^{\text{anis}}$  does, however, enable the calculation of the film absorbance at intermediate angles of

incidence that are accessible by spectroscopy. By comparing the measured and calculated absorbances for different sample geometries one can determine the degree to which chromophore reorientation is responsible for the observed linear optical properties.

Not accounting for changes in pathlength, the absorbance of the poled region of a thin film being tilted by  $\theta$  about an axis parallel to the film plane using  $p$ -polarized light propagating perpendicular to the initial film plane follows the equation

$$A_p^{\text{anis}}(\theta) = (A_x^{\text{anis}}) \cos^2 \theta + (A_z^{\text{anis}}) \sin^2 \theta;$$

Expressed in terms of  $A_x^{\text{anis}}$  and  $A_x^{\text{iso}}$ , the equation becomes

$$A_p^{\text{anis}}(\theta) = (A_x^{\text{anis}}) \cos^2 \theta + (3A_x^{\text{iso}} - 2A_x^{\text{anis}}) \sin^2 \theta$$

Neglecting the change in pathlength, the absorbance of the un-poled (isotropic) domain should remain constant when the proceeding rotations are performed such that

$$A_p^{\text{iso}}(\theta) = A_x^{\text{iso}}$$

Similar equations are used for the absorptance model:

$$\alpha_p^{\text{anis}}(\theta) = \alpha_x^{\text{anis}} \cos^2 \theta + \alpha_z^{\text{anis}} \sin^2 \theta$$

Expressed in terms of  $A_x^{\text{anis}}$  and  $A_x^{\text{iso}}$ , the equation becomes

$$\alpha_p^{\text{anis}}(\theta) = (1 - 10^{-A_x^{\text{anis}}}) \cos^2 \theta + (1 - 10^{-(3A_x^{\text{iso}} - 2A_x^{\text{anis}})}) \sin^2 \theta$$

Likewise, the absorptance of the un-poled (isotropic) domain should remain constant when the proceeding rotations are performed such that

$$\alpha_p^{\text{iso}}(\theta) = \alpha_x^{\text{iso}}$$

### 3.1.2 Corrections

In making measurements of the linear dichroism of thin, anisotropic films in non-normal incidence, there are many corrections that must be applied to the data or alternatively evaluated and justifiably dismissed. Among these are the following:

- Pathlength corrections due to Snell's laws
- Corrections to the pathlength due to the fact that in birefringent systems, the extraordinary ray does not conform to Snell's law.
- Reflection linear dichroism corrections
- Reflectance corrections accounting for the complex refractive index in absorbing media
- Corrections due to the conicity of the light pencil
- Corrections due to increasing the area of illumination at increasing angle
- Corrections for multiple reflection



The issues will be evaluated in series before proceeding with the experimental data on thin films and their analysis. However, by restricting our measurements to incident *p*-polarization, and by taking advantage of the internal standard which is the un-poled region of the film, we can quickly evaluate the extent to which the reduction in optical density of the EO films in normal incidence after poling is a consequence of dye reorientation or degradation/transformation to a non-absorbing state.

### 3.1.2.1 Pathlength Corrections

Any region of the film will darken as the film is tilted due to an increasing pathlength for the propagating light. Using Snell's law to account for refraction through the medium the absorbance as a function of tilt angle becomes

$$A_{corr}(\theta) = \frac{A_x(\theta)}{\cos(\arcsin(\frac{n_1}{n_2} \sin \theta))}$$

$$\alpha(\theta) = 1 - 10^{-A_{corr}(\theta)}$$

where  $A_x$  is the film absorbance measured normal to the film plane and  $n_1$  and  $n_2$  are the refractive indices of oil and the polymer, respectively.

What is the justification for choosing  $n_1$  and  $n_2$  as the refractive indices of polymer and oil? The optical path is as follows: air>glass>mineral oil>glass>ITO>doped polymer>mineral oil>air. We are principally concerned with the path the light will take through the polymer layer. The initial air-glass and glass-mineral oil interfaces will always be perpendicular to the propagation direction of the incident light, thus refraction will not occur at these interfaces. As the sample is inclined with respect to the incident radiation, refraction will occur altering the trajectory through the layers; however, the beam will emerge from and refract into each successive layer as if entering the new layer directly from mineral oil.

Consider light propagating through a medium with a refractive index,  $n_1$ , impinging on two parallel layers with differing refractive indices,  $n_2$  and  $n_3$ , at an angle  $\theta_1$ . The angle of the light through the second layer can be determined by Snell's Law:

$$n_1 \sin \theta_1 = n_2 \sin \theta_2$$

The angle through layer three is likewise obtained from the trajectory through layer 2.

$$n_2 \sin \theta_2 = n_3 \sin \theta_3$$

The two equations can be combined to yield an expression for  $\theta_3$  that only depends on the properties of the first and third layers:

$$n_1 \sin \theta_1 = n_3 \sin \theta_3$$

Thus the refraction of the light through the glass and ITO layers of the substrate can be safely ignored when calculating the trajectory of light through the doped polymer layer.

### 3.1.2.2 *Corrections to the Pathlength Correction*

The pathlength correction is derived from Snell's law. However, Snell's law can only be an approximation in anisotropic media. The *p*-polarized light with the electric field in the plane of incidence is the so-called extraordinary ray which does not obey Snell's law. Hasegawa have derived a simple refraction law for uniaxial anisotropic media.<sup>115</sup>

The author's show that the pathlength deviation between the ordinary and extraordinary rays is about 3° for a very large birefringence of 0.18. The films that we will be dealing with have much smaller values of birefringence, meaning that we can safely take Snell's pathlength for the calculation for absorption at various angles of incidence.

### 3.1.2.3 *Reflection linear dichroism corrections*

Due to Fresnel reflection, tilted samples will suffer reflection linear dichroism which is a consequence of the angular dependencies at the interfaces. Here, interfaces with large refractive index differences are that between air and glass, between mineral oil and glass, between glass and ITO, between ITO and polymer, and between polymer and mineral oil, and between mineral oil and air. At each interface, we should expect reflectance to diminish the transmitted light according to Fresnel's formula in combination with the formula for the conservation of energy.<sup>116</sup>

$$t_p = \frac{2 \sin \theta_i \cos \theta_t}{\sin(\theta_i + \theta_t) \cos(\theta_i - \theta_t)}$$

$$r^2 + t^2 \frac{n_2 \cos \theta_t}{n_1 \cos \theta_i} = 1$$

Applying these formulas with an incident angle of 40, we discover that that >99% of light is transmitted at the ITO interfaces. At the air glass interface with transmit only 94% and at the oil air interface with transmit only 90%. However, since all measurements will suffer losses at these interfaces in the same way, we can ignore transmittance corrections.

#### 3.1.2.4 Transmittance Corrections for Complex Refractive Indices

Of course, as we are dealing with absorbing media the refractive index must be taken as a complex quantity,  $n' = n + ik$ .

#### 3.1.2.5 Corrections due to the conicity of the light pencil

Nordén et al. have considered corrections to linear dichroism that is a consequence of the conicity of the light pencil.<sup>117</sup> That is, they argue that for an angular spread,  $\alpha$ , of the electric vector of the incident light, the quantity  $(A_s - A_p)/(A_s + A_p)$  should be multiplied by  $\sin\alpha(\cos 2/2\alpha)$ . However they quickly concluded in their studies of the orientation of chromophores in membranes that for small values of  $\alpha$ , a reasonable assumption in orthoscopic illumination, this correction can be safely neglected.

#### 3.1.2.6 Correction for Increasing Illumination Area

Lopes et al. pointed out that the dichroic ratio at non-normal incidence should be corrected by the term  $\sin(\omega)$  where  $\omega$  represents  $90 - \theta$ .<sup>118</sup> This is because the area of illumination increases as  $\omega$  decreases. This correction may be neglected as it applies equally to the poled and un-poled reference regions.

### 3.1.2.7 Corrections for Multiple Reflections

The problem of multiple reflection was treated by Johansson et al.<sup>119</sup> Multiple reflections affect measured LD due to differences in Fresnel reflections for different polarizations. However, as we will show, all of our measurements of LD are computed from measurements with a single polarization. Therefore, we ignore the affect of multiple reflections.

### 3.1.3 The Equivalence Point

One consequence of the z-direction being more strongly absorbing than the isotropic domain is the presence of an equivalence point. The poled region and the un-poled region will possess equal optical densities when the sample is tilted to an angle,  $\theta_{eq}$ , in the presence of  $p$ -polarized light.

$$A_p^{iso}(\theta_{eq}) = A_p^{anis}(\theta_{eq});$$

$$T_p^{iso}(\theta_{eq}) = T_p^{anis}(\theta_{eq});$$

$$\alpha_p^{iso}(\theta_{eq}) = \alpha_p^{anis}(\theta_{eq});$$

If the absorbance model for the angular dependence of the linear dichroism is correct, the expressions become

$$\begin{aligned}
A_p^{\text{iso}}(\theta_{\text{eq}}) &= A_p^{\text{anis}}(\theta_{\text{eq}}); \\
A_x^{\text{iso}} &= A_x^{\text{anis}} \cos^2 \theta_{\text{eq}} + A_z^{\text{anis}} \sin^2 \theta_{\text{eq}} \\
A_x^{\text{iso}} &= A_x^{\text{anis}} \cos^2 \theta_{\text{eq}} + (3A_x^{\text{iso}} - 2A_x^{\text{anis}}) \sin^2 \theta_{\text{eq}} \\
A_x^{\text{iso}} &= A_x^{\text{anis}} \cos^2 \theta_{\text{eq}} + (3A_x^{\text{iso}} - 2A_x^{\text{anis}}) - (3A_x^{\text{iso}} - 2A_x^{\text{anis}}) \cos^2 \theta_{\text{eq}} \\
-(2A_x^{\text{iso}} - 2A_x^{\text{anis}}) &= -(3A_x^{\text{iso}} - 3A_x^{\text{anis}}) \cos^2 \theta_{\text{eq}} \\
\frac{-(2A_x^{\text{iso}} - 2A_x^{\text{anis}})}{-(3A_x^{\text{iso}} - 3A_x^{\text{anis}})} &= \cos^2 \theta_{\text{eq}} \\
\cos^2 \theta_{\text{eq}} &= \frac{2}{3}; \\
\theta_{\text{eq}} &\approx 35.2^\circ
\end{aligned}$$

The absorbance model predicts an invariant equivalence point when the  $p$ -polarized light is  $35.2^\circ$  from the  $x$ -axis within the sample ( $54.7^\circ$  from the  $z$ -axis, the magic angle); the equivalence point does not depend on any initial conditions. This, however, assumes absorbance follows a  $\cos^2 \theta$  function and 100% of the differential absorbance between the poled and un-poled region is the result of chromophore reorientation.

If the absorptance/transmittance model correctly describes the angular dependence of the transmitted intensity of the sample, the equations become

$$\begin{aligned}
\alpha_p^{\text{iso}}(\theta_{\text{eq}}) &= \alpha_p^{\text{anis}}(\theta_{\text{eq}}); \\
\alpha_x^{\text{iso}} &= \alpha_x^{\text{anis}} \cos^2 \theta_{\text{eq}} + \alpha_z^{\text{anis}} \sin^2 \theta_{\text{eq}} \\
T_p^{\text{iso}}(\theta_{\text{eq}}) &= T_p^{\text{anis}}(\theta_{\text{eq}}); \\
T_x^{\text{iso}} &= T_x^{\text{anis}} \cos^2 \theta_{\text{eq}} + T_z^{\text{anis}} \sin^2 \theta_{\text{eq}}
\end{aligned}$$

The remainder of the derivation will be presented in terms of transmittance as the expressions are simpler and more straightforward.

Expressing  $T_z^{\text{anis}}$  in terms of  $T_x^{\text{iso}}$  and  $T_x^{\text{anis}}$  gives

$$\begin{aligned}
A_z^{\text{anis}} &= 3A_x^{\text{iso}} - 2A_x^{\text{anis}} \\
-\log T_z^{\text{anis}} &= 3(-\log T_x^{\text{iso}}) - [2(-\log T_x^{\text{anis}})] \\
\log T_z^{\text{anis}} &= \log[(T_x^{\text{iso}})^3] - \log[(T_x^{\text{anis}})^2] \\
T_z^{\text{anis}} &= \frac{(T_x^{\text{iso}})^3}{(T_x^{\text{anis}})^2}
\end{aligned}$$

The expression for the equivalence point becomes

$$T_x^{\text{iso}} = T_x^{\text{anis}} \cos^2(\theta_{\text{eq}}) + \left( \frac{(T_x^{\text{iso}})^3}{(T_x^{\text{anis}})^2} \right) \sin^2(\theta_{\text{eq}})$$

Solving for  $\theta_{\text{eq}}$



$$\cos^2(\theta_{\text{eq}}) = \frac{T_x^{\text{iso}} - \frac{(T_x^{\text{iso}})^3}{(T_x^{\text{anis}})^2}}{T_x^{\text{anis}} - \frac{(T_x^{\text{iso}})^3}{(T_x^{\text{anis}})^2}}$$

$$\theta_{\text{eq}} = \arccos \sqrt{\frac{T_x^{\text{iso}} - \frac{(T_x^{\text{iso}})^3}{(T_x^{\text{anis}})^2}}{T_x^{\text{anis}} - \frac{(T_x^{\text{iso}})^3}{(T_x^{\text{anis}})^2}}}$$

The equivalence point can also be expressed in terms of  $T_x^{\text{anis}}$  and  $T_z^{\text{anis}}$

$$\cos^2(\theta_{\text{eq}}) = \frac{((T_x^{\text{anis}})^2 \times T_z^{\text{anis}})^{\frac{1}{3}} - T_z^{\text{anis}}}{T_x^{\text{anis}} - T_z^{\text{anis}}}$$

$$\theta_{\text{eq}} = \arccos \sqrt{\frac{((T_x^{\text{anis}})^2 \times T_z^{\text{anis}})^{\frac{1}{3}} - T_z^{\text{anis}}}{T_x^{\text{anis}} - T_z^{\text{anis}}}}$$

Unlike the absorbance model, the absorptance model does not have an invariant equivalence point (Figure 3.3). Plotting the equivalence point as a function of anisotropic transmission coefficients reveals that in the limit of low dichroism ( $T_z - T_x \approx 10^{-4}$ ) and low optical density ( $T_x \approx T_z \approx 1.0$ ) the equivalence point approaches the value determined using the absorbance model:  $54.7^\circ$  from  $z$ . Unlike the absorbance model, however, the transmittance model predicts that the equivalence point will move towards  $z$  as either the optical density or the transmittance anisotropy increases.

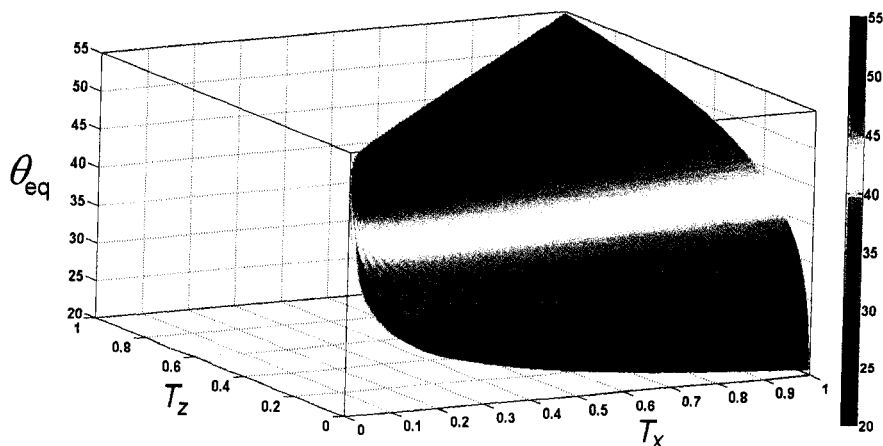


**Figure 3.3.** Plot of the equivalence point (in degrees from the z-axis) obtained using transmittance equations as a function of the transmittance of two orthogonal polarizations in an anisotropic domain ( $T_z < T_x$ ).

Again, both models are based upon the assumption that the absorption anisotropy is entirely the result of chromophore reorganization.

#### 3.1.4 Chromophore Transformation

The possibility of chromophore transformation to a non-absorbing species is seldom addressed in the poling literature.<sup>105</sup> Recent work established an order parameter,  $\Phi$ , to characterize the axial orientation of the poled chromophores<sup>120</sup> given as

$$\Phi = 1 - \frac{A}{A_0}$$

where  $A$  and  $A_0$  are the absorbances of the poled and un-poled regions, respectively, at normal incidence;  $A_x^{\text{anis}}$  and  $A_x^{\text{iso}}$ , respectively, as defined earlier in this chapter. This order parameter assumes that  $\Delta A$  between the two domains is solely the result of chromophore reorientation. The researchers test this supposition by heating the film to its glass transition temperature for 20 minutes recovering 95% of the pre-poled absorbance of the poled domain. While a recovery of 95% is substantial, the 5% loss represents nearly a third of the reported initial 17% reduction in absorbance due to poling. The poling induced transformation of a chromophore into a non-absorbing species will significantly impact the linear optical properties of the film. The transformation to a non-absorbing species must be accommodated to improve the modeling of the films.

Little is known about the mechanism of transformation of the chromophores; the parameter will be introduced as an isotropic correction such that the differential absorbance between the poled and un-poled regions is a combination of chromophore reorientation,  $A^{\text{anis}}$ , and chromophore transformation,  $A^{\text{trans}}$ , expressed as

$$A^{\text{iso}} = A^{\text{anis}} + A^{\text{trans}} = \frac{2A_x^{\text{anis}} + A_z^{\text{anis}}}{3} + A^{\text{trans}}$$

Using the absorbance model, the expression for the equivalence point becomes

$$A_p^{\text{anis}}(\theta) = A_x^{\text{anis}} \cos^2 \theta + (3A_x^{\text{iso}} - 3A^{\text{trans}} - 2A_x^{\text{anis}}) \sin^2 \theta$$

Expressed as a common  $\cos^2 \theta$  term gives

$$A_p^{\text{anis}}(\theta) = (2A_x^{\text{iso}} - 3A^{\text{trans}} - 2A_x^{\text{anis}}) - (3A_x^{\text{iso}} - 3A^{\text{trans}} - 3A_x^{\text{anis}}) \cos^2 \theta$$

Again, the equivalence point occurs when  $A_p^{\text{anis}}(\theta)$  is equal to the absorbance for the un-poled region,  $A_p^{\text{iso}}(\theta)$ ; the pathlength is omitted as it is identical for both domains giving

$$\begin{aligned} A_p^{\text{iso}}(\theta_{\text{eq}}) &= (2A_x^{\text{iso}} - 3A^{\text{trans}} - 2A_x^{\text{anis}}) - (3A_x^{\text{iso}} - 3A^{\text{trans}} - 3A_x^{\text{anis}}) \cos^2 \theta_{\text{eq}}; \\ A_x^{\text{iso}} &= (2A_x^{\text{iso}} - 3A^{\text{trans}} - 2A_x^{\text{anis}}) - (3A_x^{\text{iso}} - 3A^{\text{trans}} - 3A_x^{\text{anis}}) \cos^2 \theta_{\text{eq}} \end{aligned}$$

Solving for  $\cos^2 \theta$  results in the expression

$$\cos^2 \theta_{\text{eq}} = \frac{2A_x^{\text{iso}} - 3A^{\text{trans}} - 2A_x^{\text{anis}}}{3A_x^{\text{iso}} - 3A^{\text{trans}} - 3A_x^{\text{anis}}}$$

The earlier equivalence point equation with no transformation parameter is replicated by examining the equation in the limit of  $A_{\text{trans}}$  going to zero

$$\lim_{A^{\text{trans}} \rightarrow 0} \cos^2 \theta_{\text{eq}} = \frac{2}{3}$$

Using the absorptance/transmittance model, the equivalence point becomes

$$T_x^{\text{iso}} = T_x^{\text{anis}} \cos^2(\theta_{\text{eq}}) + T_z^{\text{anis}} \sin^2(\theta_{\text{eq}})$$

Expressing  $T_z^{\text{anis}}$  in terms of  $T_x^{\text{iso}}$ ,  $T_x^{\text{anis}}$ , and the transformation parameter,

$$T^{\text{trans}}$$

$$T_z^{\text{anis}} = \frac{(T_x^{\text{iso}})^3}{(T^{\text{trans}})^3 \times (T_x^{\text{anis}})^2}$$

The equivalence point becomes

$$T_x^{\text{iso}} = T_x^{\text{anis}} \cos^2(\theta_{\text{eq}}) + \frac{(T_x^{\text{iso}})^3}{(T^{\text{trans}})^3 \times (T_x^{\text{anis}})^2} \sin^2(\theta_{\text{eq}})$$

$$\cos^2(\theta_{\text{eq}}) = \frac{T_x^{\text{iso}} - \frac{(T_x^{\text{iso}})^3}{(T^{\text{trans}})^3 \times (T_x^{\text{anis}})^2}}{T_x^{\text{anis}} - \frac{(T_x^{\text{iso}})^3}{(T^{\text{trans}})^3 \times (T_x^{\text{anis}})^2}}$$

$$\theta_{\text{eq}} = \arccos \sqrt{\frac{T_x^{\text{iso}} - \frac{(T_x^{\text{iso}})^3}{(T^{\text{trans}})^3 \times (T_x^{\text{anis}})^2}}{T_x^{\text{anis}} - \frac{(T_x^{\text{iso}})^3}{(T^{\text{trans}})^3 \times (T_x^{\text{anis}})^2}}}$$

In both models, as the transformation parameter increases the equivalence point increases moving closer to the z-axis. If the

transformation parameter is large enough, the equivalence point will vanish; the isotropic domain will appear darker than the anisotropic domain for all rotations. In theory, the complete characterization of the linear optical properties of a poled polymer film can be realized by measuring three experimental observables,  $A_x^{\text{iso}}$ ,  $A_x^{\text{anis}}$ , and  $\theta_{\text{eq}}$ . The measurement of an equivalence point greater than the calculated theoretical equivalence point can provide a unique assay for determining the degree of chromophore transformation occurring in the film as a result of the poling process.

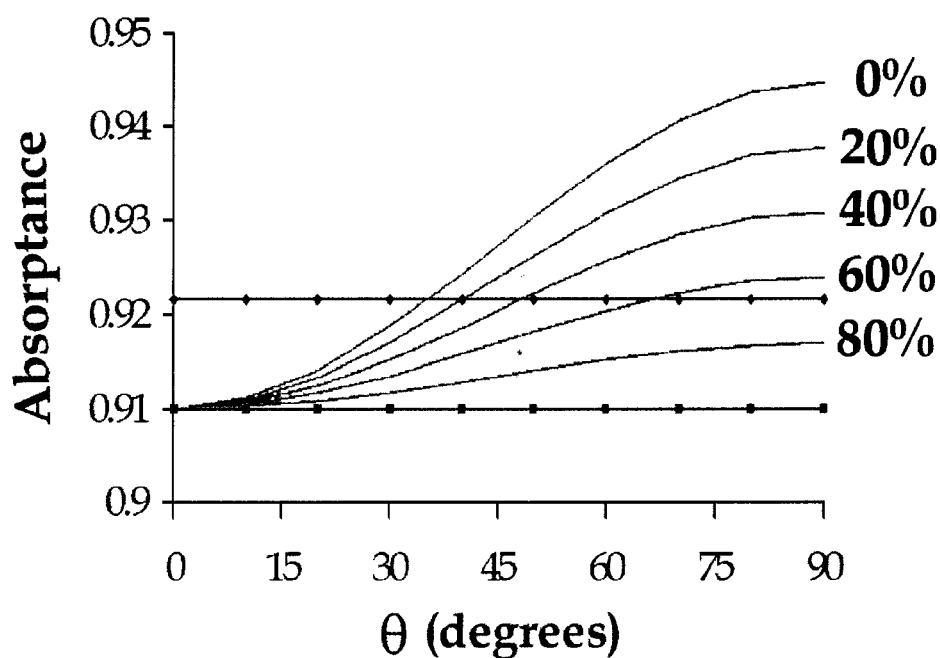


**Figure 3.4.** Calculated absorbances as a function of the internal angle for a thin film where  $\alpha_x^{\text{unpol}} = 0.922$  and  $\alpha_x^{\text{pol}} = 0.910$ . The blue line ( $\diamond$ ) represents an isotropic un-poled domain. The red line ( $\square$ ) is the absorbance of an isotropic poled domain; the differential absorbance (0.012) between the poled and un-poled domains is 100% transformation. The green lines represent the absorbance of the poled domain with various values for the transformation parameter. The equivalence point for the sample occurs when the blue and green lines intersect.

### 3.2 Polymer Film Preparation

The suitable optical quality films that we had access to were made by others using a typical sample preparation used in electrooptics laboratories.<sup>105</sup> The desired wt. % of dye and polymer host were dissolved such that the solid content in cyclopentanone was 12 wt. %. The samples were spun coat onto an indium-tin oxide (ITO) coated glass slide in a laminar flow bench in air using a spread of 500 rpm for 3 seconds and spin speeds ranging from 1100 to 1450 rpm for 20 seconds. The films were then soft baked in air on a hot plate at 65 °C for 10 minutes. The films were then baked in an oven over night at 85 °C under vacuum.

Once the gold electrodes were deposited, the samples were contact poled under nitrogen according to the conditions listed in Table 3.1. The electrooptic coefficient was measured at the 1.3  $\mu\text{m}$  wavelength by the simple reflection method.<sup>121</sup>



**Table 3.1.** Summary of poled polymer films including preparation details, qualitative observations, and qualitative observations of the linear and non-linear optical properties.

Sample ID	Provider	Polymer	Dye	Dye Conc. (wt.%)	Film thickness (mm)	Poling field (V/mm)	Poling temp (°C)	Poling time (min.)	EO response (pm/V)	crossover (θ)	Hue shift of poled region	Film Texture from Reflectance Observations	Comments
2-2	Jen	APC	AJL-7	?	?	100	165	?	70	47.5	None	Smooth	
1-3	Jen	APC	AJL-7	?	?	100	130	?	36	37.5	None	Smooth	
3-3	Jen	APC	AJL-7	?	?	140	?	?	87	42.5	None	Smooth	
1	Dalton	APC	YLII	25	1.4	60	135	?	62	N/A	N/A	Smooth	
2-2	Dalton	APC	YLII	25	1.4	80	135	?	70	N/A	N/A	Smooth	
2-3	Dalton	APC	YLII	25	1.4	100	135	?	86	N/A	N/A	Smooth	
unlabeled	Dalton	APC	YLII	25	1.9	Not poled	N/A	N/A	0	N/A	N/A	Smooth	
1-2	Jen	APC	AJL-8	25	1-1.3	50	135	2	16	40	slightly bluer	Rippled	Transparent Halo
1-1	Jen	APC	AJL-8	25	1-1.3	75	135	2	28	90	None	Rippled	Transparent Halo
9-3	Jen	APC	AJL-8	25	1-1.3	100	135	2	50	0	None	Rippled	
4-2	Jen	APC	AJL-8	25	1-1.3	125	135	2	65	35	None	Rippled	
9-2	Jen	APC	AJL-8	25	1-1.3	100	130	2	52	N/A	None	Rippled	
4-1	Jen	APC	AJL-8	25	1-1.3	100	125	2	22	90	None	Rippled	
13-3	Jen	APC	AJL-8	25	1-1.3	100	135	0	52	47.5	None	Rippled	
14-1	Jen	APC	AJL-8	25	1-1.3	100	135	10	42	N/A	None	Rippled	Dark Halo
14-2	Jen	APC	AJL-8	25	1-1.3	100	135	20	46	90	None	Rippled	Transparent Halo
19	Dalton								52	42.5	Slightly bluer	Smooth	
31b5	Dalton								50	52.5	None	Smooth	
31c4	Dalton								40	62.5	Slightly bluer	Smooth	
63b	Dalton								42	55	None	Smooth	
63a	Dalton								22	55	Slightly bluer	Smooth	
54a	Dalton								15	42.5	Much bluer	Smooth	
31a3	Dalton								35	37.5	None	Smooth	
54c	Dalton								38	60	Much bluer	Smooth	

Information not provided

### 3.3 NLO Film Optical Characterization

#### *3.3.1 Qualitative Observations*

Electrooptically (EO) active amorphous polycarbonate films containing various NLO chromophores were provided by the research groups of Professors Larry Dalton (Chemistry, UW) and Alex K.-Y. Jen (Materials Science, UW). The structures of the guest dye molecules are given in Figure 3.5. The films were initially inspected under reflected light using a field microscope to ensure the poling electrodes had been completely removed. In a similar manner, the texture of the surface was inspected; surface texture is indicative of non-uniform film thickness. Damage to the film (bleaching or charring) and streaking, presumably due to incomplete dye dissolution was identified by viewing the films with transmitted light. A summary of these observations as well as the poling conditions and EO properties of all films examined is listed in 9. Table 3.1.

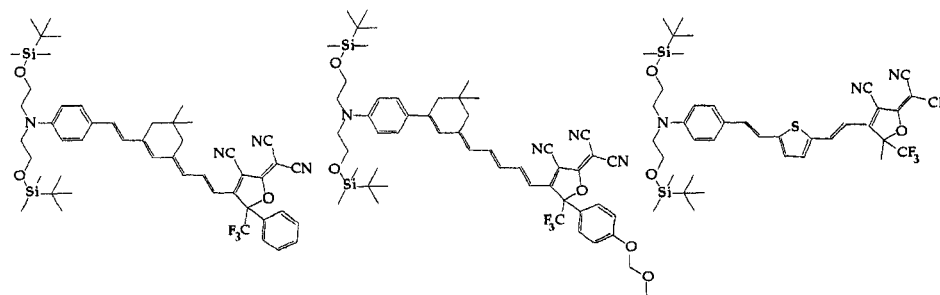


**Figure 3.5.** Structures of (left to right) YLII, AJL-7, and AJL-8.

The first two sets of films provided by the Jen and Dalton groups, the AJL-7 and YLII series, displayed very smooth surfaces when viewed under reflected light. Every film in the AJL-8 series possessed a pronounced rippling texture. Several of the films in this series were also clearly damaged. A transparent halo tracing an outline of the removed poling electrode was observed in three samples: 2-1, 1-1, and 14-2 (Figure 3.6). A dark halo was observed in sample 14-1. Hue shifts in the poled domain relative to the un-poled domain were also observed in a number samples analyzed.

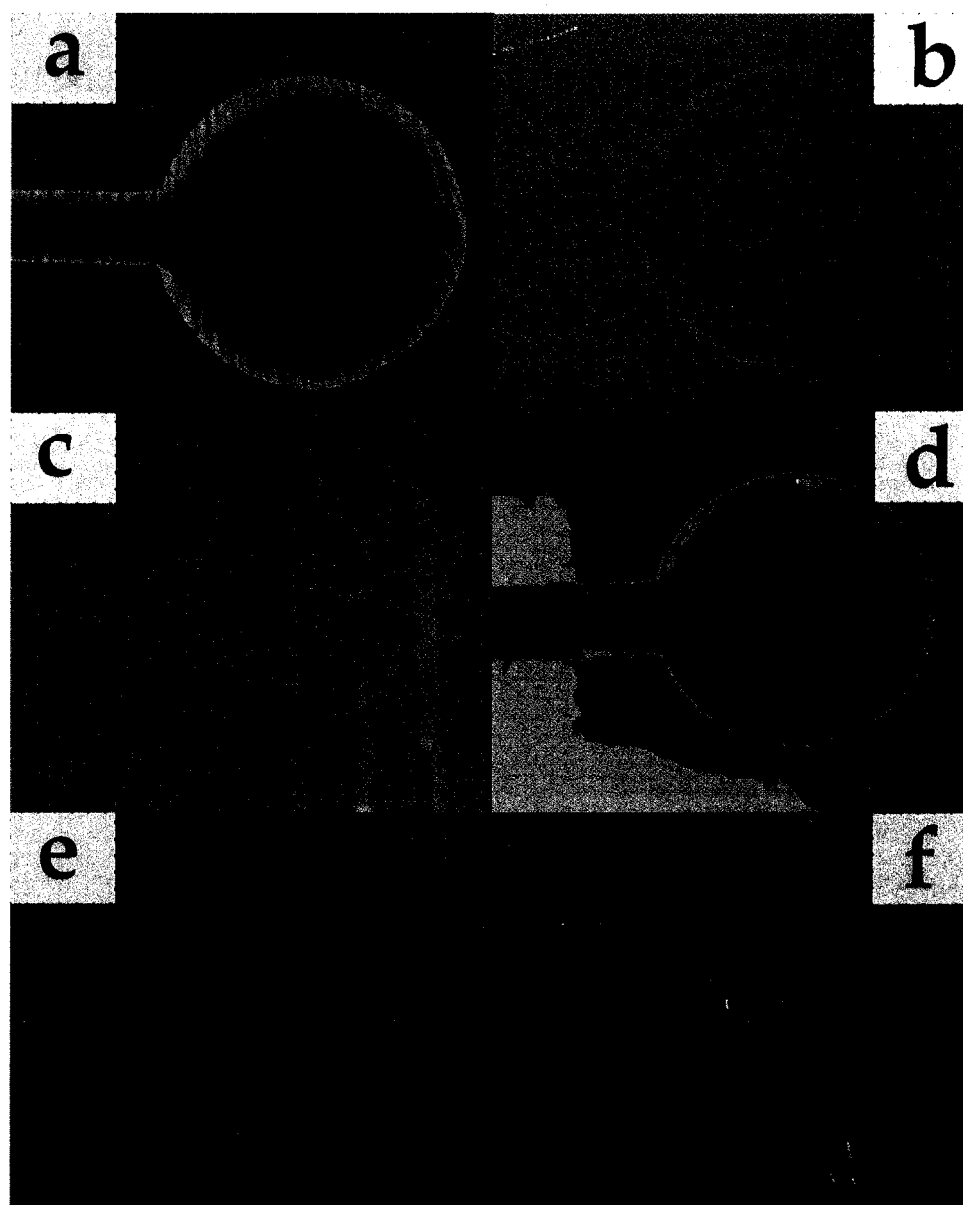


**Figure 3.6.** Optical micrographs of various poled polymer samples: a) Jen 1-1, b) Jen 1-2, c) Jen 4-1, d) Jen 14-2, e) Dalton-54a, and f) Dalton-54c. Micrographs a, b and d exhibit pronounced damage along the electrode border. The striations observed in a and c coincide with ripples observed under reflected light and are apparently the result of surface texturization. A dark

streak arising from inhomogeneous dye distribution is indicated by an arrow in micrograph c. Hue shifts of the poled domain relative to the un-poled domain are illustrated in films b, e, and f. Any additional unusual features (scratches, etc...) seen in the micrographs but not mentioned above likely occurred while the films were in our possession.

### 3.3.2 Quantitative Analysis

#### 3.3.2.1 Equivalence Point

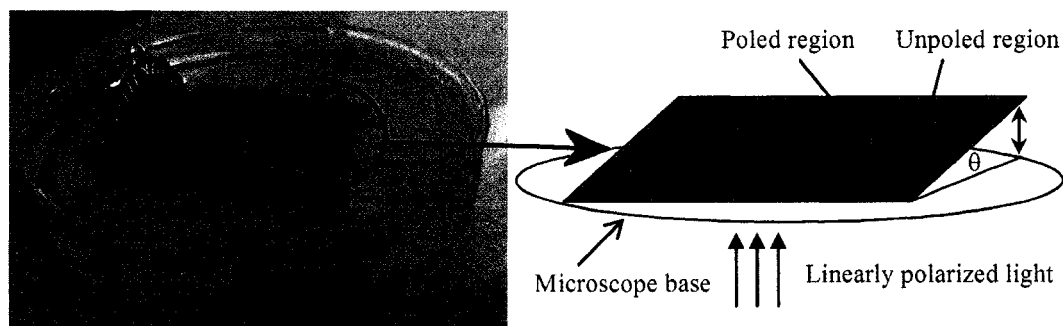


**Figure 3.7.** Left: Photograph of polymer sample attached to spindle stage submerged in mineral oil. Right: Illustration of experimental set-up showing direction of light propagation and axis of rotation relative to sample.

While the presence of an equivalence point substantiates the claim of chromophore reorientation during the poling process, the angle at which the equivalence point occurs provides a measure of the magnitude of

additional processes transforming chromophores into non-absorbing species. For samples in which  $\Delta A$  between the poled and un-poled domains is due solely to chromophore reorientation, the equivalence point should occur when the electric vector of the linearly polarized radiation is propagating through the sample at approximately  $35.3^\circ$  from the  $x$ -axis. Transformation of chromophores into non-absorbing species will shift the equivalence point to larger values eventually eliminating the equivalence point altogether.

For the semi-quantitative analysis of the equivalence point, the glass substrate of the thin films is glued to a spindle stage and the entire assembly is then submerged in a Pyrex crystallization dish filled with light, white, mineral oil ( $n_D^{20} = 1.4680$ ). The mineral oil provides a refractive index matching medium reducing interface reflections and refraction of the light through the thin film. A sheet polarizer with known orientation is placed between the glass dish and the light source of a field microscope providing a variable linearly polarized source of light for the examination of the film. For the determination of the equivalence point, the polarization of the electric vector of the light is orthogonal to the axis of rotation of the film; the  $p$ -polarization with respect to the inclined surface.

The films were then inclined in  $5^\circ$  increments until the absorbance of the poled and un-poled domains were equivalent to the eye. After recording this angle, the film was rotated about the spindle axis in the opposite direction until a similar equivalency was observed. The experiment was repeated in the original direction once more; the three recorded angles were then averaged yielding the equivalence point presented in 9. Table 3.1. For most of the films the equivalence point occurs at angles greater than  $35^\circ$ , the maximal value predicted by the model with zero chromophore transformation. This suggests a portion of the chromophores within the thin films possessing larger or non-existent equivalence points have been transformed into a non-absorbing species.

Determination of the equivalence point in several of these films was complicated by a change in hue in the poled region relative to the un-poled domain (9. Table 3.1). While the films were generally a dark forest green, the poled domain in several samples was distinctly bluer, approaching turquoise. Poling induced color shifts likely result from dye electrochromism and has been reported previously, though these effects typically lasted for only a few hours.<sup>122</sup> This effect is still apparent several months later in the samples described herein. Equivalence points for these

samples should be regarded cautiously as the differing hues dramatically increased the subjectivity of the measurement. More importantly, the different hues of the two domains supports the hypothesis that processes above and beyond chromophore reorientation are occurring in the doped films; the increased equivalence points indicate the proportion of chromophores involved in these alternative processes can be significant.

#### 3.3.2.2 *Absorption Spectroscopy*

Absorption spectra of the films measured as a function of tilt angle provide the absolute quantitative analysis of the linear optical properties of the poled thin films. Sample 31b5 was chosen for analysis as it was comparatively new, possessed a modest  $r_{33}$  coefficient, no hue shift in the poled region and was well cast. Unfortunately, the absorption maxima for this film ( $\lambda_{\text{abs}} > 750$  nm) lies beyond the limits of our microspectrophotometer (~400 nm to ~750 nm). The analysis was made at 625 nm, the edge of the absorption band of the principle electronic transition.



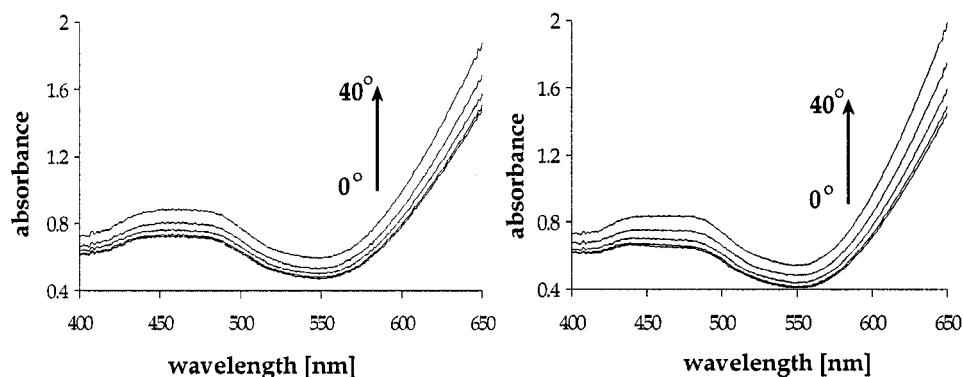


**Figure 3.8.** Absorption spectra of the un-poled domain (left) and the poled domain (right) of sample 31b5 measured at various angles of rotation from  $0^\circ$  to  $40^\circ$  in  $10^\circ$  increments.

The film and spindle stage were submerged in mineral oil to reduce refraction and interfering reflection effects. Measured absorbances were corrected for reflection and substrate effects empirically. The experiment was repeated using a piece of ITO/glass substrate without dye or polymer; the absorbance of the inclined reference was subtracted from the measured absorbances. Absorption spectra were measured at  $0^\circ$ ,  $10^\circ$ ,  $20^\circ$ ,  $30^\circ$  and  $40^\circ$  corresponding to internal angles of  $0^\circ$ ,  $8.6^\circ$ ,  $17^\circ$ ,  $25^\circ$ , and  $33^\circ$ , respectively. Three spectra were recorded and averaged for each rotation (Figure 3.8). Traces of the absorbance at 625 nm indicate that the equivalence point for

this film occurs at when the film is tilted to approximately  $28^\circ$  ( $22^\circ$  internal angle) (Figure 3.9).

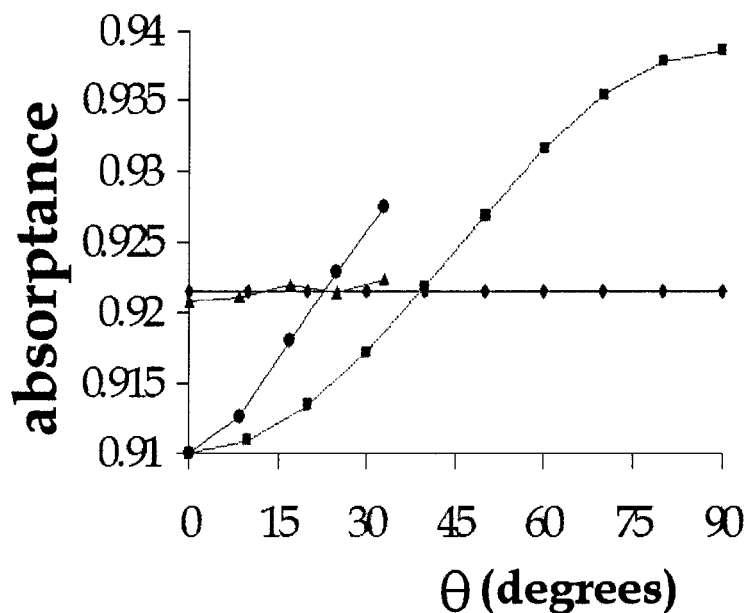


**Figure 3.9.** Traces of the experimentally determined absorbance of the poled (blue,  $\circ$ ) and un-poled (red,  $\Delta$ ) regions at 625 nm as a function of the angle between the electric vector and the  $x$ -axis within the film. The calculated absorbance for the un-poled region (black,  $\diamond$ ) assumes an isotropic distribution of chromophores. The calculated absorbance of the poled (green,  $\square$ ) domain assumes the differential absorbance between the two domains is entirely due to chromophore reorientation. The pathlength correction for refraction assumes  $n_{\text{oil}}=1.4680$  and  $n_{\text{polymer}}=1.59$ .

The results obtained using the absorbance approximation are nearly indistinguishable (Figure 3.10); the calculated equivalence point has shifted from approximately  $39^\circ$  in the absorptance model to  $35.2^\circ$  as determined in Section 3.1.3 .

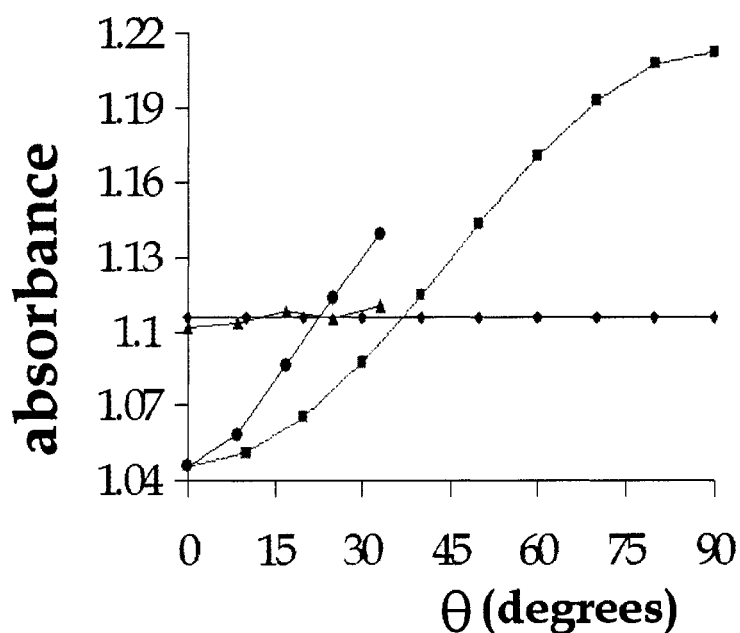


**Figure 3.10.** Traces of the experimentally determined absorbance of the poled (blue,  $\circ$ ) and un-poled (red,  $\Delta$ ) regions at 625 nm as a function of the angle between the electric vector and the  $x$ -axis within the film. The calculated absorbance for the un-poled region (black,  $\diamond$ ) assumes an isotropic distribution of chromophores. The calculated absorbance of the poled (green,  $\square$ ) domain assumes the differential absorbance between the two domains is entirely due to chromophore reorientation. The pathlength correction for refraction assumes  $n_{\text{oil}}=1.4680$  and  $n_{\text{polymer}}=1.59$ .

The shift of the equivalence point to larger values as the transformation parameter increases is illustrated in (Figure 3.4). To test this model a small area of the poled domain in sample Jen 3.3 was photo-bleached using the tungsten light source of a microscope; unpolarized conoscopic illumination was used to isotropically decompose the sample. When the sample was tilted the equivalence point of the unbleached poled domain was observed at 40-45°. The equivalence point for the photo-bleached region did not occur until 65° confirming the hypothesis that the disappearance of chromophores increases the equivalence point.

The poled region of the same film was then photo-bleached for 100 minutes using the illumination source of the microscope. The resulting traces of the absorbance at 625 nm demonstrate that the experimental equivalence point shifted from 22° to considerably greater than 40°.

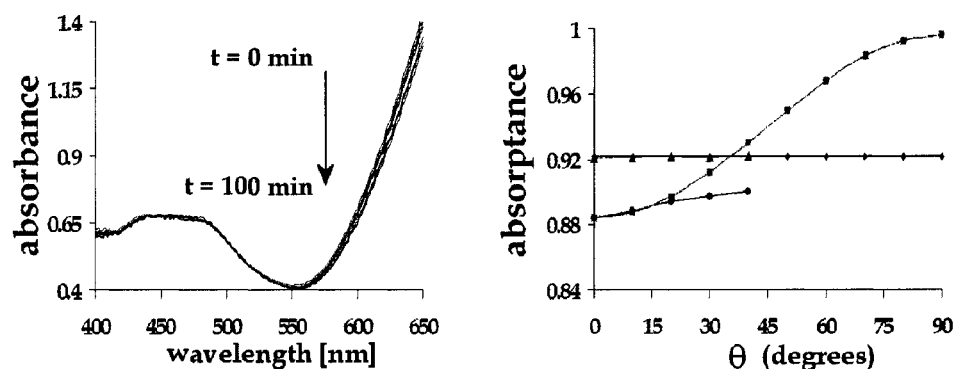


**Figure 3.11.** Traces of the experimentally determined absorbance of the photo-damaged poled (blue,  $\circ$ ) and un-poled (red,  $\Delta$ ) regions at 625 nm as a function of the angle between the electric vector and the  $x$ -axis within the film. The calculated absorbance for the un-poled region (black,  $\diamond$ ) assumes an isotropic distribution of chromophores. The calculated absorbance of the poled (green,  $\square$ ) domain assumes the differential absorbance between the two domains is entirely due to chromophore reorientation. The pathlength correction for refraction assumes  $n_{\text{oil}}=1.4680$  and  $n_{\text{polymer}}=1.59$ .

### 3.3.2.3 Discussion

Absorption spectroscopy and observations using a polarized field microscope confirm the presence of an equivalence point in a large number of poled polymer films. The tremendous variance and occasional absence of an equivalence point in these samples suggests that chromophore reorientation is not the sole process occurring during poling; chromophores are also being transformed into non-absorbing species.

The ability to increase equivalence points using photo-destructive techniques supports the notion that the extremely large poling fields are initiating electrochemical decomposition reactions within the film in addition to chromophore reorientation. These transformation reactions effectively reduce the absorbance of the poled domain relative to the unpoled region rendering the  $\Phi$  order parameter discussed earlier highly suspect.<sup>120</sup> Without further characterization, such as the measurement of the equivalence point, one cannot draw any truly meaningful associations between  $\Phi$  and non-linear optical properties of the thin films.

The observation of an equivalence point, as determined by absorption spectroscopy, considerably lower than predicted by a model assuming 100% chromophore reorientation was particularly confounding. The 100% chromophore reorientation model would give the earliest onset for the equivalence point, with chromophore transformation pushing the equivalence point to greater angles of rotation; the early equivalence point persists for both the absorptance and absorbance models.

One possibility for the rapid increase in absorbance might be related to the experimental setup; as the film is tilted, a small area of the unpoled domain (larger relative absorbance) is introduced into the sampling area of

the relatively small poled domain leading to an artificial increase in absorbance. This is unlikely as significant deviation from the model begins after the first rotation to  $10^\circ$ .

The most likely possibility for the anomalous data is the presence of a spectral shift in the poled domain relative to the un-poled region. The model for the poled region presumes that the spectra of the poled and un-poled regions are identical differing only in intensity. A shift in the spectrum of the poled region could have profound consequences for this or any linear dichroism model as analyses presume the transition energy to be invariant before and after poling; the differential intensity between the domains could arise solely from absorption energy shifts as opposed to chromophore reorientation. Despite this, examples of linear order parameters derived from spectra showing obvious and pronounced shifts between the poled and un-poled domains abound.<sup>123</sup> While a distinct color difference was not observed in the film used in the tilted absorbance measurements, considerable differences were observed in related films (Figure 3.6). Because the dichroism in these films is so slight ( $A_z - A_x \approx 0.03$ ), the slightest shift in the transition energy could profoundly impact the reliability of the measured equivalence point.

The poor agreement between the models and experimental data also precludes our ability to make a decision as to the correctness of our models. Does absorbance or absorbtance follow a  $\cos^2 \theta$  angular dependency? This question will be addressed in a model system in the following chapter.

The SHG properties of poled films decay as a function of time and temperature.<sup>124</sup> Research investigating the mechanism of SHG decay in polymer films has primarily consisted of the extensive characterization of the non-linear optical properties of the films. In the absence of investigations directly comparing the linear and non-linear optical properties of these films, researchers have concluded as recently as 2006 that the NLO properties decay because “the aligned chromophores will eventually revert to isotropic orientations.”<sup>125</sup>

While the reversion of chromophores to an isotropic distribution is sufficient for the elimination of the NLO properties of a film, it is not necessary. The medium need only revert to a centro-symmetric arrangement of chromophores to eliminate the SHG properties of the film.

The observation of persistent though vanishingly small linear dichroism in every film examined, even in films several years old, directly contradicts



the supposition that chromophores reorienting to isotropic or random distributions are responsible for the decay of the NLO properties of the films. Chromophores rearranging to form head to tail aggregate pairs would reduce or eliminate the SHG properties but would not necessarily result in a degradation or elimination of the observed linear dichroism. While such a scenario is highly speculative, it is consistent with the observed linear and non-linear optical properties.

While considerable progress towards the commercialization of organic electrooptic materials has been realized, an understanding of the structure and mechanics of these materials on the atomic and molecular scales remains inadequate. The somewhat haphazard collection of experiments discussed in this chapter was the consequence of the great difficulty we experienced in getting systematically prepared samples from colleagues that were necessary for a proper study of the linear optical properties. Any truly meaningful future investigation will require an abundance of identical thin films produced to exacting specifications and the subsequent comprehensive characterization of the linear and non-linear optical properties of these films. Such an accomplishment will provide a basis for

the rational design and development of the next generation of these materials.

## CHAPTER 4 - SORBITOL SPHERULITES

Sorbitol crystallizes as so-called spherulites from cooled melts. These polycrystalline formations have the optical symmetry of spheres. When the melt is pressed between glasses and examined in polarized light, the polycrystals behave like uniaxial disks with an infinite order optical axis in their centers. Almost 100 dyes that are soluble in molten sorbitol become oriented as the crystallization front passes through the melt so as to form highly linearly dichroic structures. The dyeing of spherulites is thus a very general method of solute alignment.

The first half of this chapter examines the linear optical properties of sorbitol spherulites containing the azo dye amaranth in detail so as to address a persistent confusion in the literature regarding the orientational dependence of linear dichroism. Some authors have taken transmittance as

having a cosine-square angular dependence while others have taken absorbance as having a cosine-square angular dependence. This issue often arises in cases involving thin film dichroism of multilayered samples that require many corrections to intensity data for samples in non-normal incidence. Plane sections of doped spherulites present all conceivable orientations of an electric dipole oscillator in spatially localized regions in normal incidence. As such, the samples described herein are ideally suited to resolving this confusion.

The linear birefringence and linear dichroism of sorbitol spherulites were examined using polarized light imaging techniques. The linear dichroism images were simulated only under the assumption that both absorbance and transmittance show a cosine-square angular dependence but with respect to *different angles*. Transmittance is connected to rotations of the fibrils about an axis parallel to the wave vector while absorbance is connected to rotations perpendicular to the wave vector. The spherulite example is offered because by self-assembly they present in one view all possible chromophore orientations thus obviating the confusion of sample reorientation and the substantial experimental difficulties that are

engendered in non-normal incidence. Thus, the principles of anisotropic absorption are given in a complete and intuitive fashion.

The latter part of this chapter describes our investigation of the non-linear optical properties of the dyed polycrystalline objects. It is clear from the strong linear dichroism of dyed spherulites that dyes are readily aligned within the chiral host. Would the interaction with the low symmetry crystallization growth front result in polar organization of the chromophores within the host? Unfortunately, second harmonic generation imaging of the dyed spherulites, a measure of the non-centrosymmetry of the material, showed no enhancement relative to undyed spherulites.

#### 4.1 Sorbitol

D-sorbitol, also known as glucitol and whose structure is shown in 1. Figure 4.1, is a commercially important sugar alcohol and is commonly used as a pharmaceutical excipient and food sweetener.<sup>126</sup> Sorbitol exhibits complex structural chemistry including three single crystal polymorphs ( $\alpha$ ,  $\beta$ ,  $\epsilon$ ), polycrystalline phases ( $\gamma$ , SM1, SM2) and solvate structures.<sup>127</sup>

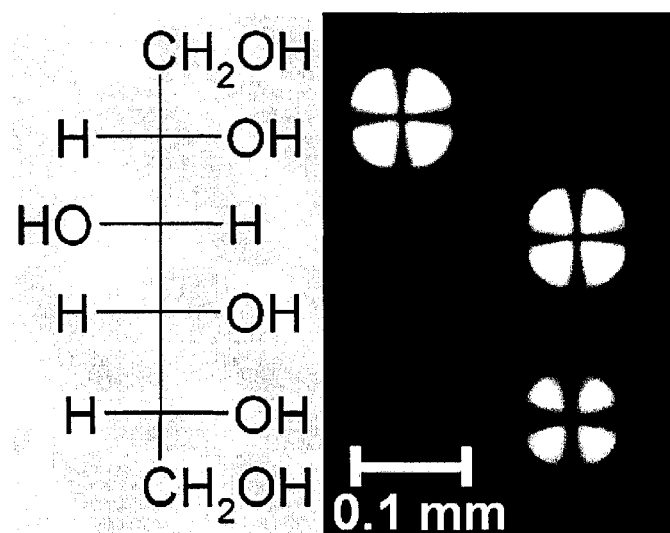


**Figure 4.1.** Chemical structure of D-sorbitol superimposed upon an optical micrograph of pure sorbitol spherulites viewed between crossed polarizers.

#### 4.2 Sorbitol Spherulites - Undyed

Yu recently described spherulites of sorbitol grown from films of the melt.<sup>128</sup> Melts are formed by heating the polycrystalline  $\gamma$  polymorph of D-sorbitol to 120 °C under vacuum, as Yu recommends, to remove air bubbles. A drop of melt is transferred with a glass rod to a microscope slide and compressed to 10-50  $\mu\text{m}$  thick beneath a glass cover slip. Spherulites spontaneously nucleate within 10-12 hours at room temperature and grow at a rate of 70  $\mu\text{m}/\text{hour}$ .

#### 4.2.1 Linear Optical Properties

Spherulites are not easily distinguished from the surrounding isotropic medium without polarizing elements. The symmetry of flattened spherulites grown between a slide and cover slip and viewed between cross polarizers was that of a circular disk displaying the 'maltese cross' characteristic of organized radial bodies (Figure 4.1). Such an optical symmetry is inconsistent with a single crystal.

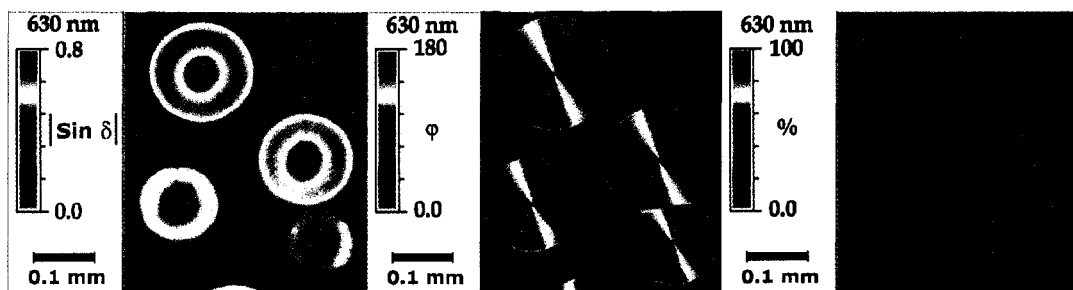


**Figure 4.2.** (Left to right) False-color images of  $\sin \delta$  (linear birefringence), orientation of the slow vibration direction ( $\phi$ ), and transmittance ( $T$ ) of sorbitol spherulites.

The rotating polarizer technique<sup>88</sup> was used to make images of retardance,  $\delta$ , in terms of the absolute value of the sign of this quantity, the slow vibration direction which is parallel to the spherulite radius, and the transmittance that does not distinguish the spherulites from the

surrounding melt (Figure 4.2). The spherulites, when fully grown, display linear birefringence characterized by first order phase shifts, punctuated by a core with near zero birefringence, a consequence of viewing a uniaxially symmetric body end-on.

AFM images of a spherulite grown on a coverslip, made by Dr. Ryan Sours, reveal two distinctly different surface topologies. The center of the spherulite in Figure 4.3 consists of numerous raised bumps that appear to emanate outwards along the radius of the spherulite. Higher resolution scans reveal that the bumps are faceted. This is possibly a consequence of recrystallization as the crystals must be opened from between pressed glasses in order to obtain the micrographs.



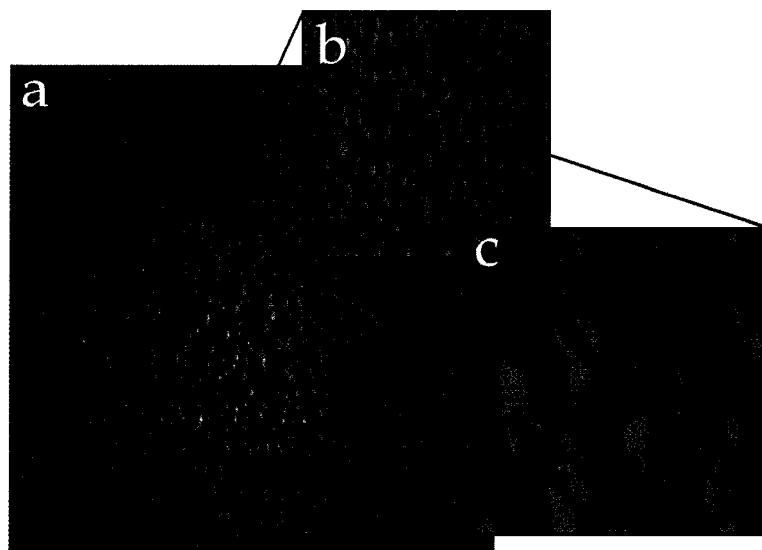


**Figure 4.3.** AFM images of a sorbitol spherulite showing the raised central core that contains geometric objects resembling crystal facets. Scan size: a.  $40 \times 40 \mu\text{m}^2$ , b.  $10 \times 10 \mu\text{m}^2$ , c.  $3 \times 3 \mu\text{m}^2$ .

AFM images of a second spherulite reveal a remarkably different texture; the polycrystalline bumps have been replaced with extremely fine interwoven fibrils that are at most 30 nm thick (Figure 4.4). Neither scan, however, seems to contain a sizeable disordered core around which radial bodies have assembled.

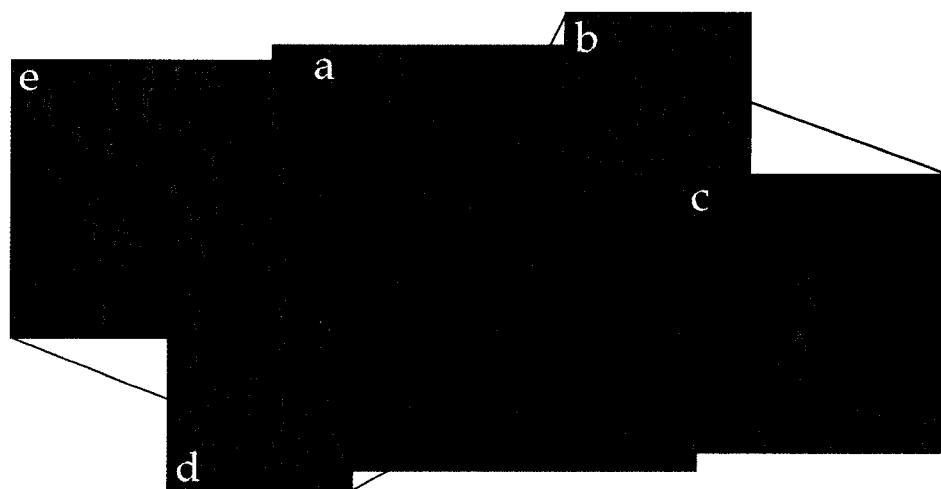


**Figure 4.4.** AFM images of a sorbitol spherulite showing the raised central core that contains geometric objects resembling crystal facets. Scan size: a.  $40 \times 40 \mu\text{m}^2$ , b.  $10 \times 10 \mu\text{m}^2$ , c.  $3 \times 3 \mu\text{m}^2$ .

Given the smooth optical texture observed in Figure 4.1 and Figure 4.2 it is likely that the spherulites grown between glass cover slips consist of fine fibers as opposed to the coarse faceted polycrystals, an observation that agrees with power x-ray diffraction patterns of sorbitol made by Yu (Figure 4.5).<sup>128</sup> The x-ray diffraction peaks of the spherulites are broader and weaker than the peaks of the starting  $\gamma$  polymorph. This is indicative of a reduction in crystallinity in the spherulite and is consistent with a structure of fine fibers. Therefore, even though the spherulites show a non-trivial

optical anisotropy, we can not say with certainty which polymorph they represent.

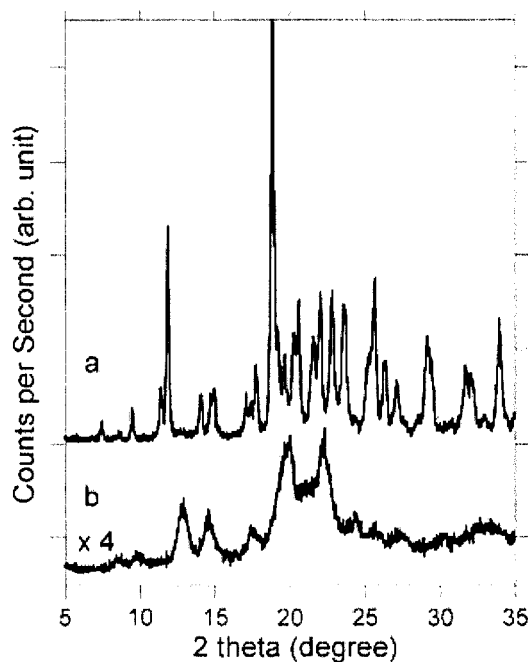


**Figure 4.5.** X-ray diffraction powder pattern of (a) the commercially available polycrystalline  $\gamma$  polymorph of sorbitol and (b) spherulites crystallized from a melt at 22 °C.<sup>128</sup>

#### 4.2.2 Non-linear Optical Properties

Second harmonic generation (SHG) as well as the linear electrooptic effect, both third rank tensorial properties, vanish in centrosymmetric

media. Therefore, SHG microscopy was used to assay the polarity of the host and dye substructures contained therein and the potential of dyed spherulites as electrooptic materials.

Pure sorbitol spherulites gave an SHG signal that increased quadratically with input power indicating that the spherulites are, as required by symmetry, acentric (Figure 4.6). The entire spherulite gives rise to an SHG signal well above the surrounding amorphous domain, though a polarization dependent anisotropy is evident. The signal is slightly larger when the polarization of the incident linearly polarized radiation is parallel to the radius of the spherulite; the refractive index of this direction being slightly larger than perpendicular to the radius.

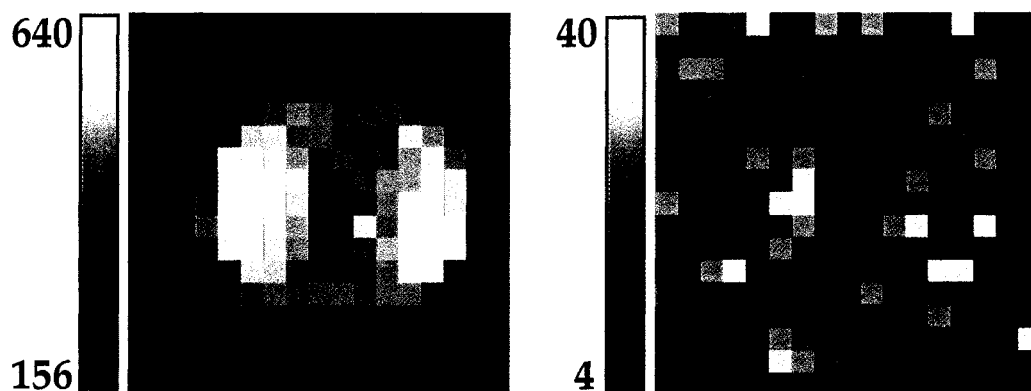


**Figure 4.6.** Left: SHG intensity (counts) of a  $80\ \mu\text{m} \times 80\ \mu\text{m}$  scan ( $5\ \mu\text{m}$  step size) of a pure sorbitol spherulite using linearly polarized

(horizontal) 800 nm, 120 fs laser pulses at 10.0 mW (100 ms integration). Right: Identical scan using 830 nm excitation.

### 4.3 Dyed Sorbitol Spherulites

Many dyes - laser dyes, textile dyes, biological stains, NLO chromophores etc. - are soluble in molten sorbitol. When the spherulite crystallization front passes through the melt, the dyes are invariably oriented giving rise to highly dichroic disks. The generality of sorbitol spherulites as a dye host rivals that of the polymer and glass counterparts that have been used in the development of EO materials. Unlike dyed single crystals, sorbitol spherulites can accommodate dye concentrations of 5 wt. %.

#### *4.3.1 Angular Dependence of Linear Dichroism*

Recently, Gregoriou and coworkers claimed to have settled “once and for all, the confusion that exists in the spectroscopic literature” regarding the angular dependence of absorbance and transmittance with respect to the incident polarized light.<sup>110</sup> At issue was whether transmittance ( $T$ ) or

absorbance ( $A$ ) of uniaxial absorbing bodies followed a  $\cos^2\theta$  angular dependence, that is whether Equation 1 or Equation 2 was valid.

$$A(\theta) = A_{\max} \cos^2(\theta) + A_{\min} \sin^2(\theta) \quad (1)$$

$$T(\theta) = T_{\min} \cos^2(\theta) + T_{\max} \sin^2(\theta) \quad (2)$$

We were surprised to discover that such an ostensibly fundamental question was a source of confusion, especially given authoritative monographs on the subject of dichroism.<sup>1</sup> Having ourselves measured the linear dichroism of many mixed crystals,<sup>18</sup> we resolved to first ascertain the nature of this confusion and how it arose, and to resolve the question either in favor of (1) or (2). As we will discover, the resolution is not as simple as a proper choice.

The question of the angular dependence of linear dichroism often arises in the analysis thin films of membranes,<sup>112</sup> poled polymers,<sup>123</sup> and liquid crystals.<sup>129</sup> The aforementioned group, in the analysis of a thin film of a nematic liquid crystal, came down squarely in favor of Eq. (2), citing the Law of Malus,<sup>130</sup> the first quantitative relationship involving polarized light which states that  $I/I_0 = T = \cos^2\theta$ , where  $\theta$  is the angle of incidence between

the plane of linearly polarized light and the preferred direction of a linear analyzer;  $T$  is the transmittance.

In making measurements of multi-layers it is critical to properly evaluate artifacts present in optical measurements made at non-normal incidence including the following: path length corrections due to Snell's law, to account for the fact that the extraordinary ray does not conform to Snell's law<sup>115</sup>, for Fresnel reflections<sup>116</sup>, for multiple reflections<sup>119</sup>, for the increasing area of illumination at increasing angles<sup>118</sup>, and for the conicity of the light pencil<sup>117</sup>. Furthermore, these corrections require precise knowledge of the real and imaginary parts of the absolute refractive index of the material and substrate. The paper by Gregoriou and coworkers<sup>110</sup> does not address the treatment of their data in non-normal incidence.

In order to settle the question between Eqs. (1) and (2) by means of experiment, we sought a system that would obviate the necessity of the corrections listed above. An ideal system for this purpose, we recognized, would be a thin section of a sphere in which chromophores were arranged uniaxially along the radii of the sphere, displaying all possible orientations in spatially localized regions with respect to a fix polarizer. We wanted to measure each and every orientation in normal incidence so as to obviate

moving samples, moving components in the optical path, and intensity corrections. We show that the study of the linear dichroism of dyed spherulites beautifully illustrate the hard won principles of crystal optics whose improper application have caused confusion with respect to the angular dependence of transmittance and absorbance.

#### *4.3.1.1 Linear Optical Properties of Amaranth Spherulites*

The azo dye, amaranth (acid red 27, C.I.# 16185) was chosen for this study because it is photostable, highly soluble in sorbitol, and produces spherulites with strong linear dichroism. Dyed spherulites containing 0.01 to 1.0 wt. % amaranth were prepared by the addition of a suitable mass of dye to 5.0 g of sorbitol ( $\gamma$  polymorph). Mixed crystals were grown from the melt as described above.



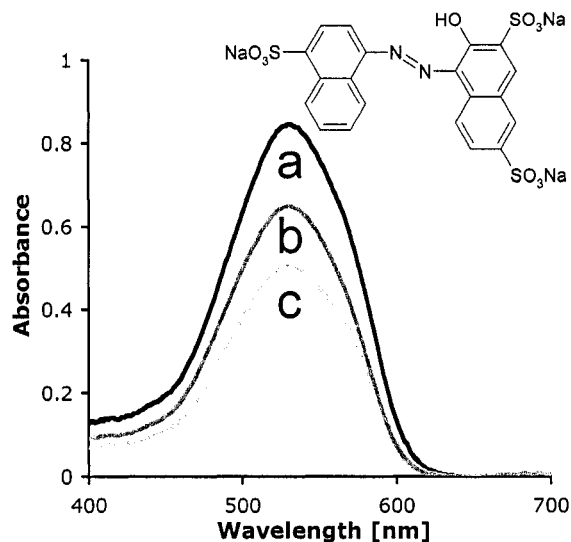


**Figure 4.7.** Absorption spectra of the isotropic melt (b), the radial direction (a), and tangential direction (c) of the spherulitic domain of sorbitol containing 0.5 wt. % amaranth. The chemical structure of the dye is superimposed upon the spectra.

The absorption maximum ( $\lambda_{\text{max}} = 532 \text{ nm}$ ) is identical for the melt and the spherulitic domain for all dye concentrations examined (Figure 4.7). Absorbance measurements and automated imaging related to the linear dichroism<sup>99</sup> confirm that the radial vibration direction is the strongest absorbing direction; the dye is preferentially aligned in the radial direction of the spherulite (Figure 4.8).

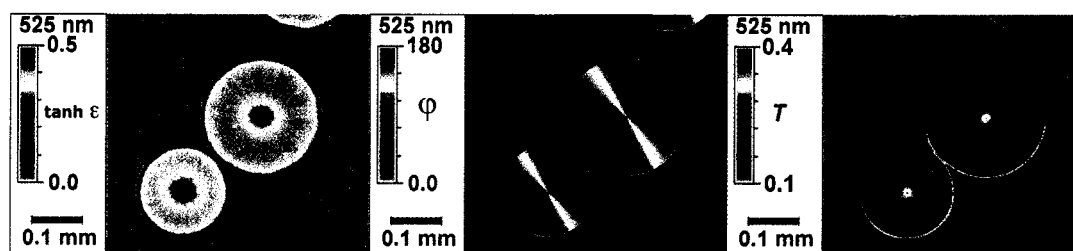


**Figure 4.8.** (Left to right) False-color micrographs of  $\tanh \varepsilon$  (linear dichroism), orientation of the strongest absorbing direction ( $\varphi$ ), and transmittance ( $T$ ) of sorbitol spherulites containing 0.5 wt. % amaranth.

#### 4.3.1.2 Not All Rotations are the Same

The plane polar coordinate of a given oscillator organized in a section of a spherulite can be defined by two rotations,  $\theta$  and  $\varphi$ , that describe, respectively, the azimuth of the oscillator in the plane section and the inclination of the oscillator with respect to the unique axis. A  $\theta$  rotation is parallel to the wave vector  $k$ ; a  $\varphi$  rotation is perpendicular to  $k$ .

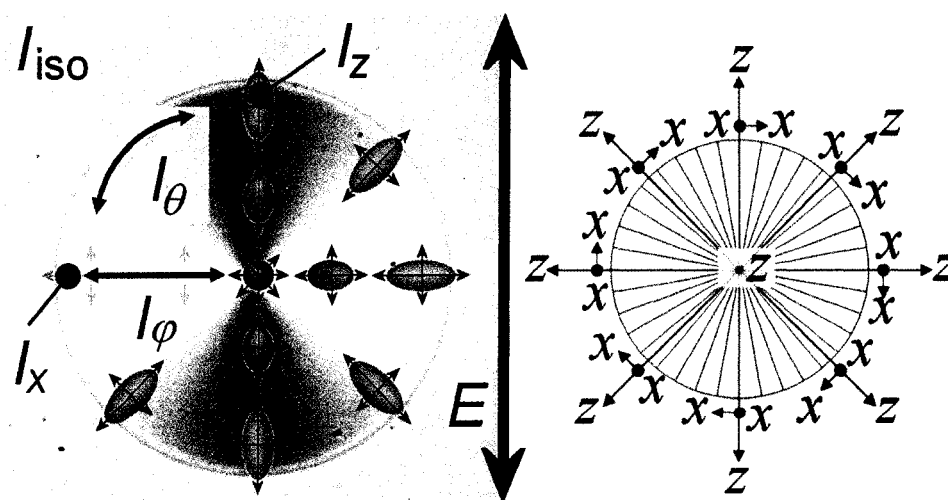


**Figure 4.9.** Left: Idealized index/absorption ellipsoids superimposed upon a contrast-enhanced polarized light micrograph of a spherulite containing 0.75 wt. % amaranth. The arrows on the surface indicate the orientation of the vibration directions in the specified domain; the lengths of the arrows qualitatively represent the magnitude of the absorption coefficient of the vibration direction. The plane of polarization of the electric vector of the incident radiation is indicated by the heavy vertical double arrow. The labels indicate the directions and rotations of the ellipsoid that are measured simultaneously. Right: Specified directions in an idealized spherulite.

Intensity images of spherulites,  $I$ , containing amaranth were generated by photographing the sample with a CCD camera through a microscope using monochromatic (525 nm) linearly polarized radiation from an LED array as the illumination source (Figure 4.9). In addition to simultaneously imaging all possible orientations of the absorbance ellipsoid within the anisotropic

domain, these images also provide the transmitted intensity of the melt which contains an isotropic distribution of chromophores. The isotropic domain is a valuable reference not generally available in other systems, and provides a convenient assay for the optical homogeneity of the film while ensuring the sample is a uniform thickness.

A sample of comparable thickness containing an undyed sorbitol melt provides the initial intensity image,  $I_0$ . Pixel by pixel division of the two images,  $I/I_0$ , yields an image of the transmittance of the dyed spherulite (Figure 4.10).

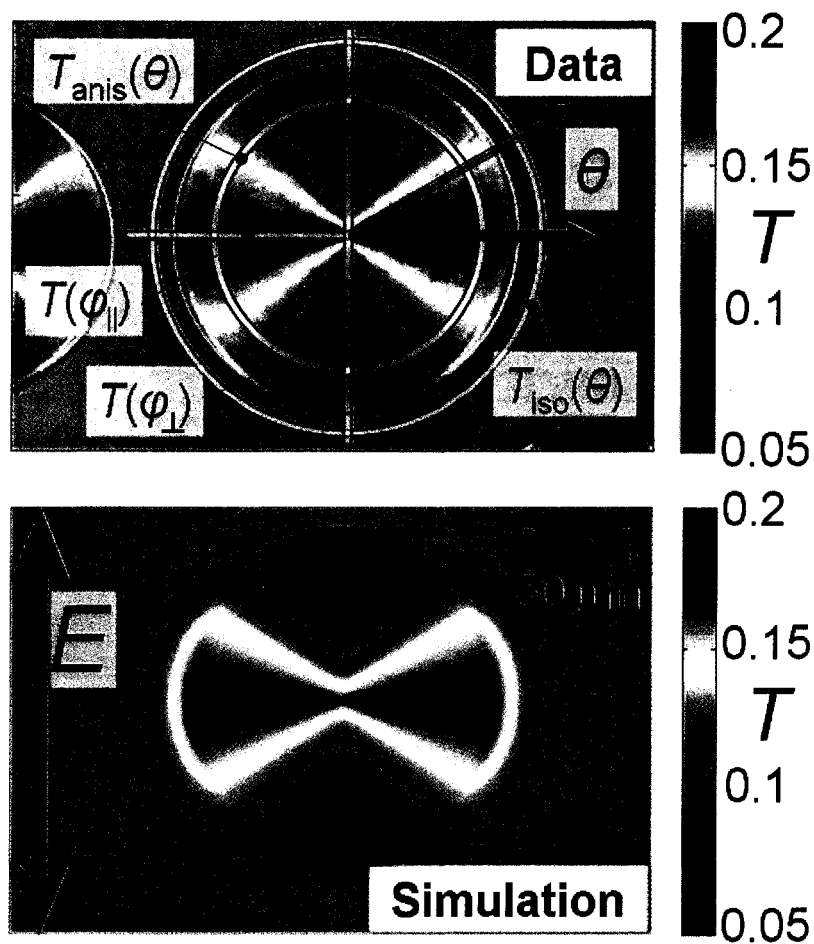


**Figure 4.10.** Polarized transmittance image of a spherulite containing 0.75 wt. % amaranth.  $\theta$  rotations of the absorption ellipsoid are measured by analyzing rings a distance,  $r$ , from the center of the spherulite. Two unique rotations,  $\varphi_{\perp}$  and  $\varphi_{\parallel}$ , are measured by analyzing straight lines that contain the maxima and minima of the  $\theta$  rotation function. Lower: Simulated polarized transmission image. The large black arrow indicates the polarization state of the incident radiation for both images.

#### 4.3.1.2.1 Theta Rotations

Typically, a  $\theta$  rotation involves the rotation of either a polarizer or the sample. In a spherulite, however, the radial organization effectively rotates any domain a distance,  $r$ , from the center by  $2\pi$ .

The radial variation of the transmittance inside and outside of the spherulite is obtained by analyzing concentric rings (Figure 4.10). For each sample, transmittance is converted to absorbance and both sets of data are then fit to a  $\cos^2\theta$  function bounded by the minima and maxima (Figure 4.11).

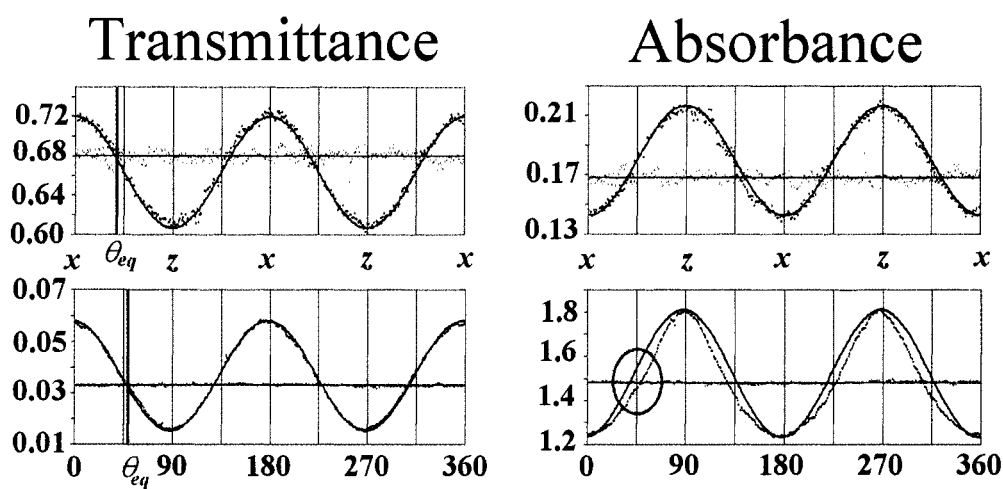


**Figure 4.11.** Transmittance (left column) and the corresponding absorption (right column) plots from spherulites that are optically thin (upper) and optically thick (lower). The solid pink line represents the average value of the isotropic data (pink dots).

The solid blue line is a  $\cos^2\theta$  fit of the data from the anisotropic domain (black dots). The vertical red line in the transmittance curves indicates the measured equivalence point. In the optically thick sample  $\theta_{eq}$  has shifted towards  $z$  ( $90^\circ$  and  $270^\circ$ ). The discrepancy between the absorbance  $\cos^2\theta$  model and the measured equivalence point is circled in red.

#### 4.3.1.2.2 Phi Rotations

Typically, a  $\varphi$  rotation in a thin dichroic sample requires tilting about an axis perpendicular to the wave vector,  $k$ . For measurements in single crystals, each unique  $\varphi$  rotation requires the preparation of new plane-parallel cut and polished crystal slices. In a spherulite,  $\varphi$  rotations are realized by moving from the center where the  $z$ -direction of the ellipse is parallel to  $k$  to the edge of the spherulite where  $z$  is perpendicular to  $k$ . Following this trajectory, the ellipsoid effectively rotates about an axis perpendicular to  $k$  and perpendicular to a radius.

Two ‘pure’  $\varphi$ -rotations are present in linearly polarized transmittance images of a spherulite. Both rotation axes are perpendicular to  $k$ ; the  $\varphi_\perp$  rotation axis is perpendicular the plane of polarization.  $\varphi_\parallel$  is parallel to the plane of polarization (Figure 4.12).

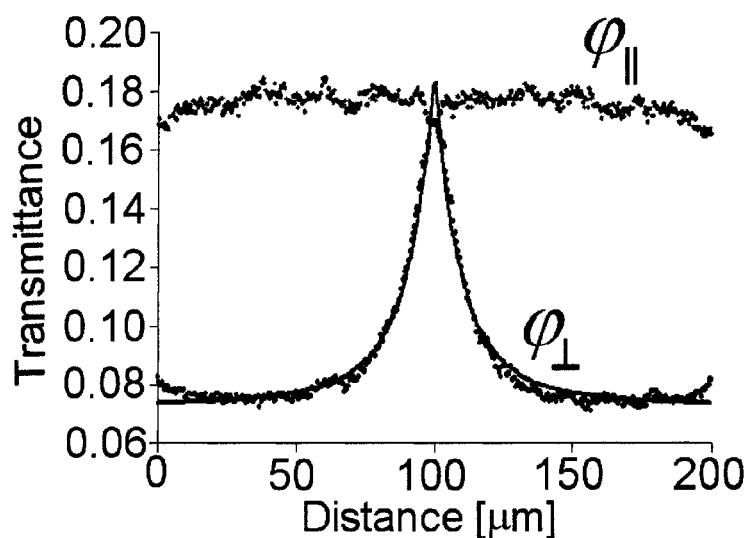


**Figure 4.12.** Plot of the transmittance for  $\varphi_{\perp}$  (black dots) and  $\varphi_{\parallel}$  (pink dots) rotations in a spherulite containing 0.75 wt. % amaranth. The solid blue line is a fit to equation (6).

#### 4.3.1.3 Discussion

Standard works express the probability for a spectroscopic transition in terms of the square of the projection of the transition moment describing that excitation onto the electric field vector of the incoming light.<sup>1</sup> However, the electric field vibrations in a dielectric anisotropic medium are constrained by the optical indicatrix of the medium, and thus the quantity  $|M \cdot E|^2$  where  $M$  is the transition moment and  $E$  is the electric field of the incident light, can not be assessed directly by arbitrary rotations of the



sample. While this is known commonly in crystal optics, it is undoubtedly the source of the confusion cited by Gregoriou in coworkers.<sup>110</sup>

In precisely the same manner that the index ellipsoid describes the refractive indices for any  $k$ , the absorption ellipsoid describes a material's absorption coefficients. The absorption ellipsoid is characterized by the magnitude of the coefficients along three orthogonal principle directions,  $x$ ,  $y$ , and  $z$ . In a uniaxial system in which  $x$  and  $y$  are degenerate, only two principle directions,  $x$  and  $z$ , exist. Furthermore, symmetry requires these directions be coincident with the principle directions of the index ellipsoid.

At low optical densities, (1) and (2) describe the transmitted intensity of light propagating through an absorbing medium equally well with respect to a  $\theta$  rotation (Figure 4.11). As the optical density is increased, the accuracy of two models diverge. Transmittance alone follows a  $\cos^2 \theta$  dependence, not absorbance. This supports the supposition that (2), not (1) describes the optical properties of a sample following a  $\theta$  rotation.<sup>131</sup> Analysis of a subtle and generally inaccessible feature, the equivalence point, further supports this determination.

If chromophores are being preferentially aligned along  $z$ , the absorbance will increase along this direction and decrease along  $x$ . The absorbance for an isotropic distribution will be intermediate these two values. Therefore, a  $\theta$  rotation must exist that will result in the anisotropic domain having an optical density equivalent to that of the isotropic domain, the equivalence point,  $\theta_{eq}$ , or when

$$A^{iso}(\theta_{eq}) = A^{anis}(\theta_{eq}); \quad T^{iso}(\theta_{eq}) = T^{anis}(\theta_{eq})$$

Presuming  $z$  is the unique axis, the extinction coefficients in a uniaxial anisotropic domain are related to the isotropic extinction coefficient by

$$\epsilon^{iso} = \frac{2\epsilon_x^{anis} + \epsilon_z^{anis}}{3} \quad (3)$$

Because pathlength and concentration are constant in the spherulite samples, (3) becomes

$$A^{iso} = \frac{2A_x^{anis} + A_z^{anis}}{3} \quad (4)$$

As derived in section 3.1.3, (1) predicts an invariant equivalence point occurring when the plane of polarization is rotated  $35.3^\circ$  -the complimentary angle of the magic angle  $54.7^\circ$ - from  $x$  towards the  $z$ -axis.

The expression for the equivalence point using (2) becomes

$$\theta_{eq} = \arccos \sqrt{\frac{((T_x^{anis})^2 \times T_z^{anis})^{\frac{1}{3}} - T_z^{anis}}{T_x^{anis} - T_z^{anis}}}$$

While this expression is cumbersome, it predicts that  $\theta_{eq}$  will increase from  $35.3^\circ$  as either the optical density or anisotropy increases (Figure 3.3).

In the optically thin sample the equivalence point was  $37^\circ$  from  $x$ . The transmittance model predicts  $36.4^\circ$ ; the absorbance model invariably predicts  $35.3^\circ$ . In the optically thick sample, the equivalence point was  $46^\circ$  from  $x$ . The calculated equivalence points were  $44.2^\circ$  and  $35.3^\circ$  for the transmittance and absorbance models, respectively.

Again, it is not surprising that the transmittance model correctly describes  $\theta$  rotations. These rotations do not change the projection of the index ellipsoid with respect to the wave vector of the light. In a  $\theta$  rotation the absorption coefficients of the two vibration directions remain constant; the only thing that changes is the *intensity* of the light that is projected onto the eigenmodes. That is:  $T(\theta) = T_{max}\cos^2(\theta) + T_{min}\sin^2(\theta)$  where  $T_{max}$  and  $T_{min}$  are transmitted intensities when the incident light is polarized in the plane

of an eigenmode of the medium. This is a statement of the Law of Malus.<sup>130</sup>

Thus in terms of absorbance and absorption coefficients

$$T(\theta) = 10^{-A_x} \cos^2 \theta + 10^{-A_z} \sin^2 \theta$$

$$T(\theta) = 10^{-\varepsilon_x \cdot c \cdot l} \cos^2 \theta + 10^{-\varepsilon_z \cdot c \cdot l} \sin^2 \theta \quad (5)$$

Phi rotations to do, however, change the cross-section of the index ellipsoid with respect to the wave vector of the light. In a spherulite, any  $\varphi$ -rotation will change the absorption coefficient of the eigen-mode parallel to the radial direction; the tangential eigen mode is unperturbed. The radial absorption coefficient has a  $\cos^2 \varphi$  dependence given by

$$\varepsilon(\varphi) = \varepsilon_z \cos^2 \varphi + \varepsilon_x \sin^2 \varphi$$

The transmittance for a  $\varphi$ -rotation is expressed as

$$T(\varphi) = 10^{-((\varepsilon_z \cos^2 \varphi + \varepsilon_x \sin^2 \varphi) \cdot c \cdot l)}$$

and can be rearranged to give

$$T(\varphi) = 10^{-((\varepsilon_x + (\varepsilon_z - \varepsilon_x) \cos^2 \varphi) \cdot c \cdot l)}$$

$$T(\varphi) = 10^{-((\varepsilon_z + (\Delta\varepsilon) \cos^2 \varphi) \cdot c \cdot l)}$$

$\Phi$  effectively describes the pitch of the ellipsoid, the angle between the spherulite z-axis and the plane of the spherulite, and is related to  $r$ , the distance from the center of spherulite by

$$\tan \varphi = \frac{l}{r}$$

where  $l$  is the thickness of the sorbitol layer.

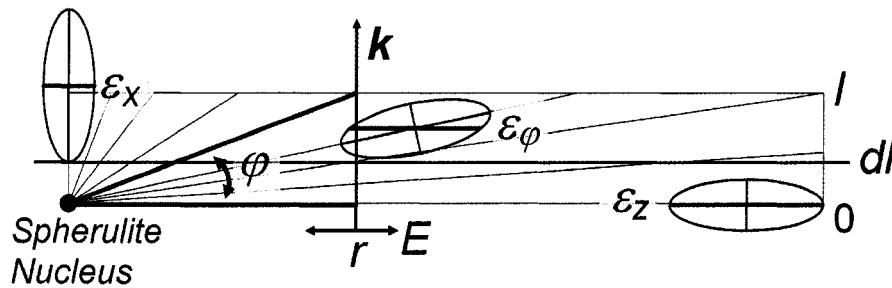


**Figure 4.13.** Schematic representation of a view parallel to a  $\varphi$  rotation axis for a sample of thickness,  $l$ . The cross-section of the ellipse for various rotations is indicated. An infinitesimally thin slice,  $dl$ , is indicated by the blue line. Light propagating through the sample a distance,  $r$ , from the center will encounter a continuous distribution of ellipsoids between  $\varphi$  and  $0^\circ$ .

However, at any point  $r$  there will be a continuous distribution of ellipsoids from  $\varphi$  to  $0^\circ$ . Correctly modeling the transmittance requires

integrating infinitesimally thin slices,  $dl$ , over the total sample thickness,  $l$ .

The transmittance becomes

$$T(\varphi) = 10^{-\int_0^l [\varepsilon_x + (\Delta\varepsilon)\cos^2(\varphi)] \cdot c \cdot dl}$$

$$T(r) = 10^{-\int_0^l [\varepsilon_x + (\Delta\varepsilon)\cos^2(\tan^{-1}(\frac{l}{r}))] \cdot c \cdot dl}$$

$$T(r) = 10^{-\varepsilon_x \cdot c \cdot l + (-\Delta\varepsilon \cdot c \cdot r \cdot \tan^{-1}(\frac{l}{r}))}$$

This expression can of course be converted to the natural logarithmic expression

$$T(r) = e^{-\alpha_x \cdot l + (-\Delta\alpha \cdot r \cdot \tan^{-1}(\frac{l}{r}))} \quad (6)$$

where  $\alpha \approx 2.303 \cdot \varepsilon \cdot c$  and has the units  $\text{cm}^{-1}$ . Figure 4.12 shows the fit of this integrated equation to the data for the  $\varphi_{\perp}$  rotation.

The transmittance for any point on a spherulite analyzed using linearly polarized radiation can thus be completely described by combining expressions (5) and (6) derived from the analysis of  $\theta$  and  $\varphi$  rotations:

$$T(\theta, \varphi) = e^{-\alpha(\varphi_{\parallel})} \cdot \cos^2 \theta + e^{-\alpha(\varphi_{\perp})} \cdot \sin^2 \theta$$

$$T(\theta, \varphi) = e^{-\alpha_x \cdot l} \cdot \cos^2 \theta + e^{-\int_0^l [\alpha_x + (\Delta\alpha)\cos^2(\varphi)] \cdot dl} \cdot \sin^2 \theta$$

Expressed in terms of  $r$

$$T(\theta, r) = e^{-\alpha_x \cdot l} \cdot \cos^2 \theta + e^{-\alpha_x \cdot l + (-\Delta\alpha \cdot r \cdot \tan^{-1}(\frac{l}{r}))} \cdot \sin^2 \theta$$

A Mueller matrix utilizing the above expression to describe the diattenuation in the sample was constructed in order to generate a simulated image of a dyed spherulite (see experimental for details). The synthesis of the image takes into account diattenuation, retardance, and growth; the details are described in the experimental section of this chapter. Figure 4.10 shows the resulting image which is in excellent agreement with the observed polarized transmittance image.

Our results represent the first simultaneous complete characterization of all polarizations in a dyed uniaxial system that includes an isotropic reference at constant path length requiring no moving parts or inclined surfaces. Our conclusions herein were derived recently by Scaife and Vij from first principles considerations of the propagation of electromagnetic fields in dielectric media.<sup>132</sup> Our experiments confirm their prediction in a remarkably direct, intuitive, and experimentally unassailable fashion.

### 4.3.2 Electro-optic Sorbitol Spherulites

Because of its notoriety as an NLO chromophore, we focused on DAST as a sorbitol spherulite guest. Crystallizing in the polar space group  $C_c$ ,<sup>133</sup> *trans*-4-[4-(dimethylamino)styryl]-1-methylpyridinium *p*-toluenesulfonate (DAST) single crystals remain one of most studied organic EO crystals to date.<sup>134</sup>

#### 4.3.2.1 Linear Optical Properties of DAST Spherulites

DAST is orange ( $\lambda_{\text{abs}} = 480$  nm) in MeOH and becomes deep red ( $\lambda_{\text{abs}} = 542$  nm) upon crystallization. Up to 5 wt. % of DAST dissolves in molten sorbitol. Amorphous sorbitol containing DAST is orange ( $\lambda_{\text{abs}} = 485$  nm,  $\lambda_{\text{em}} = 563$  nm). The dyed spherulites, however, are red ( $\lambda_{\text{abs}} = 515$  nm,  $\lambda_{\text{em}} = 588$  nm) and highly dichroic (dichroic ratio of 3; see Figure 4.14).<sup>135,136</sup>



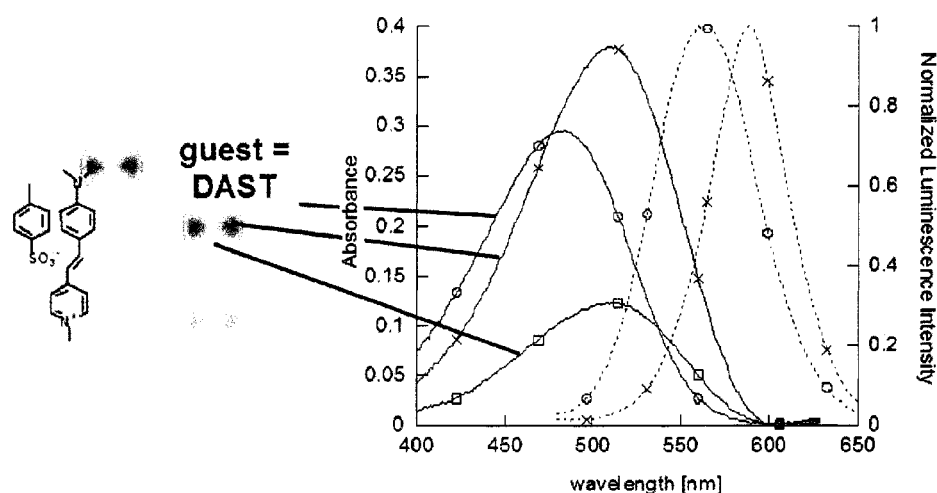


**Figure 4.14.** Left: Structure of the guest superimposed upon optical micrographs of sorbitol spherulites containing DAST viewed with linearly polarized light (horizontal). The spectral shift between the melt and spherulite is evident. Right: Absorbance spectra of the melt and of radial crystallites parallel and perpendicular to the horizontal polarization. The strong linear dichroism is apparent.

Absorbance measurements and automated imaging of the linear dichroism confirm that the radial vibration direction is also the strongest absorbing direction; on average the EDTM, which is parallel to the long axis of DAST, is oriented  $30^\circ$  away from the radius.

#### 4.3.2.2 Non-linear Optical Properties

As expected, the intensity of up-conversion luminescence arising from two-photon absorption by DAST within the spherulite was highly

anisotropic; bright lobes appearing when the polarization of the laser was parallel to the radius of the spherulite. Unlike the SHG signal obtained from pure sorbitol in which the entire spherulite was more intense than the surrounding amorphous domain, the signal when the laser polarization was perpendicular to the radius lies well below the amorphous domain. In these dark lobes, DAST has been effectively rotated into a non-absorbing and thus a non-luminescing direction; the randomly oriented molecules in the amorphous domain therefore have a larger absorption cross section relative to the dark lobe and thus more intense luminescence.

The SHG signal for DAST dyed spherulites was confounding. At DAST concentrations below 0.3 wt. %, the SHG signal resembled that of the up-conversion luminescence; bright and dark lobes where the intensity of the dark lobe was less than the surrounding amorphous region. When tuned to 830 nm, the signal, while maintaining an identical polarization anisotropy, was only slightly diminished; the reduction in intensity being nearly equivalent to that of the SHG intensity of a pure sorbitol spherulite.

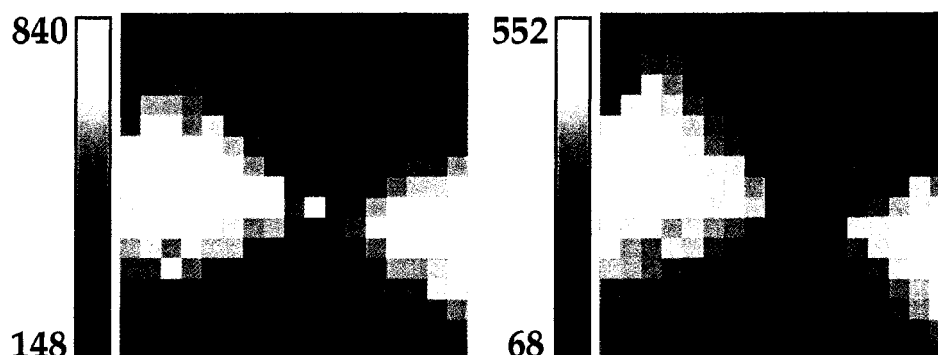


**Figure 4.15.** Left: SHG intensity (counts) of a  $80\text{ }\mu\text{m} \times 80\text{ }\mu\text{m}$  scan ( $5\text{ }\mu\text{m}$  step size) of a sorbitol spherulite containing 0.1 wt. % DAST using linearly polarized (horizontal) 800 nm, 120 fs laser pulses at 5.0 mW (100 ms integration). Right: Identical scan using 830 nm excitation.

At DAST concentrations of 0.3 wt. % the SHG intensity of the spherulite was indistinguishable from the background. While the average intensity of the SHG image was 2100 counts, several bright spots with intensities in excess of  $2.0 \times 10^4$  were observed. These are likely the result of SHG active microcrystallites of DAST forming within the sample. While the presence of these crystallites could not be confirmed using a polarized light microscope, a uniform distribution of randomly oriented DAST microcrystallites would result in a featureless SHG image.

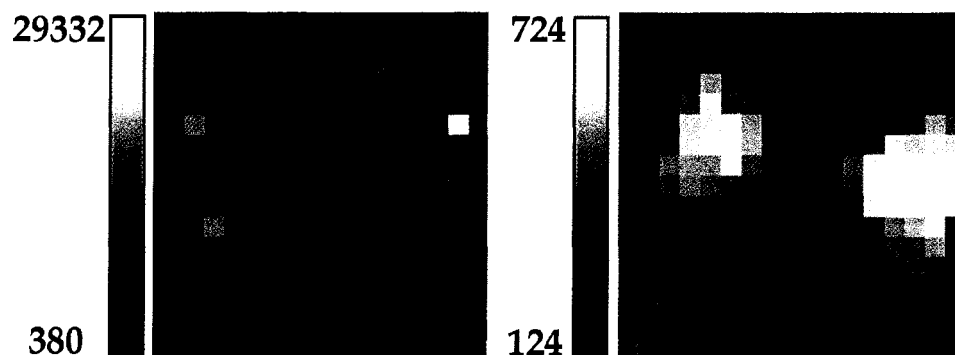


**Figure 4.16.** Left: SHG intensity (counts) of a  $80\text{ }\mu\text{m} \times 80\text{ }\mu\text{m}$  scan ( $5\text{ }\mu\text{m}$  step size) of a sorbitol spherulite containing 0.3 wt. % DAST using linearly polarized (horizontal) 800 nm, 120 fs laser pulses at 5.0 mW (100 ms integration). Right: Identical scan using 830 nm excitation.

At 0.4 wt. % the signal for the entire spherulite domain was well above the background intensity. In stark contrast to the SHG of the pure spherulite and the up-conversion luminescence of the dyed spherulite, the signal displayed no polarization anisotropy.

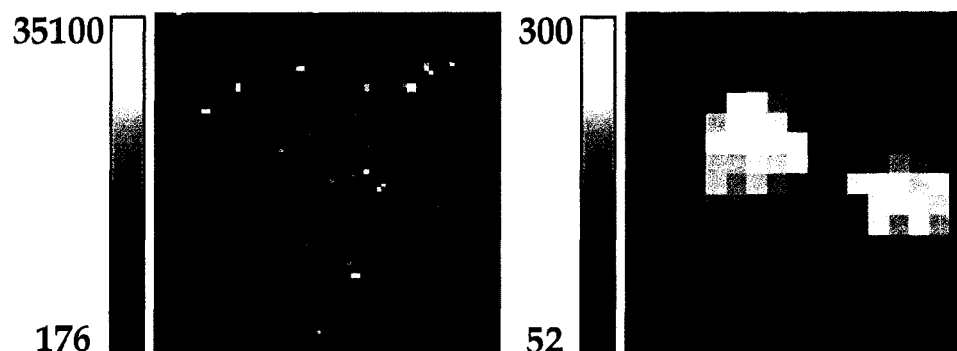


**Figure 4.17.** Left: SHG intensity (counts) of a  $80\ \mu\text{m} \times 80\ \mu\text{m}$  scan ( $1\ \mu\text{m}$  step size) of a sorbitol spherulite containing 0.4 wt. % DAST using linearly polarized (horizontal) 800 nm, 120 fs laser pulses at 2.5 mW (100 ms integration). Right: Identical scan using 830 nm excitation and a  $5\ \mu\text{m}$  step size.

Up to 5 wt. % DAST is soluble in molten sorbitol at  $100\ ^\circ\text{C}$ ; however, dye crystallites are clearly visible in the cooled melts of sorbitol containing 0.5 wt. % DAST. While microcrystallites were not observed in melts containing 0.4 wt % DAST, it is not unreasonable to suspect micro-crystallite formation at dye concentrations so close to the limit of solubility.

If DAST was being oriented in a polar manner within the spherulite matrix, the corresponding SHG image should exhibit pronounced polarization anisotropy; an enhancement of the signal observed in pure sorbitol. While the intensity of the SHG signal was enhanced, the signal was effectively depolarized within the spherulite. This depolarization would

occur if the spherulite contained randomly oriented DAST microcrystallites. While numerous 'SHG hotspots' exist within the amorphous domain of the 0.4 wt. % sample, it is clear that the preponderance of SHG intensity is contained within the spherulite. Why then would DAST preferentially crystallize within the spherulite domain?

It is entirely possible that as sorbitol crystallizes into spherulites, rather than incorporating DAST into the lattice, the dye is simply 'pushed' into the voids between the growing radial fibers. This 'push' could certainly result in distribution of chromophore orientations biased towards the radial direction resulting in the pronounced linear dichroism. Furthermore, a non-specific interaction with the dye molecule would result in a non-polar distribution supported by the lack of SHG enhancement outside of DAST crystallization. Being so close the saturation point of DAST within sorbitol, the excluded volume of the sorbitol fibers would confine the DAST to a smaller volume, effectively increasing the DAST concentration in these areas promoting crystallization.

#### 4.3.2.3 *Photostability*

The spherulite structure was surprisingly photochemically robust. The SHG signal of pure spherulites showed little or no degradation after

successive scans at powers of 40.0 mW. DAST, a photo-stable laser dye, does begin to decompose within the spherulite after successive scans at 2.5 mW.

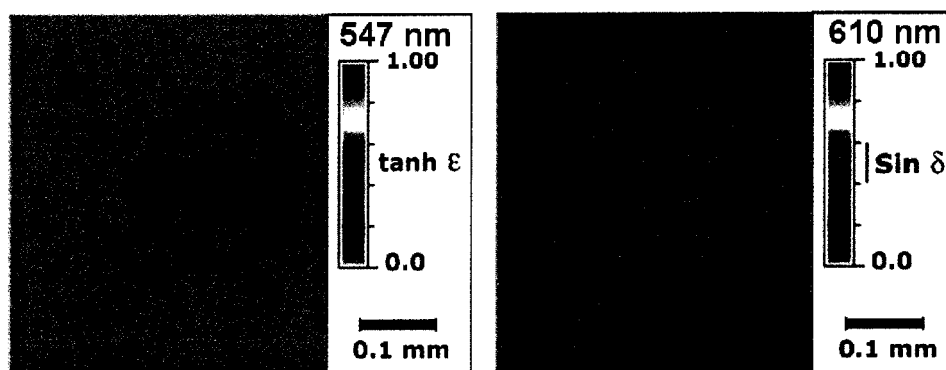


**Figure 4.18.** Linear dichroism (left) and linear birefringence (right) images of a spherulite containing 0.1 wt. % DAST after several high power (20.0 mW) two-photon microscopy scans.

Images of the linear dichroism show pitting corresponding to the photodecomposition of the dye (Figure 4.18). By contrast, the spherulite structure remains intact as the pits are conspicuously absent in the corresponding birefringence image. The bubbles present in the surrounding amorphous domain were formed during these scans.

#### 4.3.2.4 *Crystal Collimation*

Spontaneously nucleated spherulites within an amorphous glass are of little utility to device engineers. We investigated the effects of growth confinement within glass capillaries as a means of controlling spherulite growth. A molten sorbitol/dye solution is easily drawn into the rectangular capillaries (0.1 mm x 0.1 mm ID) by syringe then cooled to room temperature at which time the capillaries become filled with spherulites. After sealing the ends, 75% of the length of the capillary is submerged into an 80 °C oil bath melting existing spherulites and inhibiting further spontaneous nucleation. The capillary is then pulled from the oil at 80 µm/hour initiating spherulite growth from the 'seeds'. This new growth quickly begins to collimate with the radial fibers all running parallel to the long axis of the capillary (Figure 4.19).



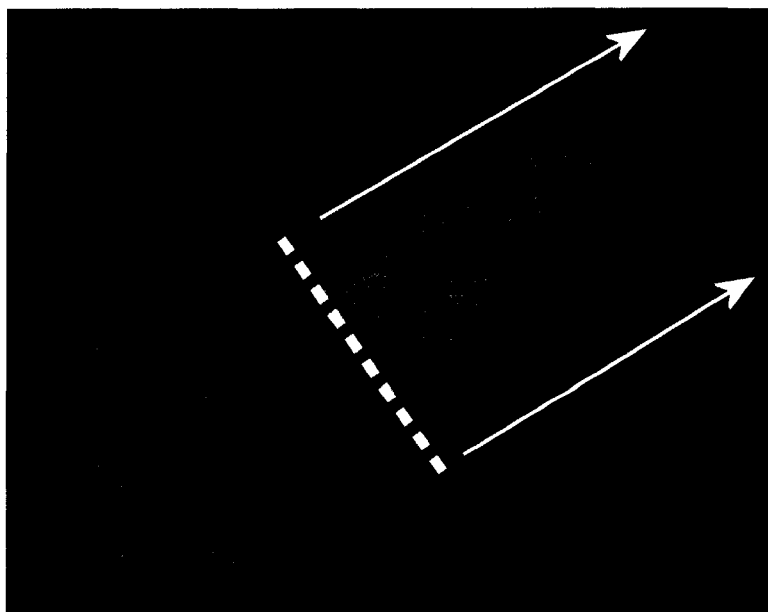


**Figure 4.19.** Optical micrograph of collimated sorbitol spherulite growth containing 0.4 wt % DAST imaged using linearly polarized light. Dashed white line represents the initial oil interface; white arrows indicate direction of collimated spherulite growth.

The collimated domain exhibits single crystal properties, illuminating and uniformly extinguishing every  $90^\circ$ , when viewed between cross polarizers. Domains as long as 1 cm were obtained using the capillary draw technique.

#### 4.3.2.5 Discussion - Conclusion

While sorbitol spherulites containing DAST do not show enhanced SHG arising from polar dye organization within the polycrystalline matrix, the general method may still produce successful results. The crystallization front of a growing spherulite is clearly capable of reorganizing dyes. In hindsight, DAST, chosen for its notoriety and NLO properties, was not the best choice for inclusion within a sorbitol spherulite. While the precise chemical composition of the crystallization front is unknown, it undoubtedly contains hydrogen bond donating -OH groups. Initially, one might consider the dimethylamino group of DAST a suitable hydrogen bond acceptor, but an analysis of the crystal structure suggests otherwise.

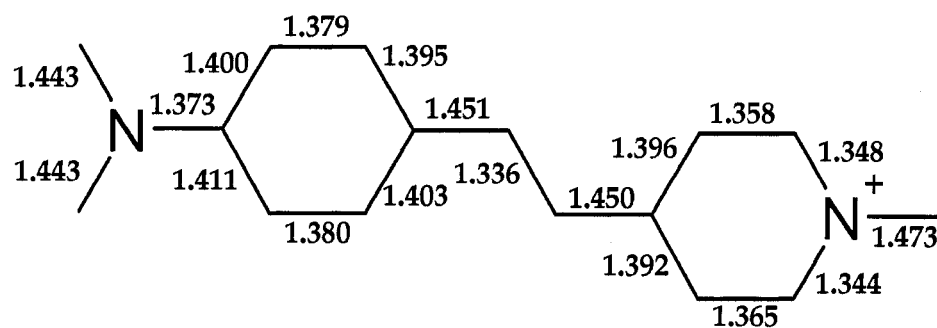


**Figure 4.20.** DAST skeleton with crystallographically determined bond lengths.

Rather than adopting a pyramidal geometry, the amino nitrogen is unambiguously trigonal planar. Furthermore, the benzene ring attached to the amino group exhibits quinoidal bond length alternation (Figure 4.20). This evidence suggests that the amino group's electron lone pair is not available for accepting a hydrogen bond. Instead, the lone pair has been donated into the plane of conjugation for this molecule.

The sorbitol spherulites have been proven to be photochemically robust, capable of withstanding intense high power laser radiation without damage. Collimation experiments demonstrated that the spherulite technology can be successfully transferred into traditional wave-guiding structures. Choosing a polar dye that possesses a complimentary hydrogen bond accepting group on one end of the molecule could ostensibly result in a stronger non-covalent interaction between the dye and the crystallization front leading to polar dye organization and a new generally applicable methodology for fabricating electrooptic devices.

#### 4.4 Experimental

**Crystal Growth:** D-sorbitol ( $\gamma$ -polymorph), amaranth (acid red 27, C.I.# 16185, 80% dye content), and *trans*-4-[4-(dimethylamino)styryl]-1-methylpyridinium *p*-toluenesulfonate (DAST, dye content 98%) were purchased from Aldrich and used without further purification. A typical preparation (0.5 wt % amaranth): 0.025 g of amaranth was added to 5.0 g of sorbitol and the dry solids were stirred in a 20 mL glass vial until uniformly colored. The uncapped vial was then placed in a 105-110 °C dry oven for 4-6 hours or until a clarified solution was obtained. Approximately 50  $\mu$ L of this solution was then pipetted onto a plain glass microscope slide (Richard Allen Scientific #4700) and covered with a micro cover glass (VWR, 25 x 25 mm, No.1). The glass slide was then placed back in the oven and the droplet was allowed to spread under the weight of the cover glass. Once spreading had stopped the sample was uniformly compressed such that the dyed sorbitol layer was approximately 10  $\mu$ m thick measured with a standard caliper. The sample was then set aside to crystallize at room temperature (23 °C). Spherulite nuclei were generally visible after 12 hours,

and spherulites suitable for imaging and spectroscopy were present 36 to 48 hours later.

**Spectroscopy:** Solution spectra were obtained with the cuvette sampling bench of the SI Photonics model 440 UV/Vis spectrophotometer. Crystal absorption spectra were obtained by coupling the spectrometer to an Olympus BX50 transmission microscope via a 200  $\mu\text{m}$  fiber-optic. The extinction directions of the crystals were used to orient the sample relative to the input polarization. Instec HS400 heating stage with a platinum resistance temperature detector was used to drive the formation of the bâtonnets.

**Second Harmonic Generation:** A mode-locked linearly polarized Ti:Sapphire laser (120 fs pulses at 800 nm with a repetition rate of 80 Mhz and powers of 1.0 - 40.0 mW) was coupled to a Nikon inverted microscope. The laser was focused onto the sample through a high numerical aperture 100x oil immersion objective. The light emitted by the sample were collected through the same objective and directed to a photon counting photomultiplier tube. The emitted light was passed through a 10 nm band pass filter centered at 400 nm. The contribution of two photon induced luminescence to the measured SHG intensity was determined by shifting

the excitation wavelength to 830 nm so that the second harmonic (415 nm) would be rejected by the band pass filter. Images were obtained by raster scans ( $80 \times 80 \mu\text{m}^2$  with a step size of  $1\text{-}5 \mu\text{m}$ ) of the sample using a closed loop piezo-electric scan stage.

**Metripol:** In order to quantify linear anisotropies we have employed the rotating polarizer technique as embodied in the Metripol microscope.<sup>88</sup> The optical train consists of a filter as monochrometer, a mechanically rotating polarizer, a sample inducing the phase shift  $\delta$ , a quarter wave retarder and a polarizer aligned at  $45^\circ$  towards the quarter wave plate's eigenray directions:

$$\mathbf{A}' = \mathbf{M}_{45\text{-pol}} \mathbf{M}_{\lambda/4} \mathbf{M}_{\text{sample}} \mathbf{R}_\theta \mathbf{J}_x .$$

where  $\mathbf{J}_x$  is the Jones matrix<sup>137</sup> for linearly polarized light operated on by a rotation matrix ( $\mathbf{R}_\theta$ ), and Jones matrices representing the sample that is linearly birefringent ( $\mathbf{M}_{\text{sample}}$ ), a quarter wave plate ( $\mathbf{M}_{\lambda/4}$ ), and a linear polarizer ( $\mathbf{M}_{45\text{-pol}}$ ). The position of the sample with respect to the rotating polarizer is defined by the angle  $\theta$ ,  $\theta = \alpha - \phi$ , where  $\alpha$  is the rotation angle of the polarizer and  $\phi$  the angle between the slow vibration direction of the

sample and the polarizer when  $\alpha = 0$ . From the amplitudes, the normalized intensity  $I/I_0$  is found directly as:

$$\begin{aligned}\frac{I}{I_0} &= A'^* \cdot A' = 2 \cdot \frac{1}{4} \left[ (\cos \theta e^{ix} - \sin \theta e^{-ix}) (\cos \theta e^{-ix} - \sin \theta e^{ix}) \right] \\ &= \frac{1}{2} [1 + \sin 2(\alpha - \phi) \sin \delta]\end{aligned}$$

In the Metripol method, intensity measurements at discrete steps ( $\alpha_i$ ) generate expressions that are easily converted to linear polynomials. Data collected over full periods yield Fourier coefficients from which the variable parameters are extracted analytically.

Simple modifications of the optical train permit the measurement of LD.<sup>138</sup> The anisotropic absorption may be determined by removing the quarter wave plate and analyzer. The Jones vector for a LD measurement using MetriPol is:

$$\mathbf{A}' = \mathbf{M}_{LD, LB} \mathbf{R}_\theta \mathbf{A}_x$$

$$\mathbf{A}' = t \cdot \begin{bmatrix} t_x e^{i\frac{\delta}{2}} & 0 \\ 0 & t_y e^{-i\frac{\delta}{2}} \end{bmatrix} \cdot \begin{bmatrix} \cos \theta & \sin \theta \\ -\sin \theta & \cos \theta \end{bmatrix} \cdot \begin{bmatrix} 1 \\ 0 \end{bmatrix} = t \cdot \begin{bmatrix} t_x e^{i\frac{\delta}{2}} \cos \theta \\ -t_y e^{-i\frac{\delta}{2}} \sin \theta \end{bmatrix},$$

where  $t$  is the average transmission coefficient,  $t_{x/y}$  are the transmission coefficients in the  $x$ ,  $y$  directions, and  $\theta$  is the initial angle between the

polarizer and the slow vibration direction of the sample. After some manipulation,<sup>99</sup> we can relate  $\tanh \varepsilon$  ( $\varepsilon$  is the difference between optical densities in orthogonal directions) to the orthogonal transmission terms  $T'''$  giving:

$$\tanh \varepsilon = \frac{\sinh \varepsilon}{\cosh \varepsilon} = \frac{(e^{+\varepsilon} - e^{-\varepsilon})/2}{(e^{+\varepsilon} + e^{-\varepsilon})/2} = \frac{T' - T''}{T' + T''}.$$

### Mueller Matrix Image Simulation

Polarized light is commonly expressed in either terms of the Jones or Stokes vector formalism. Both methods address the polarization state of light by dividing the electric field into two orthogonal parts as express below.

$$J = \begin{bmatrix} E_x \\ E_y \end{bmatrix}$$

$$S = \begin{bmatrix} |E_x|^2 + |E_y|^2 \\ |E_x|^2 - |E_y|^2 \\ 2 \Re(E_x E_y^*) \\ 2 \Im(E_x E_y^*) \end{bmatrix}$$

The Stokes vector formalism has the advantage of being able to treat partially polarized and incoherent light. The affect of an optical element on



the polarization state of incident light can be described by multiplying the Stokes vector by the Mueller matrix of that element.

$$S_{out} = M S_{in}$$

We document the routine used to create simulated Mueller images of dyed spherulites. The simulation takes into account growth, diattenuation, and retardation of a dyed spherulite sample.

Nucleation is assumed to occur at random, and growth rate is constant. The simulation starts by creating a set of random nucleation times. The first spherulite nucleates and grows at a constant rate and random location. During every cycle of the simulation, the spherulite grows radially by one pixel. Upon reaching the second nucleation time, another nucleus is added to the simulation in a random unoccupied location. This routine is continued until all regions of the simulated area are covered by a spherulite.

After the simulated region has been covered by spherulites, a blending routine occurs. The first spherulite is isolated and assigned a thickness,  $L$ , dictated by the user. A padded average filter is then applied to the whole

image. The average filter smoothly and linearly decreases the thickness from  $L$  to zero at the spherulite's edge over a range dictated by the user.

The Mueller matrix for each pixel of the isolated spherulite region is then calculated by the following equations:

$$d_{x,y} = \sqrt{(pixel_x - center_x)^2 + (pixel_y - center_y)^2}$$

$$\theta_{x,y} = \arctan\left(\frac{pixel_y - center_y}{pixel_x - center_x}\right)$$

$center$  is the center of nucleation for the spherulite.  $pixel$  is the current pixel location.

$$\delta_{x,y} = \frac{2\pi\Delta n}{\lambda} d_{x,y} \arctan\left(\frac{l_{x,y}}{d_{x,y}}\right)$$

$l_{x,y}$  is the thickness at that location.  $\Delta n$  is the difference in refractive index for the orthogonal directions.  $\lambda$  is the wavelength of light.

$$p_{\parallel} = e^{-K_1 l_{x,y} - (K_3 - K_1) d_{x,y} \arctan\left(\frac{l_{x,y}}{d_{x,y}}\right)}$$

$$p_{\perp} = e^{-K_2 l_{x,y}}$$

$K$  is the absorbance vector in the form  $[K_1, K_2, K_3]$  for the three orthogonal directions.

$$M_{ret} = \begin{bmatrix} 1 & 0 & 0 & 0 \\ 0 & 1 & 0 & 0 \\ 0 & 0 & \cos\delta_{x,y} & \sin\delta_{x,y} \\ 0 & 0 & -\sin\delta_{x,y} & \cos\delta_{x,y} \end{bmatrix}$$

$$M_D = \begin{bmatrix} p_{\parallel}^2 + p_{\perp}^2 & p_{\parallel}^2 - p_{\perp}^2 & 0 & 0 \\ p_{\parallel}^2 - p_{\perp}^2 & p_{\parallel}^2 + p_{\perp}^2 & 0 & 0 \\ 0 & 0 & 2 p_{\parallel} p_{\perp} & 0 \\ 0 & 0 & 0 & 2 p_{\parallel} p_{\perp} \end{bmatrix}$$

$$M_{rot} = \begin{bmatrix} 1 & 0 & 0 & 0 \\ 0 & \cos(2\theta_{x,y}) & \sin(2\theta_{x,y}) & 0 \\ 0 & -\sin(2\theta_{x,y}) & \cos(2\theta_{x,y}) & 0 \\ 0 & 0 & 0 & 1 \end{bmatrix}$$

$$M_{x,y} = M_{rot} M_D M_{ret} M_{rot}$$

$M_{ret}$  is the Mueller matrix for a retarder.  $M_D$  is the Mueller matrix for a diattenuator.  $M_{rot}$  is the Mueller matrix of rotation.  $M_{x,y}$  is the Mueller matrix for the current spherulite at that pixel location. When the blended region of two spherulites overlap, the Mueller matrix is equal to the product of the Mueller matrix for each spherulite in the overlapping region.

The image is then compiled into the 16 separate Mueller matrix images. One for each element in the Mueller matrix.

## REFERENCES

1. Michl J.; Thulstrup, E. Spectroscopy with polarized light: solute alignment by photoselection, in liquid crystals, polymers and membranes. 2<sup>nd</sup> edition, VCH publishers, 1995.
2. Ambronn, H. Pleochroismus gefärbter zellmembranen, *Ber. Deutsch. Botan. Ges.* **1888**, 6, 85.
3. Senarmont, H. de. Expériences sur la production artificielle du polychroïsme dans les substances cristallisées. *C. R. Seances Acad. Sci.* **1854**, 38, 101-105.
4. (a) Becquerel, H. Recherches sur les variations des spectres d'absorption dans les cristaux. *Ann. Chim. Phys.* **1888**, 14, 170-257. (b) Seherr-Thoss, M. von, Über kunstlichen Dichroismus. *Ann. Phys. Chem.* 1879, 242, 270-287. (c) Kahr, B.; Lovell, S.; Subramony, J. A. The progress of logwood extract. *Chirality*, **1998**, 10, 66-77.
5. Brewster, D. On the laws which regulate the absorption of polarised light by doubly refracting crystals. *Phil. Trans. Royal Soc. London*, **1819**, 109, 11-28.
6. Brewster, D. On the laws of polarisation and double refraction in regularly crystallized bodies. *Phil. Trans. Royal Soc. London*, **1818**, 108, 199-273.
7. Images from <http://www.faceters.com/askjeff/answer36.shtml>
8. Fraunhofer, 1817
9. Brewster, D. Observations on the lines of the solar spectrum, and on those produced by the Earth's atmosphere, and by the action of nitrous acid gas. *Trans. R. Soc. Edinburgh*, **1834**, 12, 519-530.

10. Kirchhoff, G.; Bunsen, R. Chemical analysis by observation of spectra. *Annalen der Physik und der Chemie (Poggendorff)*, **1860**, 110, 161-189.
11. Sorby, H. C. On a definite method of qualitative analysis of animal and vegetable colouring-matters by means of the spectrum microscope. *Proc. Royal Soc. London*, **1866**, 15, 433-455.
12. Bunsen, R. Ueber die erscheinungen beim absorptions-spectrum des didyms. *Annalen der Physik und der Chemie Pogg.*, **1866**, 128, 100-108.
13. Buckley, H. E. Mem. Proc. Manchester Lit. Philos. Soc. **1951**, 92, 77-123.
14. Comoretto, D; Rossi, L.; Borghesi, A. Optical properties of potassium acid phthalate. *J. Mater. Res.*, **1997**, 12, 1262-1267.
15. Kelley, M. P.; Janssens, B.; Kahr, B.; Vetter, W. M. Recognition of Dyes by K<sub>2</sub>SO<sub>4</sub> Crystals: Choosing Organic Guests for Simple Salts. *J. Am. Chem. Soc.* **1994**, 116, 5519-5520.
16. Bastin, L.; Kahr, B. Engineering oriented gases: The mechanism of dyeing potassium sulfate. *Tetrahedron*, **2000**, 56, 6633-6643.
17. Gurney, R. W.; Mitchell, C. A.; Ham, S.; Bastin, L. D.; Kahr, B. Salting Benzenes. *J. Phys. Chem. B*, **2000**, 104, 878-892.
18. Kahr, B.; Gurney, R. W. Dyeing Crystals. *Chem. Rev.* **2001**, 101, 893-951.
19. Okaya, Y. The crystal structure of potassium acid phthalate, KC<sub>6</sub>H<sub>4</sub>COOH.COO. *Acta Cryst.* **1965**, 19, 879-882.
20. Eremina, T.A.; Furmanova, N. G.; Malakhova, L. F.; Okhrimenko, T. M.; Kuznetsov, V. A. Absolute configuration and morphology of potassium bipthalate crystal. *Crystallogr. Rep.* **1993**, 38, 554-556.
21. Barbon, A.; Bellinazzi, M.; Benedict, J. B.; Brustolon, M.; Fleming, S. D.; Jang, S.-H.; Kahr, B.; Rohl, A. L. Luminescent Probes of Crystal

- Growth: Surface Charge and Polar Axis Sense in Dye-Doped Potassium Hydrogen Phthalate. *Angew. Chem. Int. Ed.* 2004, 43, 5328-5331.
22. Bullard, T.; Kurimoto, M.; Avagyan, S.; Jang, S.-H.; Kahr, B. Luminescence imaging of growth hillocks in potassium hydrogen phthalate. *Transactions ACA*, 2004, 39, 62-72.
  23. Burton, W. K.; Cabrera, N.; Frank, F. C. The growth of crystals and the equilibrium structure of their surfaces. *R. Soc. London. Philos. Trans. A*, 1951, 243, 299-358.
  24. Hottenhuis, M. H. J.; Lucasius, C. B. The influence of internal crystal structure on surface morphology; in situ observations of potassium hydrogen phthalate {010}. *J. Cryst. Growth*, 1989, 94, 708-720.
  25. Haugen, G. R.; Melhuish, W. H. Association and self-quenching of proflavine in water. *Trans. Faraday Soc.* 1964, 60, 386-394; Pileni, M. - P.; Graetzel, M. Light-induced redox reactions of proflavin in aqueous and micellar solution. *J. Phys. Chem.* 1980, 84, 2402-2406; Yamaoka, K.; Shimadzu, M. Film dichroism. VI. Linearly-polarized absorption spectra of neutral and divalent 3,6-diaminoacridine dyes in the stretched poly(vinyl alcohol) film. *Bull. Chem. Soc. Jpn.* 1983, 56, 55-59; Schoonheydt, R. A.; Cenens, J.; De Schrijver, F. C. Spectroscopy of proflavine adsorbed on clays. *J. Chem. Soc., Faraday Trans. I*, 1986, 82, 281-289; Ramaraj, R.; Rachel Jeyanthi, D.; Srinivasan, C. Adsorption characteristics and spectroscopic studies of 3,6-diaminoacridine adsorbed on clays. *Ind. J. Chem.* 1991, 30A, 1044-1046.
  26. Dauber-Osguthorpe, P.; Roberts, V. A.; Osguthorpe, D. J.; Wolff, J.; Genest, M.; Hagler, A. T. Structure and energetics of ligand binding to proteins: *Escherichia coli* dihydrofolate reductase-trimethoprim, a drug-receptor system. *Proteins: Struct., Func., Genet.* 1988, 4, 31-47.
  27. Obendorf, S. K.; Carrell, H. L.; Glusker, J. P. Proflavin dichloride dihydrate (3,6-diaminoacridine dihydrochloride dihydrate) *Acta Cryst.*, 1974, B30, 1408-1411.

28. Wustholz, K.; Kahr, B.; Reid, P. Single-molecule orientations in dyed salt crystals. *J. Phys. Chem. B*, **2005**, *109*, 16357-16362.
29. Fister, J. C.; Harris, J. M. Time- and wavelength resolved delayed fluorescence emission from acridine yellow in an inhomogeneous saccharide glass. *Anal. Chem.* **1996**, *68*, 639-646.
30. Bellinazzi, M.; Barbon, A.; Kahr, B.; Benedict, J. B.; Brustolon, M. Time-resolved EPR spectra of the triplet excited states of diaminoacridine guests in polar potassium hydrogen phthalate single crystals. *Phys. Chem. Chem. Phys.* **2006**, *8*, 379-385.
31. Grivet, J. P. ESR of acridine in its metastable triplet state. *Chem. Phys. Lett.*, **1971**, *11*, 267-270.
32. Hartman, P.; Perdok, W. G. On the relations between structure and morphology of crystals. III. *Acta Cryst.* **1955**, *8*, 525-529. Woensdregt, C. F. Computation of surface energies in an electrostatic point charge model: II. Application to zircon ( $\text{ZrSiO}_4$ ). *Phys. Chem. Minerals*, **1992**, *19*, 59-69.
33. Solc, Z.; Kvapil, J.; Vlcek, J. Crystallisation of potassium acid phthalate. *Krist. Tech.* **1973**, *8*, 59-66. Ester, G. R.; Price, R.; Halfpenny, P. J. An atomic force microscopic investigation of surface degradation of potassium hydrogen phthalate (KAP) crystals caused by removal from solution. *J. Cryst. Growth*, **1997**, *182*, 95-102.
34. Hermes, R. E. Progress in solid-state dye laser development. *Proc. Int. Conf. Lasers*, **1991**, 1990, 718-724,
35. Whitehurst, C.; Shaw, D. J.; King, T. A. Sol-gel solid-state lasers doped with organic molecules. *Proc. SPIE-Int. Soc. Opt. Eng.* **1990**, *1328*, 183-193.,
36. Aldag, H. R. Solid-state dye laser for medical applications. *Proc. SPIE - Int. Soc. Opt. Eng.* **1994**, *2115*, 184-189.

37. Jones, A. L. Jr.; DeYoung, R. J.; El-Sayid-Ele, H. Compact ozone differential absorption lidar (DIAL) transmitter using solid-state dye polymers. *NASA/TM*, **2001**, 211028, 1-40.
38. Bornemann, R.; Lemmer, U.; Theil, E. Continuous-wave solid-state dye laser. *Opt. Lett.* **2006**, *31*, 1669-1671.
39. (a) Carbonaro, C. M.; Anedda, A.; Grandi, S.; Magistris, A. Hybrid materials for solid-state dye laser applications. *J. Phys. Chem. B* **2006**, *110*, 12932-12937. (b) Russell, J. A.; Pacheco, D. P.; Russell, W. H.; Aldag, H. R.; Manenkov, A. A. Laser threshold and efficiency measurements of solid-state dye lasers operating in the near-infrared under microsecond pumping. *Proc. SPIE*, **2002**, 4630, 24-33.
40. Rifani, M.; Yin, Y. -Y.; Elliott, D. S.; Jay, M. J.; Jang, S. -H.; Kelley, M. P.; Bastin, L.; Kahr, B. Solid-state dye lasers from stereospecific host-guest interactions. *J. Am. Chem. Soc.* **1995**, *117*, 7572-7573. Kahr, B.; Jang, S.-H.; Elliott, D. S. *US Patent 5 701 323*, **1997**. Rifani, M. *Ph.D. Dissertation*, Purdue University, **1998**.
41. Ihlein, G.; Schüth, F.; Krauss, O.; Vietze, U.; Laeri, F. Alignment of a laser dye in the channels of the  $\text{AlPO}_4\text{-5}$  molecular sieve. *Adv. Mater.* **1998**, *10*, 1117-1119. Vietze, U.; Krauss, O.; Laeri, F.; Ihlein, G.; Schüth, F.; Limburg, B.; Abraham, M. Zeolite-dye microlasers. *Phys. Rev. Lett.* **1998**, *81*, 4628-4631. Braun, I.; Ihlein, G.; Laeri, F.; Nöckel, J. U.; Schulz-Ekloff, G.; Schüth, F.; Vietze, U.; Weiss, Ö.; Wöhrle, D. Hexagonal microlasers based on organic dyes in nanoporous crystals. *Appl. Phys. B* **2000**, *70*, 335-343.
42. Zhang, G. C.; Wang, G. F.; Guan, X. G. Research and development of laser-nonlinear multi-functional crystals. *J. Inorg. Mat.* **2001**, *16*, 769-778.
43. Jiang, H.; Li, J. Wang, J.; Hu, X.-B.; Liu, H.; Teng, B.; Zhang, C. -Q.; Dekker, P.; Wang, P. Growth of  $\text{Yb:YAl}_3(\text{BO}_3)_4$  crystals and their optical and self-frequency-doubling properties. *J. Cryst. Growth*, **2001**, *233*, 248-252.



44. Gamelin, D. R.; Güdel, H. U. Design of luminescent inorganic materials: new photophysical processes studied by optical spectroscopy. *Acc. Chem. Res.* **2000**, *33*, 235-242. Gamelin, D. R.; Güdel, H. U. Upconversion processes in transition metal and rare earth metal systems. *Top. Curr. Chem.* **2001**, *214*, 1-56.
45. Albota, M.; Beljonne, D.; Brédas, J. -L.; Ehrlich, J. E.; Fu, J. -Y.; Heikal, A. A.; Hess, S. E.; Kogej, T.; Levin, M. D.; Marder, S. R.; McCord-Maughon, D.; Perry, J. W.; Röckel, H.; Rumi, M.; Subramaniam, G.; Webb, W. W.; Wu, X. -L.; Xu, C. Design of organic molecules with large two-photon absorption cross sections. *Science*, **1998**, *281*, 1653-1656. Reinhardt, B. A.; Brott, L. L.; Clarson, S. J.; Dillard, A. G.; Bhatt, J. C.; Kannan, R.; Yuan, L.; He, G. S.; Prasad, P. N. Highly active two-photon dyes: design, synthesis, and characterization toward application. *Chem. Mater.* **1998**, *10*, 1863-1874. Kannan, R.; He, G. S.; Yuan, L.; Xu, F.; Prasad, P. N.; Dombroskie, A. G.; Reinhardt, B. A.; Baur, J. W.; Vaia, R. A.; Tan, L. - S. Diphenylaminofluorene-based two-photon-absorbing chromophores with various  $\pi$ -electron acceptors. *Chem. Mater.* **2001**, *13*, 1896-1904. Cho, B. R.; Son, K. H.; Lee, S. H.; Song, Y. -S.; Lee, Y. -K.; Jeon, S. -J.; Choi, J. H.; Lee, H.; Cho, M. Two photon absorption properties of 1,3,5-tricyano-2,4,6-tris(styryl)benzene derivatives. *J. Am. Chem. Soc.* **2001**, *123*, 10039-10045.
46. Benedict, J. B.; Wallace, P. M.; Reid, P. J. Jang, S.-H.; Kahr, B. Up-conversion Luminescence in Dye-Doped Crystals of Potassium Hydrogen Phthalate. *Adv. Mater.* **2003**, *15*, 1068-1070.
47. Belyaev, L. M.; Belikova, G. S.; Gil'varg, A. B.; Golovei, M. P.; Kalinkina, I. N.; Kosourov, G. I. Nonlinear properties of potassium biphthalate crystal. *Opt. Spectrosc.* **1970**, *29*, 522-524.
48. Brackmann, U. *Lambdachrome laser dyes, 2nd revised edition*. Lambda Physik GmbH, Göttingen, **1994**.
49. The observed phase-matching directions for the frequency doubling of an 800 nm pump laser to 400 nm are approximately perpendicular to the  $\{11\bar{1}\}$  faces and are consistent with the values reported in

- Belyaev, L. M.; Belikova, G. S.; Gil'varg, A. B.; Golovei, M. P.; Kalinkina, I. N.; Kosourov, G. I. Nonlinear properties of potassium biphthalate crystal. *Opt. Spectrosc.* **1970**, *29*, 522-524.
50. Pålsson, L. -O.; Monkman, A. P. Measurements of solid-state photoluminescence quantum yields of films using a fluorimeter. *Adv. Mater.* **2002**, *14*, 757-758.
  51. Arbeloa, F. L.; Arbeloa, T. L.; Arbeloa, I. L.; Costela, A.; Garcia-Moreno, I.; Figuera, J. M.; Amat-Guerri, F.; Sastre, R. Relations between photophysical and lasing properties of rhodamines in solid polymeric matrices. *Appl. Phys. B*, **1997**, *64*, 651-657.
  52. Costela, A.; Garcia-Moreno, I.; Gomez, C.; Garcia, O.; Sastre, R. New organic-inorganic hybrid matrices doped with rhodamine 6G as solid-state dye lasers. *Appl. Phys. B*, **2002**, *75*, 827-833.
  53. Springer, G. H.; Higgins, D. A. Multiphoton-excited fluorescence imaging and photochemical modification of dye-doped polystyrene microsphere arrays. *Chem. Mater.* **2000**, *12*, 1372-1377.
  54. Gaubert, P. Sur la coloration artificielle des cristaux. *Bull. Soc. Fr. Min.* **1900**, *23*, 211-221.
  55. Bernstein, J.; Davey, R.; Henck, J.-O. Concomitant polymorphs. *Angew. Chem. Int. Ed. Engl.* **1999**, *38*, 3440-3461.
  56. Pertsev, A. N. Syncrystallization processes in the gabbro-ultramafite complex of the ural platinum belt: geochemical variability of clinopyroxene in rocks from the Kytlym massif. *Geochem. Internat.* **2004**, *42*, 1078-1085; Mascherpa, C. D.; Mascherpa, G.; Chauvet, A. Cristallisation, syncrystallisation, et alliages moléculaires entre le lorazepam et l'oxazepam. *J. Sol. St. Chem.* **1993**, *103*, 298-306; Riera, A. M. I.; Pourroy, G.; Poix, P. Syncrystallization of  $\text{CoFe}_2\text{O}_4$  from ferric and cobaltous chlorides: physical properties of the precipitate. *J. Sol. St. Chem.* **1992**, *101*, 195-198; Chanh, N. B.; Clastre, J.; Gaultier, J.; Haget, Y.; Meresse, A.; Lajzerowicz, J.; Filhol, A.; Thomas, M. The tensor of compositional deformation. A new crystallographic way to

- analyse syncrystallization. *J. Appl. Cryst.* **1988**, *21*, 10-14; Brianso, M. C. Sels diastereoisomeres de phenyl-1 ethylamineet d'acides phenylacetiques a substitues p et n. Separation ou syncrystallisation: une explication cristallographique. *Acta Cryst. Sect. B.* **1981**, *37*, 618-620; Petit, B.; Bourlang, C. *Comptes Rendus Hebd. Seances Acad. Sci. Ser. C*, **1973**, C276, 1485-1488.
57. Benedict, J. B.; Cohen, D. E.; Lovell, S.; Rohl, A. L.; Kahr, B. What is syncrystallization? States of pH indicator methyl red in crystals of phthalic acid. *J. Am. Chem. Soc.* **2006**, *128*, 5548-5559.
  58. Mitchell, C.; Lovell, S.; Thomas, K.; Savickas, P.; Kahr, B. Charge transfer interactions in dyed crystals of aromatic carboxylic acids and their relevance to MALDI mass spectrometry. *Angew. Chem. Int. Ed. Engl.* **1996**, *35*, 1021-1023.
  59. Kurimoto, M.; Bastin, L. D.; Fredrickson, D.; Gustafson, P. N.; Jang, S.-H.; Kaminsky, W.; Lovell, S.; Mitchell, C. A.; Chmielewski, J.; Kahr, B. in *Morphology and dynamics of crystal surfaces in complex molecular systems*, De Yoreo, J. J.; Casey, W. H.; Malkin, A. J.; Vlieg, E.; Ward, M. D. eds. Materials Research Society, Pittsburgh, 2001, 620, M981-M9810.
  60. Kahr, B.; Gurney, R. W. Dyeing Crystals. *Chem. Rev.* **2001**, *101*, 893-951.
  61. Kahr, B.; Vasquez, L. Painting crystals. *CrystEngComm*, **2002**, *4*, 514-516.
  62. Lehmann, O. Uber kunstliche farbung von krystallen. *Z. Phys. Chem.*, **1891**, *8*, 543-553; Uber kunstliche farbung von krystallen und amorphen Korpen. *Ann. Phys. Chem.* **1894**, *51*, 47-76.
  63. Gaubert, P. Sur la coloration artificielle des cristaux d'acide phthalique. *Bull. Soc. Fr. Min.* **1905**, *28*, 286-304; De l'influences des matieres colorants d'une eau mere sur la forme des cristaux qui s'en deposit (acid phtalique). *Comptes Rendus Acad. Sci. Paris*, **1906**, *142*, 219-221.

64. Gaubert, P. *Soc. Chim. Phys.* **1911**, *1*, 33.
65. Gaubert, P. Modifications du facies des cristaux de phloro-glucine par les matieres colorants et action de la chaleur sur la coloration. *Comptes Rendus Acad. Sci. Paris*, **1935**, *200*, 1120-1122.
66. Buckley, H. E. *Crystal Growth*, Wiley, New York, **1951**; pp 346.
67. Bunn, C. W. Adsorption, oriented overgrowth and mixed crystal formation. *Proc. Roy. Soc. London, Ser. A*, **1933**, *141*, 567-593.
68. Gaubert, P. Diffusion sous l'influence de la chaleur de la matiere colorante dans les cristaux d'acide phthalique colores artificiellement. *Comptes Rendus Acad. Sci. Paris*, **1937**, *204*, 599-601.
69. The choice of *bâtonnet* to describe the separated dye particles was likely influenced by the introduction of this term into the liquid crystal literature at about the same time. See: Friedel, G. *Ann. Phys.* **1922**, *18*, 273-474.
70. Gebhardt, M., Neuhaus, A. Hellwege, K.-H.; Hellwege, A. M. (Eds.) *Epitaxy Data of Inorganic and Organic Crystals Landolt-Börnstein: Numerical Data and Functional Relationships in Science and Technology - New Series Group 3: Condensed Matter, Vol. 8*, Springer, Berlin, **1972**.
71. Neuhaus, A. Über die normale mischbarkeit organischer substanzen. (Anomale mischkristalle IV.) *Z. Krist.* **1941**, *103*, 297-327. To compare Neuhaus's triclinic methyl red cell ( $a = 8.45 \text{ \AA}$ ,  $b = 11.6 \text{ \AA}$ ,  $c = 9.30 \text{ \AA}$ ,  $\alpha = 115^\circ$ ,  $\beta = 125^\circ$ ,  $\gamma = 66^\circ$ . with our own we must adopt the following cell based on vectors derived from the monoclinic crystal in Table 1: ( $[010] = 8.50 \text{ \AA}$ ,  $[111] = 11.72 \text{ \AA}$ ,  $[\bar{1}\bar{1}0] = 9.16 \text{ \AA}$ ,  $\alpha = 116.5^\circ$ ,  $\beta = 124.6^\circ$ ,  $\gamma = 66.3^\circ$ ).
72. Lindenberg, W. Über die abh ngigkeit von kristalltracht und -habitus organischer substanzen vom Lösungsmittel. *N. Jahr. Min. Ab.* **1956**, *89*, 149-181.

73. Gale J. D., Rohl A. L. The general utility lattice program (gulp). *Mol. Simul.*, **2003**, 29, 291-341.
74. Fleming S. D.; Rohl A. L. GDIS: a visualization program for molecular and periodic systems. *Z. Kristallogr.* **2005**, 220, 580-584.
75. Ermer, O. Unusual structural feature of crystalline phthalic acid. *Helv. Chim. Acta* **1981**, 64, 1903-1909; Veenendaal, A. L.; MacGillavry, C. H. Phthalic acid at low temperature. *Acta Cryst.* **1954**, 7, 775; van Schalkwyk, T. G. D. The crystal structure of phthalic acid. *Acta Cryst.* **1954**, 7, 775.
76. Ramette, R. W.; Dratz, E. A.; Kelly, P. W. Acid-base equilibria of methyl red. *J. Phys. Chem.* **1962**, 66, 527-532.
77. Drummond, C. J.; Grieser, F.; Healy, T. W. Acid-base equilibria in aqueous micellar solutions part 4. azo indicators. *J. Chem. Soc. Faraday Trans. I*, **1989**, 85, 561-578.
78. Singh, A. K.; Ghosh, J. C. A recalculation of pK1 and pK2 of o-phthalic acid at a number of temperatures. *J. Indian Chem. Soc.* **1983**, 60, 702-704; First dissociation constant of o-phthalic acid from 283.15 to 323.15 K. *J. Indian Chem. Soc.* **1985**, 62, 158-160.
79. Moreiras, D.; Solans, J.; Solans, X.; Miravittles, C.; Germain, G.; Declercq, J. P. 4-dimethylaminoazobenzene-2'-carboxylic acid (methyl red), C<sub>15</sub>H<sub>15</sub>N<sub>3</sub>O<sub>2</sub>. *Cryst. Struct. Comm.* **1980**, 9, 921-924.
80. Tuble, S. C.; Anwar, J.; Gale, J. D. An approach to developing a force field for molecular simulation of Martensitic phase transitions between phases with subtle differences in energy and structure. *J. Am. Chem. Soc.* **2004**, 126, 396-405
81. Frisch, M. J.; Trucks, G. W.; Schlegel, H. B.; Scuseria, G. E.; Robb, M. A.; Cheeseman, J. R.; Montgomery, J. A., Jr.; Vreven, T.; Kudin, K. N.; Burant, J. C.; Millam, J. M.; Iyengar, S. S.; Tomasi, J.; Barone, V.; Mennucci, B.; Cossi, M.; Scalmani, G.; Rega, N.; Petersson, G. A.; Nakatsuji, H.; Hada, M.; Ehara, M.; Toyota, K.; Fukuda, R.; Hasegawa,

- J.; Ishida, M.; Nakajima, T.; Honda, Y.; Kitao, O.; Nakai, H.; Klene, M.; Li, X.; Knox, J. E.; Hratchian, H. P.; Cross, J. B.; Adamo, C.; Jaramillo, J.; Gomperts, R.; Stratmann, R. E.; Yazyev, O.; Austin, A. J.; Cammi, R.; Pomelli, C.; Ochterski, J. W.; Ayala, P. Y.; Morokuma, K.; Voth, G. A.; Salvador, P.; Dannenberg, J. J.; Zakrzewski, V. G.; Dapprich, S.; Daniels, A. D.; Strain, M. C.; Farkas, O.; Malick, D. K.; Rabuck, A. D.; Raghavachari, K.; Foresman, J. B.; Ortiz, J. V.; Cui, Q.; Baboul, A. G.; Clifford, S.; Cioslowski, J.; Stefanov, B. B.; Liu, G.; Liashenko, A.; Piskorz, P.; Komaromi, I.; Martin, R. L.; Fox, D. J.; Keith, T.; Al-Laham, M. A.; Peng, C. Y.; Nanayakkara, A.; Challacombe, M.; Gill, P. M. W.; Johnson, B.; Chen, W.; Wong, M. W.; Gonzalez, C.; Pople, J. A. *Gaussian 03, Revision C.02*, Gaussian, Inc., Wallingford, CT, 2004.
82. Anex, B. G. Optical properties of highly absorbing crystals. *Mol. Cryst.* **1966**, *1*, 1-36
  83. For the spectral characteristics in a variety of polymer and glass matrices, see: Yariv, E.; Reisfeld, R.; Weiss, A. M. Optical nonlinearities of methyl red in various solid matrices. *SPIE*, **1993**, *1972*, 46-54.
  84. Etter, M. C. Encoding and decoding hydrogen-bond patterns of organic compounds. *Acc. Chem. Res.* **1990**, *23*, 120-126; Etter, M. C.; MacDonald, J. C.; Bernstein, J. Graph-set analysis of hydrogen-bond patterns in organic crystals. *Acta Crystallogr. B.* **1990**, *B46*, 256-262; Bernstein, J.; Davis, R. E.; Shimoni, L.; Chang, N.-L. Patterns in hydrogen bonding: functionality and graph set analysis in crystals. *Angew. Chem. Int. Ed. Engl.* **1995**, *34*, 1555-1573.
  85. The  $\text{MR}^\circ$ ,  $\text{MR}^\pm$ , and  $\text{MRH}^+$  structures were taken from the  $0.5\text{PA} \cdot \text{MR}$ ,  $2,5\text{-DHB} \cdot \text{MR}$ , and  $\text{MR} \cdot \text{HBr} \cdot \text{H}_2\text{O}$  structures, respectively.  $\text{MR}^-$  was taken from Pruchnik, F. P.; Banbula, M.; Ciunik, Z.; Chojnacki, H.; Latocha, M.; Skop. B.; Wilczok, T.; Opolski, A.; Wietrzyk, J.; Nasulewicz, A. Structure, properties and cytostatic activity of triorganotin (aminaryl)carboxylates. *Eur. J. Inorg. Chem.* **2002**, *12*, 3214-3221.

86. Foote, F. G.; Blake, F. C.; France, W. G. Adsorption at crystal-solution interfaces. *J. Phys. Chem.* **1930**, *34*, 2236-2240; Paine, P. A.; France, W. G. Adsorption at crystal-solution interfaces. VII. Effect of stirring and growth rates on the habit and dye adsorption of alum crystals. Influence of acid and alkali media on the habit of alum crystals. *J. Phys. Chem.* **1935**, *39*, 425-429.
87. Cerius<sup>2</sup> Version 4.0, Molecular Simulations Inc., San Diego, 1999.
88. Glazer, A. M.; Lewis, J. G.; Kaminsky, W. An automatic optical imaging system for birefringent media. *Proc. R. Soc. Lond. A*, **1996**, *452*, 2751-2765.
89. Krüger, R.; Pfenninger, A.; Fournier, I.; Glückman, M.; Karas, M. Analyte incorporation and ionization in matrix-assisted laser desorption/ionization visualized by pH indicator molecular probes. *Anal. Chem.* **2001**, *73*, 5812-5821.
90. Bonafede, S. J.; Ward, M. D. Selective nucleation and growth of an organic polymorph by ledge-directed epitaxy on a molecular crystal substrate. *J. Am. Chem. Soc.* **1995**, *117*, 7853-7861; Carter, P. W.; Ward, M. D. Topographically directed nucleation of organic crystals on molecular single-crystal substrates. *J. Am. Chem. Soc.* **1993**, *115*, 11521-11535.
91. Bonev, I. On the terminology of the phenomena of mutual crystal orientation. *Acta Crystallogr.* **1972**, *A28*, 508-512; Bailey, S. W.; Frank-Kamenetskii, V. A.; Godsztaub, S.; Kato, A.; Pabst, A.; Schulz, H.; Taylor, H. F. W.; Fleischer, M.; Wilson, A. J. C. Report of the international mineralogical association (IMA) – international union of crystallography (IUCr) joint committee on nomenclature. *Acta Cryst.* **1977**, *A33*, 681-684.
92. Ungemach, H. *Bull. Soc. Fr. Miner. Crist.* **1935**, *58*, 97; Sur la syntaxie et la polytypie *Z. Kristallogr.* **1935**, *91*, 1-22.
93. Palatnik, L. S.; Papirov, I. I. *Oriented Crystallization*, Metallurgia, Moscow, 1964; Cistijakov, Ju. D.; Schneider, H. G.; Weinhold, C.

*Epitaxie-Endotaxie*, Leipzig: Deutsches Verlag für Grundstoffindustrie, 1969.

94. Spangenberg, K.; Neuhaus, A. Künstlich gefarbte kristalle als biespiele sogenannter anomaler Mischkristalle und ihre mineralchemische bedeutung. *Chem. Erde*, **1930**, 5, 437-528.
95. Kleber, W. Z. *Phys. Chem.* **1959**, 212, 222-234.
96. Gaubert, P. Sur la modification du facies des cristaux par suite de leur syncrystallisation avec matiere etrangere dissoute dans l'eau mere. *Comptes Rendus Acad. Sci. Paris*, **1925**, 180, 378-380.
97. Gaubert, P. Sur la mélanges isomorphes. *Comptes Rendus Acad. Sci. Paris*, **1918**, 167, 491-494.
98. Seifert, H. *Fortschr. Min. Krist. Petro.* **1935**, 19, 103-182; **1936**, 20, 324-455; **1937**, 22, 187-488.
99. Kaminsky, W.; Claborn, K.; Kahr, B. Polarimetric imaging of crystals. *Chem. Soc. Rev.* **2004**, 33, 514-525.
100. Kaminsky, W.; Jin, L.-W.; Powell, S.; Maezawa, I.; Claborn, K.; Branham, C.; Kahr, B. Polarimetric imaging of amyloid. *Micron*, **2006**, 37, 324-338.
101. Otwinowski, Z.; Minor, W. Processing of x-ray diffraction data collected in oscillation mode. *Methods in Enzymology*, **1997**, 276, 307-326.
102. Altomare, A.; Burla, M. C.; Camalli, M.; Cascarano, G. L.; Giacovazzo, C.; Guagliardi, A.; Moliterni, A. G. G.; Polidori, G.; Spagna, R. SIR97: a new tool for crystal structure determination and refinement. *J. Appl. Cryst.* **1999**, 32, 115-119.
103. Sheldrick, G. M. University of Göttingen, Germany, 1997.
104. Dalton, L. R.; Robinson, B. H.; Jen, A. K.-Y.; Steier, W. H. Nielson, R. Systematic development of high bandwidth, low drive voltage



organic electro-optic devices and their applications. *Optical Materials*, **2002**, *21*, 19-28.

105. (a) Singer, K. D.; King, L. A. Relaxation phenomena in polymer nonlinear optical materials. *J. Appl. Phys.* **1991**, *70*, 3251-3255. (b) Wu, X.; Wu, J.; Liu, Y.; Jen, A. K.-Y. Highly Efficient, Thermally and Chemically Stable Second Order Nonlinear Optical Chromophores Containing a 2-Phenyl-tetracyanobutadienyl Acceptor *J. Am. Chem. Soc.* **1999**, *121*, 472 -473. (c) Shi, Y.; Zhang, C.; Zhang, H.; Bechtel, J. H.; Dalton, L. R.; Robinson, B.; Steier, W. H., Low (Sub-1-Volt) Halfwave Voltage Polymeric Electro-optic Modulators Achieved by Controlling Chromophore Shape. *Science*, **2000**, *288*, 119-122. (d) Ma, H.; Chen, B.; Sassa, T.; Dalton, L. R.; Jen, A. K.-Y. Highly efficient and thermally stable nonlinear optical dendrimer for electrooptics. *J. Am. Chem. Soc.* **2001**, *123*, 986-987. (e) Dalton, L. R. Organic electro-optic materials. *Pure Appl. Chem.* **2004**, *76*, 1421-1433. (f) Cho, M. J.; Kim, J. Y.; Kim, J. H.; Lee, S. H.; Dalton, L. R.; Choi, D. H. Heterocyclic nonlinear optical chromophores composed of phenothiazine or carbazole donor and 2-cyanomethylene-3-cyano-4,5,5-trimethyl-2,5-dihydrofuran acceptor. *Bull. Korean Chem. Soc.* **2005**, *26*, 77-84. (g) Dalton, L.; Robinson, B.; Jen, A.; Reid, P.; Eichinger, B.; Sullivan, P.; Akelaitis, A.; Bale, D.; Haller, M.; Luo, J.; Liu, S.; Liao, Y.; Firestone, K.; Bhatambrekar, N.; Bhattacharjee, S.; Sinness, J.; Hammond, S.; Buker, N.; Snoeberger, R.; Lingwood, M.; Rommel, H.; Amend, J.; Jang, S.-H.; Chen, A.; Steier, W. Electro-optic coefficients of 500 pm/V and beyond for organic materials. *Proc. of SPIE*, **2005**, *5935*, 1-12. (h) Dalton, L.; Scherer, A.; Chen, A.; Jen, A.; Reid, P.; Robinson, B.; Eichinger, B.; Hochberg, M.; Baehr-Jones, T.; Pyajt, A.; Takayesu, J.; Sullivan, P.; Akelaitis, A.; Lawson, R.; Bale, D.; Haller, M.; Luo, J.; Liu, S.; Liao, Y.; Firestone, K.; Bhattacharjee, S.; Sinness, J.; Hammond, S.; Sgro, A.; Buker, N.; Snoeberger, R.; Lingwood, M.; Steier, W. Organic electro-optic glasses for WDM applications. *Proc. of SPIE*, **2005**, *6014*, 1-15. (i) Dalton, L.; Robinson, B.; Jen, A.; Reid, P.; Eichinger, B.; Sullivan, P.; Akelaitis, A.; Bale, D.; Haller, M.; Luo, J.; Liu, S.; Liao, Y.; Firestone, K.; Bhatambrekar, N.; Bhattacharjee, S.; Sinness, J.; Hammond, S.; Buker, N.; Snoeberger, R.; Lingwood, M.; Rommel, H.; Amend, J.; Jang, S.-H.; Chen, A.; Steier, W. Acentric

- lattice electro-optic materials by rational design. *Proc. of SPIE*, **2005**, 5912, 1-12. (j) Dalton, L.; Robinson, B.; Jen, A.; Reid, P.; Eichinger, B.; Sullivan, P.; Akelaitis, A.; Bale, D.; Haller, M.; Luo, J.; Liu, S.; Liao, Y.; Firestone, K.; Sago, A.; Bhatambrekar, N.; Bhattacharjee, S.; Sinness, J.; Hammond, S.; Buker, N.; Snoeberger, R.; Lingwood, M.; Rommel, H.; Amend, J.; Jang, S.-H.; Chen, A.; Steier, W. Optimizing electro-optic activity in chromophore/polymer composites and in organic chromophore glasses. *Proc. of SPIE*, **2005**, 5990, 1-10. (k) Liao, Y.; Anderson, C. A.; Sullivan, P. A.; Akelaitis, A. J. P.; Robinson, B.; Dalton, L. R. Electro-Optical Properties of Polymers Containing Alternating Nonlinear Optical Chromophores and Bulky Spacers. *Chem. Mater.* **2006**, 4, 1062-1067.
106. Apitz, D.; Bertram, R. P.; Benter, N.; Hieringer, W.; Andreasen, J. W.; Nielsen, M. M.; Johansen, P.M.; Buse, K. Investigation of chromophore-chromophore interaction by electro-optic measurements, linear dichroism, x-ray scattering, and density functional calculations, *Phys. Rev. E*, **2005**, 72, 036610 (1-10).
  107. Wu, J. Birefringent and electro-optic effects in poled polymer films: steady-state and transient properties, *J. Opt. Soc. Am. B*, **1991**, 8, 142-152.
  108. Meredith, G. R.; VanDusen, J. G.; Williams, D. J. Optical and nonlinear optical characterization of molecularly doped thermotropic liquid crystalline polymers. *Macromolecules*, **1982**, 15, 1385-1389.
  109. Zbinden, R. Infrared Spectroscopy of High Polymers. Academic Press, New York, London, **1964**.
  110. Gregoriou, V. G.; Tzavalas, S.; Bollas, S. T. Angular dependence in infrared linear dichroism: a reevaluation of the theory. *Appl. Spectrosc.* **2004**, 58, 655-661.
  111. Kahr, B.; Claborn, K. The lives of Malus and his bicentennial law. *ChemPhysChem*, **2007**, 0000.

112. (a) Johansson, L. B-A.; Davidsson, A. Analysis and application of linear dichroism on membranes. *J. Chem. Soc., Faraday Trans. 1*, **1985**, *81*, 1375-1388. (b) Wang H. Reflection/transmission measurements of anisotropic films with one of the principle axes in the direction of columnar growth. *J. Modern Opt.* **1995**, *42*, 497-505. (c) Collings, P. J.; Ratna, B. R.; Shashidhar, R. Order parameter measurements of dichroic dyes dissolved in smectic liquid crystals that tilt without layer contraction. *Phys. Rev. E*, **2003**, *67*, 021705 (1-8). (d) Rosell, F. I.; Boxer, S. G. Polarized absorption spectra of green fluorescent protein single crystals: transition dipole moment directions. *Biochemistry*, **2003**, *42*, 177-183. (e) Scaife, B. K. P.; Vij, J. K. Propagation of an electromagnetic wave in an absorbing anisotropic medium and infrared transmission spectroscopy of liquid crystals. *J. Chem. Phys.* **2005**, *122*, 174901 (1-11). (f) Chaney, S. B.; Zang, Z.-Y.; Zhao, Y.-P. Anomalous polarized absorbance spectra of aligned Ag nanorod arrays. *Appl. Phys. Lett.*, **2006**, *89*, 053117-1-3.
113. (a) Peterson D. L.; Simpson, W. T. Polarized electronic absorption spectrum of amides with assignments of transitions. *J. Am. Chem. Soc.* **1957**, *79*, 2375-2382. (b) Gabler, R.; Bearden, J.; Bendet, I. Anisotropic absorption of linearly polarized light by cylindrical molecules. *Biophysical Journal*, **1971**, *11*, 302-307. (c) Ebihara Y.; Vacha, M. A method for determining the absorption ellipsoid of single conjugated polymer molecules and single luminescent nanoparticles. *J. Chem. Phys.* **2005**, *123*, 244710 (1-4).
114. Haussühl, S. Physical Properties of Crystals, Wiley-VCH, Weinheim, **2007**; p 326.
115. Hasegawa, T.; Umemura, J.; Takenaka, T. Simple refraction law for uniaxial anisotropic media, *Appl. Spectrosc.* **1993**, *47*, 338-340.
116. Heavens, O. S. Optical Properties of Thin Solid Films. Butterworth Scientific, London, England, **1955**.
117. Nordén, B.; Lindblom, G.; Jonás, I. Linear dichroism spectroscopy as a tool for studying molecular orientation in model membrane systems, *J. Phys. Chem.* **1977**, *81*, 2086-2093.

118. Lopes, S.; Fernandes, M. X.; Prieto, M.; Castanho, M. A. R. B. Orientational order of the polyene fatty acid membrane probe *trans*-parinaric acid in Langmuir-Blodgett multilayer films. *J. Phys. Chem. B* **2001**, *105*, 562-568.
119. Johansson, L. B.-Å. Linear dichroism as a tool for studying the molecular orientation in membrane systems. 2. Order parameters of guest molecules from linear dichroism and nuclear magnetic resonance, *J. Phys. Chem.* **1978**, *82*, 2604-2609.
120. Kim, T.-D.; Kang, J.-W.; Luo, J.; Jang, S.-H.; Ka, J.-W.; Tucker, N. M.; Benedict, J. B.; Dalton, L. R.; Gray, T.; Overney, R. M.; Park, D. H.; Herman, W. N.; Jen, A. K.-Y. Ultralarge and thermally stable electro-optic activities from supramolecular self-assembled molecular glasses. *J. Am. Chem. Soc.* **2007**, *129*, 488-489.
121. Teng, C.; Man, H. Simple reflection technique for measuring the electro-optic coefficient of poled polymers. *Appl. Phys Lett.* **1990**, *56*, 1734-1736.
122. Page, R. H.; Jurich, M. C.; Reck, B.; Sen, A.; Twieg, R. J.; Swalen, J. D.; Bjorklund, G. C.; Willson, C. G. Electrochromic and optical waveguide studies of corona-poled electro-optic polymer films. *J. Opt. Soc. Am. B*, **1990**, *7*, 1239-1250.
123. (a) Graf, H. M.; Zobel, O.; East, A. J.; Haarer, D. The polarized absorption spectroscopy as a novel method for determining the orientational order of poled nonlinear optical polymer films. *J. Appl. Phys.* **1994**, *75*, 3335-3339. (b) Rodriguez, V.; Adamietz, F.; Sanguinet, L.; Buffeteau, T.; Sourisseau, C. Quantitative determination of the polar order induced under high electric field in amorphous PDRIM azobenzene polymer films. *J. Phys. Chem. B* **2003**, *107*, 9736-9743.
124. (a) Ye, C.; Marks, T. J. Synthesis of molecular arrays with nonlinear optical properties: second-harmonic generation by covalently functionalized glassy polymers. *Macromolecules*, **1987**, *20*, 2322-2326. (b) Hampsch, H. L.; Yang, J.; Wong, G. K.; Torkelson, J. M.

- Orientation and second-harmonic generation in doped polystyrene and poly(methyl methacrylate) films. *Macromolecules*, **1988**, *21*, 526-528. (c) Singer, K. D.; King, L. A. Relaxation phenomena in polymer nonlinear optical materials. *J. Appl. Phys.* **1991**, *70*, 3251-3255. (d) Dureiko, R. D.; Schuele, D. E.; Singer, K. D. Modeling relaxation processes in poled electro-optic polymer films. *J. Opt. Soc. Am. B*, **1998**, *15*, 338-350. (e) Wong, K. Y.; Shen, Q. Effects of physical aging on the relaxation of poled nonlinear optical polymers. *J. Appl. Phys.* **1999**, *86*, 2953-2958.
125. To, C. W.; Wong, K. Y. Comparative studies of molecular reorientations in thermal-assisted electric-field poled nonlinear optical polymers. *J. Appl. Phys.* **2006**, *100*, 0735051-0735056.
  126. Welch, K.; Mousavi, S.; Lundberg, B.; Stromme, M. Viscoelastic characterization of compacted pharmaceutical excipient materials by analysis of frequency- dependent mechanical relaxation processes. *Eur. Phys. J. E*, **2005**, *18*, 105-112.
  127. (a) Kim, H. S.; Jeffrey, G. A.; Rosenstein, R. D. The crystal structure of glucitol-pyridine. *Acta Cryst.* **1971**, *B27*, 307-314. (b) Quinquenet, S.; Ollivon, M.; Grabielle-Madelmont, C. Polymorphism of hydrated sorbitol. *Thermochem. Acta*, **1988**, *125*, 125-140. (c) Schouten, A.; Kanters, J. A.; Kroon, J.; Comini, S.; Looten, P.; Mathlouthi, M. Conformational polymorphism of D-sorbitol (D-glucitol): the crystal and molecular structures of D-glucitol 2/3-hydrate and *epsilon* D-glucitol. *Carbohydr. Res.*, **1998**, *312*, 131-137.
  128. (a) Yu, L. Growth rings in D-sorbitol spherulites: connection to concomitant polymorphs and growth kinetics. *Cryst. Growth Des.* **2003**, *3*, 967-971. (b) Yu, L. Nucleation of one polymorph by another. *J. Am. Chem. Soc.* **2003**, *125*, 6380-6381.
  129. Collings, P. J.; Ratna, B. R.; Shashidhar, R. *Phys. Rev. E*, **2003**, *67*, 02175-1-8.
  130. Kahr, B.; Claborn, K. *ChemPhysChem*, **0000**, *00*, X-XX. DOI: 10.1002/cphc.200700173.

131. Libowitzky, E.; Rossman, G. R. Principles of quantitative absorbance measurements in anisotropic crystals, *Phys. Chem. Minerals*, **1996**, *23*, 319-327.
132. Scaife, B. K. P.; Vij, J. K. J. *Chem. Phys.* **2005**, *122*, 174901-1-11.
133. Marder, S. R.; Perry, J. W.; Yakymyshyn, C. P. Organic salts with large second-order optical nonlinearities. *Chem. Mater.* **1994**, *6*, 1137-1147.
134. (a) Pan, F.; Knopfle, G.; Bosshard, Ch.; Follonier, S.; Spreiter, S.; Wong, M. S.; Gunter, P. Electro-optic properties of the organic salt 4-N,N-dimethylamino-4'-N'-methyl-stilbazolium tosylate. *Appl. Phys. Lett.* **1996**, *69*, 13-15. (b) Bhowmik, A. K.; Xu, J.; Thakur, M. Polarized optical absorption and photoluminescence measurements in single-crystal thin films of 4'-dimethylamino-N-methyl-4-stilbazolium tosylate. *Appl. Phys. Lett.* **1999**, *75*, 3291-3293. (c) Sohma, S.; Takahashi, H.; Taniuchi, T.; Ito, H. Organic nonlinear optical crystal DAST and its device applications. *Chemical Physics*, **1999**, *245*, 359-364. (d) Follonier, S.; Fierz, M.; Biaggio, I.; Meier, U.; Bosshard, Ch.; Gunter, P. Structural, optical, and electrical properties of the organic molecular crystal 4-N,N-dimethylamino-4'-N'-methyl stilbazolium tosylate. *J. Opt. Soc. Am. B*, **2002**, *19*, 1990-1998. (e) Geis, W.; Sinta, R.; Mowers, W.; Deneault, S. J.; Marchant, M. F.; Krohn, K. E.; Spector, S. J.; Calawa, D. R.; Lyszczarz, T. M. Fabrication of crystalline organic waveguides with an exceptionally large electro-optic coefficient. *Appl. Phys. Lett.* **2004**, *84*, 3729-3731.
135. Loew, L. M.; Simpson, L.; Hassner, A.; Alexanian, V. An unexpected blue shift caused by differential solvation of a chromophore oriented in a lipid bilayer. *J. Am. Chem. Soc.* **1979**, *101*, 5439-5440.
136. At high dye loading densities ( $\geq 1.0$  wt. %), DAST crystallizes from the melt prior to spherulite formation. Visible spectra of these samples are identical to those of crushed pure DAST crystals, possessing the characteristic peak at 550 nm.

137. Kaminsky, W.; Claborn, K.; Kahr, B. Polarimetric imaging of crystals. *Chem. Soc. Rev.* **2004**, 33, 514-525.
138. Kaminsky, W.; Jin, L.-W.; Powell, S.; Maezawa, I.; Claborn, K.; Branham, C.; Kahr, B. Polarimetric imaging of amyloid. *Micron*, **2006**, 37, 324-338.

## Curriculum Vitae

Jason B. Benedict

### Education

Degree Sought:

**Ph.D.** University of Washington. Seattle, WA. GPA: 3.78  
Chemistry, 2001-2007

Degree Held:

**B.S.** Arizona State University. Tempe, AZ. GPA: 3.34  
Chemistry, 1996-2001; Philosophy minor

### Awards/Honors

- |           |  |
|-----------|--|
| 2005      | George A. Jeffrey Award from the Pittsburgh Diffraction Society for scientific excellence of graduate student research.  |
| 2005      | Travel Grant to the XX IUCr Annual Congress in Italy from the U.S. National Committee for Crystallography  |
| 2005      | Ludo Frevel Crystallography Scholarship from the International Centre for Diffraction Data to support promising graduate students in crystallography-related fields. |
| 2004      | Outstanding Service Employee Award from the Department of Chemistry of the University of Washington  |
| 2004      | American Crystallographic Association Travel Grant for the 2004 Annual Meeting in Chicago, Il  |
| 2001-2002 | Cady Fellowship from the Department of Chemistry of the University of Washington   |
| 2001      | Hypercube award for academic excellence from Department of Chemistry of Arizona State University   |
| 1997-2001 | Dean's List at Arizona State University  |



### Research Experience

- 2001-present    Research assistant in the lab of Bart Kahr at the University of Washington. Studies include optical probes of various properties of growing crystal surfaces, crystal growth mechanisms, materials science applications of dye inclusion crystals, and the optical characterization of electro-optic poled polymers.
- 2002-2006      Departmental crystallographer. Determination of over 100 structures, many involving difficult crystallizations, unstable crystals/compounds, disorder and twinning.
- 2000-2001      Undergraduate researcher in the lab of M. Tyler Caudle at Arizona State University. Studies involved the exploration of metal ion scrambling in hexanuclear carbamate clusters predominately through the use of single crystal X-ray diffraction, optical spectroscopies, and  $^{13}\text{C}$  nuclear magnetic resonance.

### Publications Related to Thesis

11. Dyeing Polymorphs: The MALDI Host 2,5-Dihydroxybenzoic Acid. D. E. Cohen, J. B. Benedict, B. Morlan, D. T. Chiu, B. Kahr, *Cryst. Growth Des.* 7(3), 492-495 (2007).
10. Mesoscale Chiroptics of Rhythmic Precipitates. E. Gunn, R. Sours, J. B. Benedict, W. Kaminsky, B. Kahr, *J. Am. Chem. Soc.* 128(44), 14234-14235 (2006).
9. What is Syncrystallization? States of pH Indicator Methyl Red in Crystals of Phthalic Acid. J. B. Benedict, D. E. Cohen, S. Lovell, A. L. Rohl, B. Kahr, *J. Am. Chem. Soc.* 128(16), 5548-5559 (2006)
8. Time-resolved EPR spectra of the triplet excited states of diaminoacridine guests in polar potassium hydrogen phthalate single crystals. M. Bellinazzi, A. Barbon, B. Kahr, J. B. Benedict, M. Brustolon, *Phys. Chem. Chem. Phys.* 8, 379-385 (2006)
7. Photochromism of a spirooxazine in the single crystalline phase. D. G. Patel, J. B. Benedict, R. A. Kopelman, N. L. Frank, *Chem Comm.* 17, 2208-2210 (2005)

6. Luminescent Probes of Crystal Growth: Surface Charge and Polar Axis Sense in Dye-Doped Potassium Hydrogen Phthalate. A. Barbon, M. Bellinazzi, J. B. Benedict, M. Brustolon, S. D. Fleming, S.-H. Jang, B. Kahr, A. L. Rohl, *Angew. Chem. Int. Ed.* 43, 5328-5331 (2004)
5. Potassium hydrogen diphthalate dihydrate: a new structure and correction to the literature. J. B. Benedict, T. Bullard, W. Kaminsky, B. Kahr, *Acta Cryst.* C60, m551-m553 (2004)
4. Optical consequences of chemistry at growing crystal interfaces. B. Kahr, M. Kurimoto, W. Kaminsky, S.-H. Jang, J. B. Benedict, *From Fluid-Solid Interfaces to Nanostructural Engineering*, (J. De Yoreo et al. eds.) Plenum/Klumer (2004)
3. 3,3'-Didecyl-5,5'-bis(4-phenylquinolin-2-yl)-2,2'-bithienyl. J. B. Benedict, W. Kaminsky, C. J. Tonzola, *Acta Cryst. E.* E60(4), o530-o531 (2004)
2. Up-conversion Luminescence in Dye-Doped Crystals of Potassium Hydrogen Phthalate. J. B. Benedict, P. M. Wallace, P. J. Reid, S.-H. Jang, B. Kahr, *Adv. Mater.* 15(13), 1068-1070 (2003)
1. Metal Ion Scrambling in Hexanuclear  $M_6(Et_2NCO_2)_{12}$  Complexes ( $M = Co, Mg$ ). Synthesis, Solid State Structure, and Solution Dynamics of Heteronuclear  $Co_nMg_{(6-n)}(Et_2NCO_2)_{12}$  Complexes. M. T. Caudle, J. B. Benedict, C. K. Mobley, N. A. Straessler, T. L. Groy, *Inorg. Chem.* 41(12), 3183-3190 (2002)

### Publications Through Structure Collaborations

9. Ultralarge and Thermally Stable Electro-Optic Activities from Supramolecular Self-Assembled Molecular Glasses. T.-D. Kim, J.-W. Kang, J. Luo, S.-H. Jang, J.-W. Ka, N. Tucker, J. B. Benedict, L. R. Dalton, T. Gray, R. M. Overney, D. H. Park, W. N. Herman, A. K.-Y. Jen. *J. Am. Chem. Soc.* 129(3), 488-489 (2007).
8. A Functional Model for the Cysteinate-Ligated Non-Heme Iron Enzyme Superoxide Reductase (SOR). T. Kitagawa, A. Dey, P. Lugo-Mas, J. B. Benedict, W. Kaminsky, E. Solomon, J. A. Kovacs. *J. Am. Chem. Soc.* 128(45), 14448-14449 (2006).

7. How does Single Oxygen Atom Addition Affect the Properties of an Fe-Nitrile Hydratase Analogue? The Compensatory Role of the Unmodified Thiolate. P. Lugo-Mas, A. Dey, L. Xu, S. D. Davin, J. Benedict, W. Kaminsky, K. O. Hodgson, B. Hedman, E. I. Solomon, J. A. Kovacs. *J. Am. Chem. Soc.* 128(34) 11211-11221 (2006).
6. Pyrroline Chromophores for Electro-Optics. S.-H. Jang, J. Luo, N. M. Tucker, A. Leclercq, E. Zojer, M. A. Haller, T.-D. Kim, J.-W. Kang, K. Firestone, D. Bale, D. Lao, J. B. Benedict, D. Cohen, W. Kaminsky, B. Kahr, J.-L. Bredas, P. Reid, L. R. Dalton, A. K.-Y. Jen. *Chem. Mater.* 18(13), 2982-2988 (2006).
5. Crystal structures and luminescence properties of osmium complexes of cis-1,2-viylenebis(diphenylarsine) and pyridyl ligands: Possible evidence for metal d, ligand backbonding. B. Carlson, G. D. Phelan, J. B. Benedict, W. Kaminsky, L. Dalton, *Inorganica Chimica Acta*, 359(4), 1093-1102 (2006)
4. Systematic study of the structure-property relationship of a series of ferrocenyl nonlinear optical chromophores. Y. Liao, B. E. Eichinger, K. A. Firestone, M. Haller, J. Luo, W. Kaminsky, J. B. Benedict, P. J. Reid, A. K.-Y. Jen, L. R. Dalton, B. H. Robinson, *J. Am. Chem. Soc.* 127(8), 2758-2766 (2005)
3. Crystallography and luminescence of divalent osmium complexes green osmium emitters and possible evidence for d-orbital backbonding. B. Carlson, G. D. Phelan, J. Benedict, W. Kaminsky, L. Dalton, *Inorganica Chimica Acta* 357, 3967-3974 (2004)
2. Nucleophilic Aromatic Substitution on Aryl-Amido Ligands Promoted by Oxidizing Osmium(IV) Centers. J.D. Soper, E. Saganic, D. Weinberg, D. A. Hrovat, J. B. Benedict, W. Kaminsky, J. Mayer, *Inorganic Chemistry* 43(19), 5804-5815 (2004)
1. How does cyanide inhibit superoxide reductase? Insight from synthetic FeIIIN<sub>4</sub>S model complexes. J. Shearer, S. B. Fitch, W. Kaminsky, J. Benedict, R. C. Scarrow, J. A. Kovacs, *Proc. Natl. Acad. Sci. USA*, 100(7), 3671-3676 (2003)

### Abstracts

3. Spherulites for polar dye organization. J. B. Benedict, C. Branham, M. Nichols, S. Randall, P. Reid, B. Kahr, Lecture Abstract of the XX IUCr Congress, Florence, Italy, August 23-31, (2005).
2. Optical Probes of Growing Crystals: Elucidating Surface Chemistry and "Sensing" Polar Axes. J. B. Benedict, A. Barbon, M. Bellinazzi, M. Brustolon, S. D. Fleming, S.-H. Jang, S. Lovell, B. Kahr, A. L. Rohl, Invited Lecture Abstract, American Crystallographic Association Annual Meeting, Chicago, IL, United States, July 17-22, (2004)
1. Interactions in hexanuclear magnesium(II) and cobalt(II) carbamate complexes. Jason B. Benedict, M. Tyler Caudle, Abstracts of Papers - American Chemical Society (2001), 221st CHED-364.

### Patents

1. Osmium-based oxygen sensor and pressure-sensitive paint. W. B. Carlson, G. D. Phelan, J. B. Benedict, W. Kaminsky, G.-E. Khalil, M. P. Gouterman, L. R. Dalton. *U.S. Pat. Appl. Publ.* 46pp. (2007).